MASSIVE STAR FORMATION IN SPARSE ENVIRONMENTS

by

Joel B. Lamb

A dissertation submitted in partial fulfillment
of the requirements for the degree of
Doctor of Philosophy
(Astronomy)
in The University of Michigan
2012

Doctoral Committee:

Associate Professor Sally Oey, Chair
Professor Fred Adams
Professor Mario Mateo
Associate Professor Oleg Gnedin
Associate Professor Rupali Chandar, University of Toledo

For my parents, who have provided unconditional encouragement and support.

ACKNOWLEDGMENTS

Sally Oey has been a fantastic advisor from day one at Michigan. She has my deepest gratitude for all the time, effort, and energy she expended on my behalf as an advisor and mentor. I appreciate immensely her support throughout my graduate school experience. She was always quick to praise my successes and patiently helped with my shortcomings. Her influence has been paramount in every aspect of my growth as a student, scientist, teacher, writer, and mentor. I appreciate the sense of community she fostered within her research group by having frequent FANG group meetings and inviting us for delicious meals at her home. This thesis began as a first year project outlined by Sally, and I have found it tremendously fulfilling to expand its scope and scale with her thoughtful mentorship.

My dissertation committee has been instrumental to the success of this research. Their advice and direction have greatly enhanced the science within this thesis and contributed significantly to my growth as a scientist. Fred Adams has identified and discussed useful algorithms and analyses that became key pieces of this work. Oleg Gnedin helped me design and understand the results of Monte Carlo simulations presented within. Mario Mateo provided excellent advice on the interpretation of our observational data, and possible observing setups to maximize our science. His efforts at time allocation for my Magellan observations were also tremendously appreciated. Rupali Chandar gave valuable advice and an important fresh perspective on my research during this last year.

This thesis was not an individual effort, and I received help from numerous individuals throughout this project. Sally has been instrumental as an advisor every step of the way, from the science to the writing. Undergraduate students Andrew Graus and Dominique Segura-Cox contributed substantially to the data reduction for this

thesis. Andrew helped determine the spectral types for stars in the RIOTS4 survey. Jess Werk contributed valuable knowledge and expertise on sparse star formation and the IGIMF. Laura Ingleby generously observed a few objects for us with the MIKE spectrograph at Magellan. Tony Zenn wrote a friends-of-friends code utilized in this thesis. Radek Poleski investigated a few issues we encountered with the OGLE survey. Jason Harris and Dennis Zaritsky granted us access to the MCPS V-band data. Phil Massey and Nidia Morrell provided advice on dealing with massive star spectra. I thank Fred Adams, Rupali Chandar, Cathie Clarke, Oleg Gnedin, Simon Goodwin, Lee Hartmann, Wen-hsin (Tina) Hsu, Anne Jaskot, Mario Mateo, Joel Parker, Eric Pellegrini, and Jordan Zastrow for helpful discussions, advice, and suggestions. I also thank the support staff at Magellan and Las Campanas Observatory for their help during the nearly six weeks I spent observing in Chile during my graduate career.

The FANG working group has been an indispensable resource and contributed to my growth as a scientist, a scholar, and a person. Past and present members of FANG, including Thomas Bensby, Andrew Graus, Dan Hanish, Anne Jaskot, Carol Kehrig, Cole Kushner, Brian Mikolajczyk, Eric Pellegrini, Dominique Segura-Cox, Colin Slater, and Jordan Zastrow have been role models, peer advisors, and also good friends. In particular, FANG has provided valuable experiences and opportunities to hone my presentation skills and participate in a variety of enriching activities, including peer review, mock TAC committees, and regular discussion of the latest news in science and astronomy. In addition, the FANG writing group and in particular, Anne and Jordan, have greatly enhanced my abilities with the written word.

Teaching is one of my great passions, so I'd like to thank all those who have contributed to my growth as a teacher including Scott Cameron, Kiwi Davis, Lee Hartmann, Jon Miller, Jon Monnier, Shannon Murphy, Sally Oey, and Shannon Schmoll. I'd especially like to thank Sally for entrusting me with the debut of a quantitative thinking component in discussion sections during my first semester teaching. It was a valuable first experience to participate in the creation of teaching plans and mini-lessons. It also facilitated the discovery of my strengths and weaknesses in the classroom, as well as a venue to test the effectiveness of different teaching meth-

ods. Shannon Schmoll was instrumental in helping me during my first experience as the sole instructor of a class. Her syllabus, lecture slides, and knowledge of the planetarium were all valuable resources.

The support staff in the department of astronomy have been a large help during my time at Michigan. Shannon Murphy has always been a key resource for teaching and outreach. Her behind-the-scenes efforts keeping the planetarium and telescopes in working order is very appreciated. Roy Bonser and Jeremy Hallum have resolved numerous computer issues and implemented a variety of software packages critical to the success of this project. Brian Cox, Stephanie Ford, Sarah Lloyd, Carin Scott, Ann Smith, and Li Yong handled any and all issues I could come up with outside the realms of science and were key resources for the smooth operation of the department. Nuria Calvet and Jon Miller provided valuable advice and advocacy during their terms as graduate student advisors.

My fellow graduate students have supported me every step of the way. I'm particularly thankful to Kiwi Davis, Jeffrey Fogel, and Sasha Muratov for putting up with my random questions and exclamations in our shared office space. I've made some great friends including Jen Blum, Nate Crockett, Kiwi Davis, Jeffrey Fogel, Matt Greco, Sasha Muratov, and Jess Werk. A special thanks to Jen Blum and Kiwi Davis who helped me feel at home in Michigan my first year here. I'm also thankful for the continued friendship of Maggie Bacon and Laura Ingleby who moved here from the University of Iowa at the same time as me. My deepest gratitude to Tina Hsu for helping me through many trying times including prelims, paper writing, code debugging and algorithms, and putting together my thesis. Your support, both intellectual and emotional, has made this thesis possible.

Finally, a special thanks to my parents, Damon and Susan Lamb, for their steadfast support of me throughout my academic endeavors. Without them, I would have never made it to Michigan in the first place, let alone completed my PhD. My parents, along with my brother, Justin, and fiancee, Tina, have always been there for me in times of need and to share in my joys and successes. I thank each of you from the bottom of my heart.

Chapter 2 of this thesis is based on a publication in *The Astrophysical Journal* (Lamb et al. 2010) and is reproduced here with permission. It was supported by program HST-GO-10629.01, provided by NASA through a grant from the Space Telescope Science Institute, which is operated by the Association of Universities for Research in Astronomy, Inc., under NASA contract NAS5-26555. We also recognize support from NSF grant AST-0907758. Chapter 3 is based on work to be published in *The Astrophysical Journal* (Lamb et al. in preparation). This work was supported by funding from NSF grant AST-0907758. Finally, I'm also grateful for numerous instances of travel support provided by the University of Michigan Rackham Graduate School.

CONTENTS

LIST OF FIGURES

Figure

LIST OF TABLES

Table

ABSTRACT

Sparse massive star formation provides a critical test for star formation theories. To investigate the extreme case, we probe the immediate stellar environment around eight seemingly isolated massive stars in the Small Magellanic Cloud using the *Hubble Space Telescope's* Advanced Camera for Surveys. Our observations reveal sparse clusters of $8-10$ stars from $1M_{\odot}$ to $4M_{\odot}$ around three of our targets, while three other stars remain candidates for in situ field massive star formation. Stochastic sampling effects dominate in these sparse clusters, so we compare our observations to a simulated cluster population generated from a –2 power-law distribution in star count (N_{*}) or cluster mass ($M_{\rm cl}$) and populated randomly following a Kroupa IMF. Our results suggest that clusters are built stochastically by randomly sampling stars from a universal IMF with a fixed stellar upper-mass limit and are inconsistent with a $m_{\rm max}-M_{\rm cl}$ relation.

To investigate field massive stars as a population, we carry out a comprehensive survey, the Runaways and Isolated O Type Star Spectroscopic Survey of the SMC (RIOTS4). RIOTS4 is a spatially complete census of the entire field massive star population of the SMC undertaken with the IMACS multi-object spectrograph and MIKE echelle spectrograph on the Magellan telescopes. We find the slope of the field IMF above $20M_{\odot}$ is $\Gamma_{\rm IMF}$=2.3±0.4, which is much steeper than the canonical Salpeter slope of $\Gamma_{\rm IMF}$=1.35. We extend our IMF measurement to lower masses using BV photometry from the OGLE survey. We develop a statistical approach to generate a mass probability distribution for each star to measure the IMF with OGLE photometry, from which we again find $\Gamma_{\rm IMF}$=2.3±0.4 above $7M_{\odot}$. We rule out the possibility that a unique star formation history or high binary fraction could make a Salpeter IMF consistent with the steep observed present day mass function

of the field. Interestingly, the steep field IMF does not support our earlier results, indicating that high mass stars are depleted in the field population. We may reconcile these findings if sparse O star clusters are remnants of larger clusters that rapidly dissolve or if the mechanism for sparse massive star formation is different from that in clusters.

CHAPTER 1

Introduction

1.1 Introduction

Star formation is the final stage of perhaps the most basic physical process in the universe: gravitational attraction and collapse. In the early universe, gravity led to the hierarchical formation of galaxies through the build-up and merger of dark matter halos and primordial gas (White & Rees 1978; Searle & Zinn 1978). Within galaxies, dense clouds of molecular gas undergo collapse due to self-gravity. As they collapse, these clouds fragment hierarchically into clumps and further from clumps into stars (Hoyle 1953; Oey 2011). However, within this simplistic framework there exists a great deal of physical complexity. The specifics of the fragmentation process, including the effects of rotation, turbulence, cloud geometry, and magnetic fields are still widely studied and debated. Thus, despite being such a fundamental astrophysical process, we are far from a complete understanding of star formation.

Direct studies of star formation are limited to a handful of nearby regions with ongoing star formation. The overwhelming majority of stars in the local universe formed long ago. Thus, to study star formation beyond these few systems, we are left with studying the resultant stellar population that formed. Specifically, the one observable of a stellar population that is a direct consequence of the star formation process is the stellar initial mass function (IMF). The form of the stellar IMF was first examined by Salpeter (1955) who examined the luminosity distribution of main sequence stars in the solar neighborhood. He found that the stellar IMF could be

simply approximated using a power law function of the form

$$n(m)\ dm \propto m^{-\gamma} dm\ , \tag{1.1}$$

where n is the number of stars, m is stellar mass, and the power law slope, $\gamma = 2.35$. For stars $\gtrsim 1 M_{\odot}$, this power law form is robustly verified for a range of stellar populations including the local Galactic field, OB associations and young, massive clusters (Kroupa 2001 and references within). Thus, the Salpeter IMF is widely accepted as the canonical model for high mass stars.

It is clear from the Salpeter IMF that low mass stars are far more common than high mass stars. However, the stellar mass-luminosity relationship is even steeper than the Salpeter IMF, with $L \sim m^3$ (Eddington 1924). Thus, despite their small numbers, massive stars dominate the light output of stellar populations. Furthermore, due to their short lifespan, massive stars serve as primary indicators of recent star formation. Beyond star formation, feedback from massive stars is one of the primary drivers of cluster and galactic evolution. Therefore, the formation of massive stars is exceptionally important to understand due to their stochasticity and the disproportionate influence they have on their local environment and key observables.

Massive stars pose difficulties for star formation models. Under most astrophysical conditions, molecular clouds are expected to fragment into pieces of $\sim 1 M_{\odot}$ (Jeans mass; Jeans 1902). Thus, one of two things must happen for massive star formation to occur. Either the local gas conditions of the cloud must significantly increase the Jeans mass, or gas outside of the molecular cloud fragment must be accreted by the forming star. These scenarios account for the two primary paradigms for massive star formation, monolithic collapse (e.g., Shu et al. 1987) and competitive accretion (e.g., Zinnecker 1982), respectively. While either model is plausible in a clustered environment, this is not the case for a distributed population. There are scenarios in which a small molecular cloud could collapse monolithically in near isolation (e.g., Krumholz et al. 2009). However, competitive accretion stipulates that a high mass star may only form along with a requisite population of low mass stars, such that

the most massive star formed, $m_{\rm max}$, is related to the the total cluster mass, $M_{\rm cl}$, by $m_{\rm max} \propto M_{\rm cl}^{2/3}$ (Bonnell et al. 2004). Therefore, the formation of massive stars in sparse environments provides a key diagnostic test between these star formation models.

The concept of a deterministic relationship between $m_{\rm max}$ and $M_{\rm cl}$ is not relegated solely to competitive accretion. Weidner & Kroupa (2004; 2006) develop a statistical model to relate $m_{\rm max}$ and $M_{\rm cl}$ and compare their model with an aggregation of $m_{\rm max}$ and $M_{\rm cl}$ estimates of Galactic clusters from the literature. They argue that the close agreement found between their model and the distribution of $m_{\rm max}$ vs. $M_{\rm cl}$ in the Galactic clusters is evidence of a deterministic $m_{\rm max} - M_{\rm cl}$ relationship. However, correlation does not imply causation, as Oey & Clarke (2005) demonstrate that for a universal Salpeter IMF the expectation value of $m_{\rm max}$ correlates with $M_{\rm cl}$, simply due to the increased likelihood of randomly sampling a higher mass star given more cluster mass to work with. Thus, using an expanded sample of Galactic clusters, Weidner et al. (2010) use a variety of statistical tests to demonstrate that the observed $m_{\rm max}-M_{\rm cl}$ relationship in this sample is inconsistent with a universal Salpeter IMF. However, Maschberger & Clarke (2008) supplement the Galactic cluster database of Weidner & Kroupa (2006) with a sample of isolated and sparsely clustered Herbig Ae/Be stars from Testi et al. (1997). The inclusion of this population significantly alters the $m_{\rm max}$ vs. $M_{\rm cl}$ cluster distribution by disrupting the previously tight fit with significant scatter. Maschberger & Clarke (2008) caution that sample selection can play a huge role in the observed $m_{\rm max}-M_{\rm cl}$ relationship. Selman & Melnick (2008) similarly argue that the Weidner & Kroupa (2006) Galactic cluster sample focuses on well-populated clusters and is therefore biased against small clusters that form an exceptionally high mass star given their cluster mass. Furthermore, they argue that such 'top heavy' clusters, dominated by a single massive star, are gravitationally unstable and will become unbound and indistinguishable as a cluster. Therefore, massive stars in sparse environments are a key diagnostic component for the $m_{\rm max} - M_{\rm cl}$ distribution of clusters.

The effects of a deterministic $m_{\rm max} - M_{\rm cl}$ relationship on the stellar population

of a galaxy are substantial. Primary among them is the steepening of the integrated galactic initial mass function (IGIMF). Just like the stellar IMF, clusters follow a similar power law mass distribution, given by

$$n(M_{\rm cl})\ dM_{\rm cl} \propto M_{\rm cl}^{-\beta}\ dM_{\rm cl} \quad , \tag{1.2}$$

where $n(M_{\rm cl})$ is the number of clusters in the mass range $M_{\rm cl}$ to $M_{\rm cl} + dM_{\rm cl}$. The combination of this cluster mass function and a deterministic $m_{\rm max} - M_{\rm cl}$ relationship prevent a large fraction of clusters from sampling the top end of the IMF, which thus steepens the overall IMF of a galaxy and decreases the expected number of O and B stars in a galaxy. Thus, the impact of a deterministic $m_{\rm max} - M_{\rm cl}$ relationship is far-reaching and it is vitally important to investigate the clustering properties of sparse massive stars. Furthermore, the population of field massive stars can provide a direct test of a steepened IGIMF, since it would be the most substantially impacted population if they originate from in situ formation. Thus, the mass function of field OB stars provides a key constraint on the possible magnitude and existence of a steepened IGIMF.

While the field may seem to be the result solely of sparse star formation, there is actually a well-known runaway star component of the field population. These objects form in the dense cores of star clusters and are ejected either dynamically (Poveda et al. 1967), due to the supernova of a binary companion star (Blaauw 1961), or both processes may occur one after the other in a two step ejection (Gvaramadze et al. 2012). Estimates of the runaway faction of field O stars vary up to an order of magnitude from as low as 10% (Blaauw 1961) to as high as 100% (Gvaramadze et al. 2012). One undisputed property of runaways is that the fraction of O star runaways is higher than B star runaways (e.g., Blaauw 1961; Stone 1991). Thus, if runaways are the primary component of the field population, it would likely result in a shallow field IMF.

Previous studies of field massive star populations yield conflicting results on the mass function of field stars. A steep field IMF is discovered in both the Magellanic

Clouds, with $\gamma \sim 4-5$, compared to the canonical Salpeter slope of $\gamma \sim 2.35$ (Massey et al. 1995; Massey 2002). A slightly steepened field IMF is found in NGC 4214 (Ubeda et al. 2007), while a Salpeter slope is found in the field population around 30 Dor in the Large Magellanic Cloud (Selman et al. 2011). These conflicting results illustrate the need for a large-scale survey of field massive stars.

In this thesis, we use a sample of field OB stars in the Small Magellanic Cloud (SMC) identified by Oey et al. (2004) to investigate the clustering properties of seemingly isolated massive stars and measure the IMF of the field massive star population. In Chapter 2, we present high resolution VI imaging observations of eight field massive stars using HST Advanced Camera for Surveys. We search for stellar clustering in the immediate vicinity of these stars using both a stellar density analysis and a friends-of-friends algorithm. Our search detects three sparse clusters and five isolated massive stars, two of which are runaway stars. Since stochastic effects dominate these sparse clusters, we perform Monte Carlo simulations to explore how our observations fit within the framework of empirical, galactic cluster properties. In Chapter 3, we present the results of our Runaways and Isolated O Type Star Spectroscopic Survey of the SMC. This survey covers a spatially complete sample of field massive stars in the SMC. RIOTS4 observations are performed with the IMACS multi-object spectrograph and the MIKE echelle spectrograph on the Magellan Baade and Clay telescopes respectively. Using accurate mass estimates from our RIOTS4 spectra, we measure the field IMF of the SMC for stars $> 20M_{\odot}$. We extend this IMF measure down to $7M_{\odot}$ with BV photometry from the Optical Gravitational Lensing Experiment (OGLE). In Chapter 4, we summarize the results of this thesis.

CHAPTER 2

The Sparsest Clusters With O Stars

2.1 Introduction

Most observational properties of galaxies and stellar populations are directly influenced by star formation. Massive stars, although small in number, disproportionally affect observables such as the integrated light from galaxies, feedback effects, star formation rates, and many others. However, there is significant debate regarding the conditions under which massive stars form. The competitive accretion model of star formation requires that a population of low-mass stars must form in the presence of a high-mass star (e.g. Bonnell et al. 2004), while the core accretion model of star formation allows for massive stars to form in relative isolation (e.g. Krumholz et al. 2009). Empirical studies are similarly divided on the connection between cluster mass and massive star formation. A physical relationship between the two (e.g. Weidner & Kroupa 2006, hereafter WK06) would indicate that massive stars *always* form in clusters, while random statistical sampling (e.g. Elmegreen 2000) would indicate that massive stars *preferentially* form in clusters. One observational method to differentiate between these theories is to examine the sparsest environments where massive stars are found. A targeted study of field massive stars can quantify limitations on the minimum stellar groupings needed for massive star formation. Such a study, which we present in this work, provides direct observational constraints for the two competing theories of star formation.

The core accretion model suggests that stars of all masses form by a fragmentation process in molecular clouds, where cores collapsing due to self-gravity represent the mass available to form an individual star or stellar multiple system (e.g. Shu

et al. 1987). In this model, massive stars must necessarily form from massive cores; however, it is unclear how such massive cores (up to hundreds of Jeans masses) can collapse without further fragmentation. Analytic models by Krumholz & McKee (2008) suggest that sufficiently dense clouds having surface densities ≥ 1 g/cm^{-2} will trap stellar and accretion radiation that heats clouds and prevents further fragmentation. Additionally, 3-D hydrodynamic simulations by Krumholz et al. (2009) reveal that self-shielding occurs along filaments resulting from gravitational and Rayleigh-Taylor instabilities, thereby channeling gas onto massive stars despite radiation pressures that dominate gravitational forces. These simulations result in the formation of a high-mass star or multiple system with a small companion population of low-mass stars. Similarly, Spaans & Silk (2000) show that the star formation properties of a gravitationally collapsing molecular cloud are highly dependent upon the equation of state of that cloud. For a cloud polytropic equation of state given by $P \propto \rho^{\gamma}$ where P is the thermal pressure and ρ is the gas density, they concluded that $\gamma > 1$ yields a peaked stellar initial mass function (IMF) rather than a power-law distribution. Li et al. (2003) conduct further simulations and find that molecular clouds with $\gamma > 1$ will most likely result in the formation of massive, isolated stars.

In contrast, the competitive accretion model suggests that fragmentation only produces low-mass stars, with high-mass stars formed by winning a competition for the remaining gas (e.g. Zinnecker 1982). In this scenario, the mass of a star is highly dependent upon the star-forming environment, with high-mass stars preferentially located at the bottom of the gravitational potential where the majority of a cluster gas reservoir gets funneled (Bonnell et al. 2001). This model of massive star formation requires that massive stars form in a clustered environment, with an explicit relation between the mass of a cluster ($M_{\rm cl}$) and the mass of the most massive star in the cluster ($m_{\rm max}$) given by $M_{\rm cl} \propto m_{\rm max}^{1.5}$ (Bonnell et al. 2004). Thus, competitive accretion forms massive stars along with a fully populated cluster of lower mass companion stars (Bonnell et al. 2007).

One of the primary differences between the observational predictions of these models is in the formation of high-mass stars in low $M_{\rm cl}$ environments. Compet-

itive accretion argues that formation of a high-mass star in a low-mass cluster is extremely difficult, while core accretion places no formal constraint on cluster mass. The competitive accretion model implies that the IMF is not a universal property of star formation, but instead tends to limit $m_{\rm max}$ for a given $M_{\rm cl}$. However, the IMF has been robustly verified for a wide range of star-forming environments, leading many to argue that $m_{\rm up}$, the upper stellar mass limit, is a universal property of star formation, regardless of environment (see Elmegreen 2000, 2006, 2008). In the case of a universal IMF, the relationship between $m_{\rm max}$ and $M_{\rm cl}$ is determined by the statistical mean (Oey & Clarke 2005). Not everyone agrees with the universality of the IMF; for example, WK06 argue for the existence of a deterministic $m_{\rm max}$-$M_{\rm cl}$ relation using analytic models. They further their argument by aggregating a data sample of Galactic clusters from which they find a strong correlation between $m_{\rm max}$ and $M_{\rm cl}$, closely following the derived $m_{\rm max}$-$M_{\rm cl}$ relation in Weidner & Kroupa (2004). Weidner et al. (2010a), who update and greatly expand the observational data set, conclude using a variety of statistical tests, that it is highly unlikely that the sample of Galactic clusters is generated from random sampling of a universal IMF.

However, Selman & Melnick (2008), using the same data from WK06, argue that the correlation of $m_{\rm max}$ with $M_{\rm cl}$ may be caused by the quick dispersal of clusters dominated by a single massive star due to gravitational instabilities. Since these objects would no longer be identifiable as clusters, such a dispersal effect would bias the WK06 cluster sample against clusters that formed with a flatter-than-Salpeter mass function, leaving behind only those clusters that follow a more standard Salpeter mass function. Maschberger & Clarke (2008) complement the WK06 data set with a sample of very small clusters from Testi et al. (1997) and find that the resultant ensemble of clusters does not significantly deviate from the expectations of a universal stellar IMF, when examining the correlation between the number of stars in a cluster (N_*) and $m_{\rm max}$. They argue that analyses using N_* instead of $M_{\rm cl}$ are more reliable since N_* is a directly observable quantity, while $M_{\rm cl}$ must be inferred. They caution that observational and sample selection effects can greatly influence the correlation of $m_{\rm max}$ with $M_{\rm cl}$ or N_* and that much more observational data is needed to reach a

conclusion.

A $m_{\rm max}$-$M_{\rm cl}$ relation, if it exists, has broad implications for cumulative stellar populations of galaxies. The power-law form of the cluster mass function is robust, similar to the IMF, with empirical derivations from a wide range of Galactic objects and environments, generally consistent with a power-law slope of –1.7 to –2.3 (§3.2). Coupling the cluster mass function, which is highly weighted towards low-mass clusters, with a deterministic $m_{\rm max}$-$M_{\rm cl}$ relation can have a large effect on the integrated galactic initial mass function (IGIMF) for stars. The primary consequences include a decrease in the expected number of OB stars within galaxies and an overall steepening of the IGIMF for the composite stellar population of a galaxy (Kroupa & Weidner 2003; Weidner & Kroupa 2005). A steepened IGIMF appears to successfully reproduce a variety of poorly-understood observationally-derived relations, including the dwarf galaxy mass-metallicity relation (Köppen et al. 2007), global correlations between Hα to UV flux ratios and galaxy mass (Hoversten & Glazebrook 2008; Lee et al. 2009; Meurer et al. 2009), and sharp radial surface brightness truncations in Hα compared to more extended-UV emission in the outer disks of nearby galaxies (Thilker et al. 2007; Pflamm-Altenburg et al. 2009). Such observational relations appear to arise naturally from clustered star formation and the $m_{\rm max}$-$M_{\rm cl}$ relation implicit to a steepened IGIMF. Maschberger et al. (2010) found evidence of a steepened IGIMF in the competitive accretion simulations of Bonnell et al. (2003, 2008), linking these two theories under their common assumption of a $m_{\rm max}$-$M_{\rm cl}$ relation. Considering the far-reaching implications of a steepened IGIMF, it is of utmost importance to examine its validity using observational constraints of isolated O stars.

One observational method to test the assertion of a $m_{\rm max}$-$M_{\rm cl}$ relation is to look for isolated, massive star formation. Field O stars are abundant in the literature (e.g., Massey et al. 1995) and may account for 25-30% of the O star population in a galaxy (Oey et al. 2004). While many of these stars are likely to be runaway stars from clusters, the remainder of field stars with no evidence of companions would be difficult to incorporate into the $m_{\rm max}$-$M_{\rm cl}$ relation proposed by WK06 and inherent to the theory of competitive accretion. In a study of Galactic field O stars, de Wit

et al. (2004, 2005) find that $4 \pm 2\%$ of all Galactic O stars appear to have formed in isolation, without the presence of a nearby cluster or evidence of a large space velocity indicative of a runaway star. This value is in agreement with the 5% of isolated O stars (defined as O stars without any companion O or B stars) found from Monte Carlo simulations of clusters (Parker & Goodwin 2007).

In this paper, we examine the stellar environment around field O stars to probe the limiting cases where O stars form in the sparsest stellar groups, or in near isolation.

2.2 Observations

2.2.1 *HST* Imaging Observations

We target field O stars in the SMC for this study because this nearby galaxy offers a view unobscured by gas and dust, allowing clear identification of the field massive stars and any low-mass companions. Our targets are taken from the work of Oey et al. (2004), who applied a friends-of-friends algorithm to photometrically identify OB star candidates, thereby identifying clusters and field stars in this sample. For this study, all of the targets were spectroscopically verified as O or early B stars, and all appeared isolated in ground-based imaging. In a pilot SNAP program, we exploit the $0.05''$/px spatial resolution of the Advanced Camera for Surveys (ACS) Wide-Field Camera aboard the *Hubble Space Telescope (HST)* to search for low-mass stars associated with the target OB stars. Unfortunately, Cycle 14 had an unusually low SNAP return, and we obtained observations of only eight targets. Table 2.1 lists our sample. Column 1 gives the star's ID from the catalog of Azzopardi & Vigneau (1975); the star smc-16 was catalogued by Massey et al. (1995). Columns 2, 3, and 4 list the right ascension, declination, and V magnitude, respectively, taken from Massey (2002). Column 5 gives the spectral types, in some cases derived from our observations described below in §2.2.3. Column 6 gives our mass estimate derived from the spectral type as described below, in §3.5. Column 7 gives our measured heliocentric radial velocities (see §2.3).

We obtained exposures of 6 seconds in the F555W band and 18 seconds in the

Field OB Star	RA[a]	Dec[a]	V[a]	Spectral Type[b]	Mass ($M_\odot$)	RV[b](km s^{-1})
smc16	01:00:43.94	-72:26:04.9	14.38	O9 V	23 ± 2	121 ± 21
AzV 58	00:49:57.84	-72:51:54.4	14.29	B0.5 III	22 ± 2	146 ± 11
AzV 67	00:50:11.13	-72:32:34.8	13.64	O8 V	37 ± 3	159 ± 13
AzV 106	00:51:43.36	-72:37:24.9	14.18	B1 II	18 ± 1	150 ± 12
AzV 186	00:57:26.99	-72:33:13.3	13.98	O8 III((f))[c]	33 ± 3	159 ± 10
AzV 223	00:59:13.41	-72:39:02.2	13.66	O9 II[d]	32 ± 2	189 ± 7[e]
AzV 226	00:59:20.69	-72:17:10.3	14.24	O7 III((f))[c]	35 ± 3	146 ± 21
AzV 302	01:02:19.01	-72:22:04.4	14.20	O8.5 V[e]	27 ± 2	161 ± 11[e]

a From Massey (2002).
b Observed with the IMACS multislit spectrograph on the 6.5m Magellan/Baade telescope, unless otherwise stated.
c From Massey (2009).
d From Evans (2006).
e Observed with the MIKE echelle spectrograph on the 6.5m Magellan/Clay telescope.

Table 2.1. List of SMC Field OB Stars.

F814W band. Figure 2.1 shows the F814W images of each object, with a circle of radius one parsec (3.4 arcsec) for reference, adopting an SMC distance of 60 kpc (Harries et al. 2003). The F555W exposures are complete down to 21st magnitude while the F814W are complete down to 22nd magnitude.

For each *HST* field, we use the IRAF DAOPHOT package to identify stars and obtain their photometry, using a combination of aperture photometry and PSF fitting. The aperture photometry is more reliable due to an undersampled PSF; however, PSF fitting was unavoidable in the case of close companions. The aperture photometry was done with an aperture radius of six pixels, while PSF fitting was done with a two-pixel FWHM and corrected to match the six-pixel aperture. For the F555W images, 3–5% of stars require PSF fitting, while in the F814W band, 10–15% require PSF fitting. PSF fitting did not reveal close companions for any of the target stars; however, the PSF subtraction of the target stars was very non-uniform, so companions cannot be entirely ruled out.

We used two separate methods to identify possible companion stars associated with the targets: (1) an analysis of the stellar density surrounding the OB star and (2) a friends-of-friends algorithm. For the first method, we computed the stellar surface density of the field as a function of radius from the target OB star. We performed this analysis using the F814W exposures, since they probe to a fainter magnitude than the F555W images. To measure the average stellar density of the

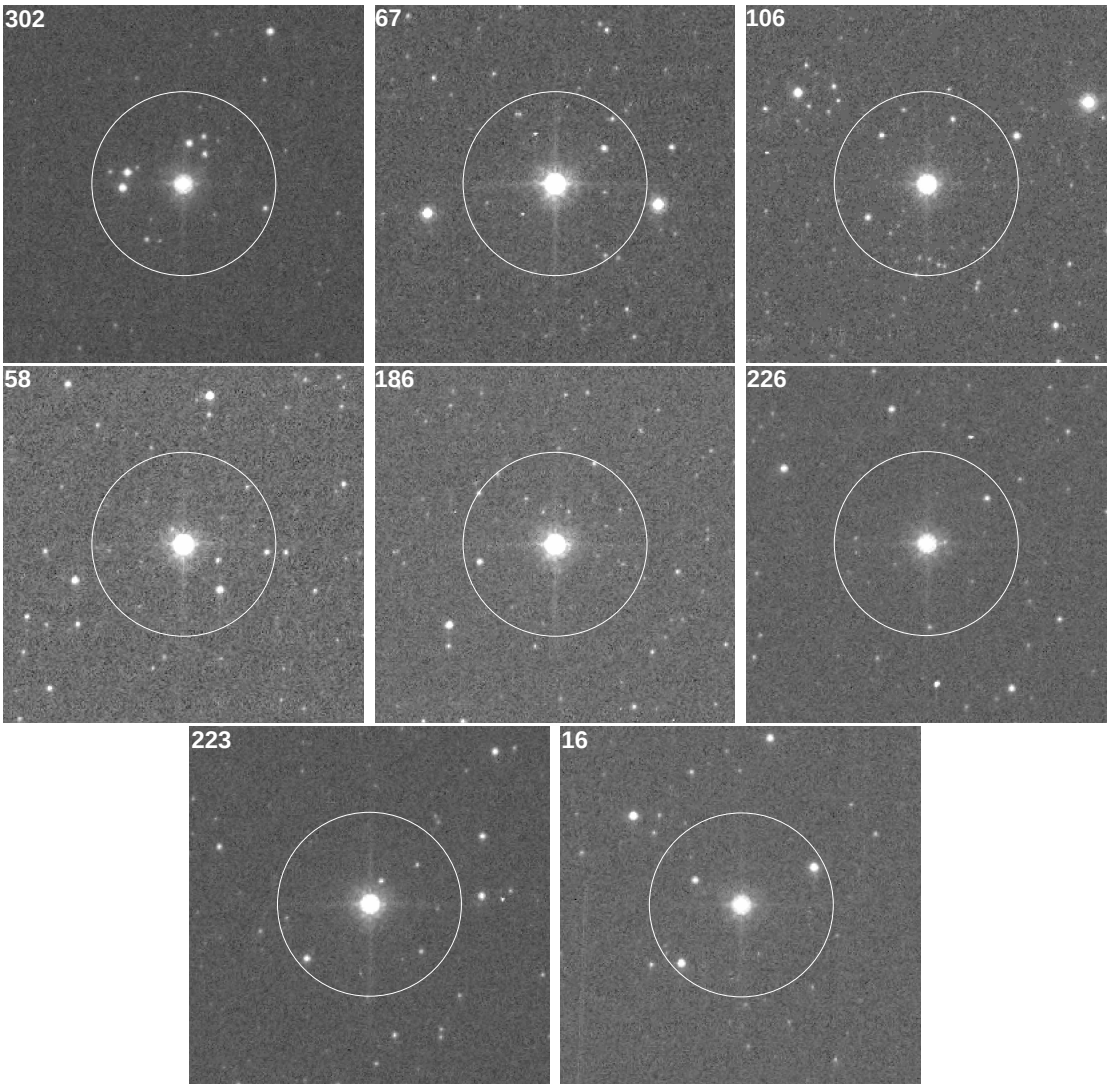

Figure 2.1. *HST* F814W images of each target star, with the star's ID number from the Azzopardi & Vigneau (1975) catalog listed in the upper left of each panel. The circle corresponds to a radius of 1 parsec. The top row contains fields showing a stellar density enhancement. The middle and bottom rows contains fields with no density enhancement. The bottom row contains stars found to be runaways.

field, we used an annulus centered on the OB star, with an inner radius ranging from 5″ to 10″, and an outer radius 10″ beyond the inner radius; the annuli were positioned to avoid any obvious stellar clustering. We define a density enhancement to occur when the observed stellar density is higher than the average stellar density of the field, including the statistical uncertainty. The probability that the observed stellar distribution matches the expected Poisson distribution, for a given background stellar density, is:

$$f(k, x) = x^k * e^{-x}/k! \tag{2.1}$$

where x is the expected star count within a given radius and k is the observed star count within that radius. A more useful value, which we designate the "field probability" $P(f)$, is the likelihood that the population follows the stellar density of the field:

$$P(f) = 1 - \sum_{0}^{k} f(k, x) \tag{2.2}$$

The right term in equation 2.2 yields the probability of observing more than k stars within a certain radius, and so $P(f)$ represents the probability of obtaining the background field. A smaller $P(f)$ therefore indicates an increased likelihood of clustering.

To examine the stellar environment near each target star, we plot the cumulative stellar density as a function of radius from the target OB star in Figure 2.2. The horizontal lines show the measured background density of each field. We were unable to detect stars within the wings of the target star, which typically extended to a radius of 0.2 pc. Thus, the actual cumulative stellar densities may be higher than those observed. Table 2.2 lists the angular and physical radius $R_{\rm cl}$ at which $P(f)$ is minimized in columns 2 and 3, respectively. The value of $P(f)$ is listed in column 4 for targets showing a density enhancement.

We also searched for density enhancements with a friends-of-friends algorithm applied to our F814W images. This method defines group members to be all the stars within a fixed clustering length l of another member of the same group. Following Battinelli (1991), we adopted a value for l that maximizes the number of groups having at least three stars. The distributions of clusters vs. l for each field are approximated

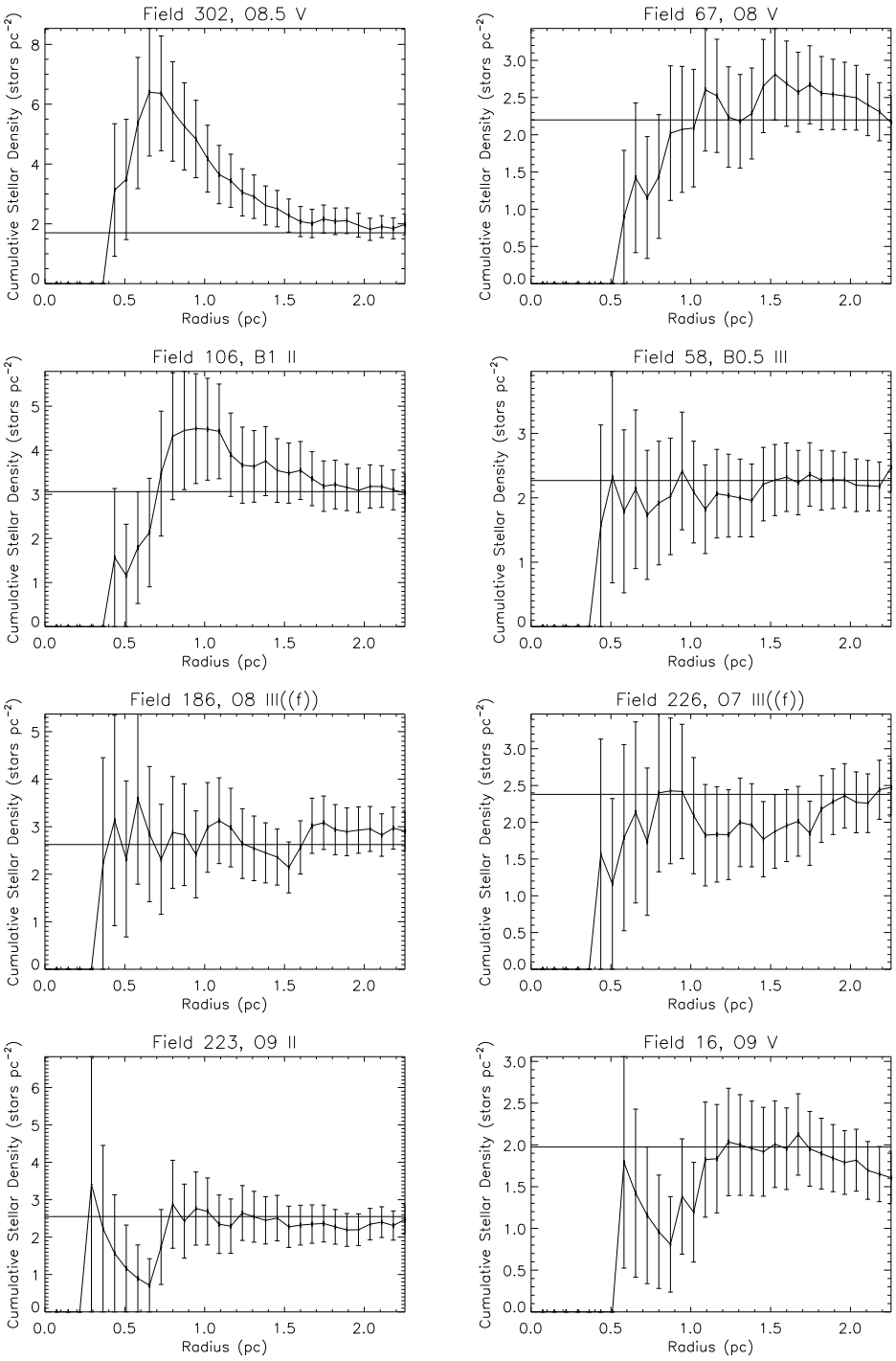

Figure 2.2. Cumulative stellar density as a function of radius from each target star. Each field is titled with the target star's ID and spectral type. The panels are shown in the same sequence as in Figure 2.1, with the first three stars showing a stellar density enhancement.

Field	Angular Size ($''$)	$R_{\rm cl}$ (pc)	$P(f)$	l (pc)	Field IMF
smc16	...	...	...	0.52	$\Gamma = -0.9 \pm 0.5$
AzV 58	...	...	...	0.43	$\Gamma = -1.2 \pm 1.1$
AzV 67	10.3	1.5	0.114	0.50	$\Gamma = -1.3 \pm 0.7$
AzV 106	6.9	1.0	0.047	0.43	$\Gamma = -1.6 \pm 1.3$
AzV 186	...	...	...	0.46	$\Gamma = -0.9 \pm 1.2$
AzV 223	...	...	...	0.47	$\Gamma = -1.1 \pm 0.5$
AzV 226	...	...	...	0.48	$\Gamma = -1.0 \pm 1.0$
AzV 302	4.8	0.7	0.0001	0.58	$\Gamma = -1.0 \pm 0.7$

Table 2.2. Cluster and Stellar Population

well by normal distributions, and so we used gaussian functions to estimate l. Figure 2.3 shows a representative example. The average l for these observations is 0.48 ± 0.05 parsecs. Table 2.2 lists the clustering length of each field in column 5.

2.2.2 Minimal O Star Groups

As seen from the data in Figure 2.2 and Table 2.2, there are three stars that show robust evidence of small, associated stellar groups: AzV 67, AzV 106, and AzV 302. The field probabilities, $P(f)$, for these targets range from 0.01% to 11.4%. The friends-of-friends algorithm confirms the existence of stars within the clustering length l in each of these fields. To examine the sensitivity to l, we also ran the friends-of-friends code with values of $l \pm 0.05$ pc, where this variation is equal to the standard deviation of l in the sample (see above). For the smaller values, this yielded companions only for AzV 302; while the larger value resulted in associated stars for all targets in our sample. Thus, we are confident that the fitted peak values for l are appropriate, and they support the identification of groups found by identifying density enhancements. We will refer to these sparse groups as "minimal O star groups". AzV 186 is the only field to appear clustered using the friends-of-friends algorithm, but not the density enhancement algorithm. We identify only those fields that appear clustered using both algorithms, as minimal O star groups.

2.2.3 Isolated Field Stars

The remaining four targets (AzV 58, AzV 223, AzV 226, smc16) show no evidence of associated stars using either of the methods above. These are candidates for massive

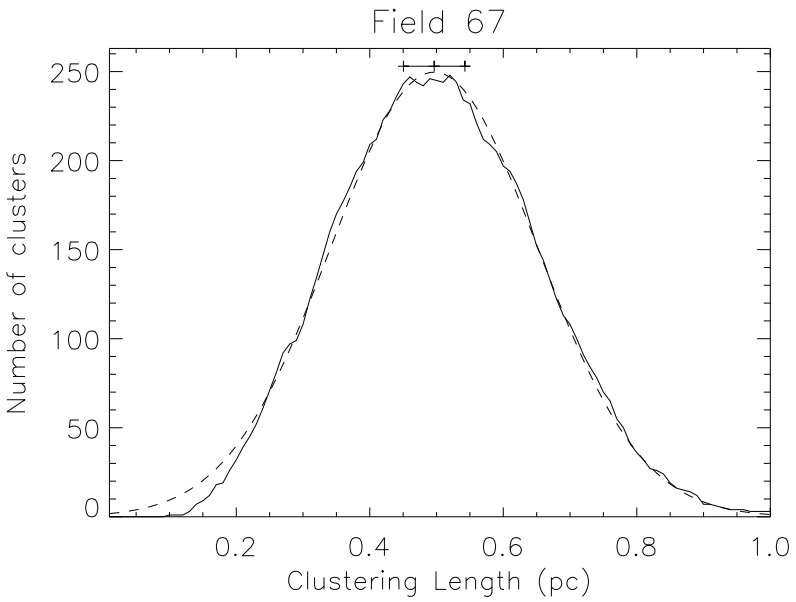

Figure 2.3. Number of clusters vs. clustering length, l, with a fitted Gaussian (dashed line) for a representative field, AzV 67. The bar shows the extent between one standard deviation below and above the peak value, and indicates the three values used for l for each field.

stars that formed in complete isolation. However, a substantial fraction of field O stars likely did not originate in the field at all, but rather are runaway stars from clusters (e.g., Blaauw 1961; Gies 1987; Hoogerwerf et al. 2001). Thus, we examine the likelihood that our isolated OB stars are runaways.

We are performing a complete spectroscopic survey of SMC field OB stars that is now underway, using primarily the IMACS multi-slit spectrograph on the 6.5-m Magellan/Baade telescope at Las Campanas Observatory (Lamb et al, in preparation). These data yield the stellar radial velocities and spectral classifications, and we will ultimately estimate the runaway fraction for these massive field stars. In the course of this survey, we obtained spectra of the target field OB stars in our *HST* imaging sample. Table 2.1 gives our measured heliocentric radial velocities and spectral classifications. Several stars were previously classified, and we either confirmed or revised the spectral types, as shown.

We identify two of these stars, smc16 and AzV 223, as runaways, defined as stars having ≥ 30 km s^{-1} difference (de Wit et al. 2005) from the SMC systemic velocity

of 155 km s^{-1} (Staveley-Smith et al. 1997). We note that Stanimirović et al. (2004) found the SMC to have a velocity gradient; however, the positions of our targets do lie between the 150 km s^{-1} and 160 km s^{-1} contours as plotted in Figure 3 of Stanimirović et al. (2004). The two runaway stars will be removed from analysis in all subsequent sections, since they are no longer located in the region of their formation. This leaves us with two, isolated, apparently non-runaway OB stars, AzV 58 and AzV 226. Assuming an isotropic distribution of runaway velocities, we still expect to miss a number of transverse runaways. The missed fraction depends on the velocity distribution of runaway stars; however, we estimate that typical ejection velocities of 60 km s^{-1} or 120 km s^{-1} would cause us to miss two or one transverse runaway(s), respectively. Therefore, transverse runaways may account for both our remaining isolated stars.

It is also informative to investigate the interstellar gas around these field OB stars (Figure 2.4). We examined the ionized gas around our target stars, using Hα data from the Magellanic Cloud Emission Line Survey (MCELS; Smith et al. 2000). Since gas is a necessary component of star formation, the presence of gas can help to constrain which stars may still be in the region of their formation. As a control group, all three of our minimal O star groups show Hα emission within 2.0′ (35 pc), consistent with a physical association within these groups as sparse, young clusters. We also find that both confirmed runaway stars are far removed from any Hα emission. For the remaining isolated targets, the MCELS data show that AzV 58 and AzV 226 are located within HII regions in the line of sight (Figure 2.4), while AzV 186 is far from any HII regions. These results suggest that AzV 58 and AzV 226 may still be in the region of their formation and thus they remain candidates for isolated massive star formation.

2.2.4 The IMF

We construct color-magnitude diagrams (CMD's) from our ACS photometry, and use these to evaluate the IMF for the minimal O star groups as well as the field stars. We converted the photometric results from the F555W and F814W bands

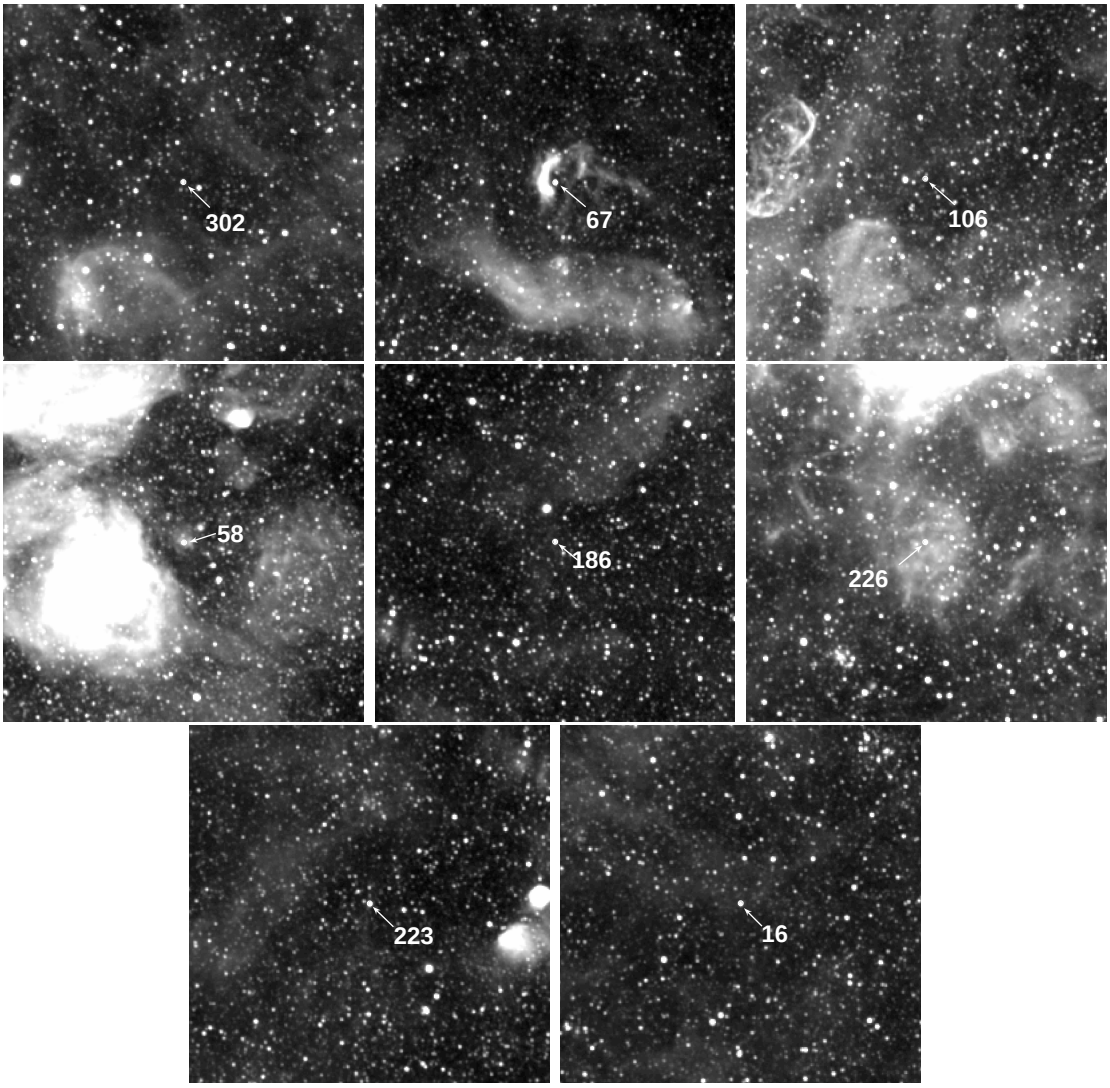

Figure 2.4. Hα images from the Magellanic Cloud Emission Line Survey (MCELS), tracing the ionized gas in the region around each target star. The PSF of these observations is similar to the 1 parsec circles in Figure 2.1, and the field of view is $9' \times 9'$. The panels are sequenced as in Figure 2.1, with the top row showing fields with a stellar density enhancement. The target stars are identified.

to Johnson V and Cousins I bands, respectively, following the synthetic transfer equations provided in Sirianni et al. (2005). These V and I band magnitudes were then extinction corrected using the SMC extinction maps provided by the Magellanic Cloud Photometric Survey (MCPS; Zaritsky et al. 2002). MCPS provides two sets of stars for estimating extinction, the "hot" stars ($12,000$ K $\leq T_{eff} \leq 45,000$ K) and "cool" stars ($5,500$ K $\leq T_{eff} \leq 6,500$ K). We chose to average the extinction values of "cool" stars within $1'$ of the target star for the extinction calculation, as these objects better trace the sparse field population of our observations. The "hot" stars tend to trace active, clustered star formation with high gas content, yielding extinction values up to half a magnitude higher than those typically found in the "cool" stars.

We then calculated absolute magnitudes using a distance modulus of 18.9 (Harries et al. 2003). Comparisons of our photometry with MCPS photometry typically show differences less than 0.1 mag, with I-band matching more closely than V. On average, our photometry appears fainter than that of the MCPS in both V and I bands. For stars fainter than 16th magnitude, Zaritsky et al. (2002) find that stellar crowding may play a factor in spuriously brightening the MCPS photometry when compared with the OGLE catalog (Udalski et al. 1998), which they deem to be superior in this regime. Since nearly all stars in our fields are fainter than 16th magnitude, the difference between our photometry and MCPS photometry is likely due to these crowding effects.

We used Geneva stellar evolutionary tracks to extract mass estimates from our photometry. These tracks are based on the ATLAS9 no-overshoot models at SMC metallicity, calculated by Charbonnel et al. (1993) and have been converted by Girardi et al. (2002) to Johnson-Cousins $UBVRI$ photometry. The stellar masses are inferred by identifying the two evolutionary tracks between which a star falls, on the V vs $V-I$ CMD. For the extremely blue, O and B target stars, the $V-I$ colors are degenerate, so effective temperature, $T_{\rm eff}$, is used instead of $V-I$ color. $T_{\rm eff}$ of our OB target stars are based on our spectral classifications given in Table 2.1, using the conversions of spectral type to effective temperature for the SMC by Massey et

al. (2005) for the O stars, and Crowther (1997) for the B stars.

Following the formalism of Scalo (1986) and analysis done by Massey (1995), we write the slope of the IMF as:

$$\Gamma = d\log\xi(\log m)/d\log m \tag{2.3}$$

where $\xi(\log m)$ is the mass function in units of stars born per logarithmic stellar mass m ($M_\odot$) per unit area (kpc^2) per unit time (Myr). This corresponds to a power-law mass spectrum given by:

$$n(m)\ dm \propto m^\gamma dm \tag{2.4}$$

where $n(m)\ dm$ is the number of stars per unit mass bin and the power law index $\gamma = \Gamma - 1$. In this formalism, a Salpeter mass function has a slope $\Gamma = -1.35$. In order to derive $\xi(\log m)$, we counted the stars in each mass bin, corrected for the size of the mass bin by normalizing to one dex in mass, and divided by the area covered by the observations. For computing the IMF of the background field, we divided by the average age of stars within each mass bin (Charbonnel et al. 1993) to account for differences in stellar lifetimes as a function of mass. Ages were calculated as an average between the lower and upper mass in each bin, weighted by the IMF. This allowed us to measure an IMF under the assumption of continuous star formation, rather than obtaining the present-day mass function of the field.

The CMD and IMF for a representative, full field, that of AzV 67, are shown in Figure 2.5. On the CMD plot, we draw SMC-metallicity evolutionary tracks (Charbonnel et al. 1993; Girardi et al. 2002) to show the stellar mass ranges of the field population. On the IMF plot, the error bars represent the Poisson uncertainty for each mass bin. The detection limit is $V = 22$ in the F555W image, which corresponds to a mass of $1.5M_\odot$. The observations are incomplete up to $2M_\odot$. On the IMF plot, points corresponding to stellar mass bins below $2M_\odot$ are excluded from the linear fitted line, which has been made weighting the data inversely by the errors. The IMF slopes for the field population in each full, $202'' \times 202''$ ACS frame are given in Table 2.2, column 6. Accounting for the stellar age correction, each field exhibits an IMF

O Star Group	RA	Dec	V	I
AzV 67	00:50:10.39	-72:32:30.9	20.78 ± 0.15	20.77 ± 0.06
AzV 67	00:50:11.77	-72:32:30.0	19.85 ± 0.07	19.79 ± 0.03
AzV 67	00:50:11.95	-72:32:32.3	20.51 ± 0.13	20.67 ± 0.06
AzV 106	00:51:43.45	-72:37:27.3	19.51 ± 0.05	19.58 ± 0.02
AzV 106	00:51:44.02	-72:37:23.9	21.20 ± 0.20	21.15 ± 0.08
AzV 302	01:02:18.74	-72:22:04.7	19.76 ± 0.08	19.52 ± 0.03
AzV 302	01:02:18.81	-72:22:01.1	20.84 ± 0.16	20.68 ± 0.06
AzV 302	01:02:18.83	-72:22:01.7	17.97 ± 0.02	17.98 ± 0.01
AzV 302	01:02:19.40	-72:22:02.2	20.81 ± 0.16	20.46 ± 0.04

Table 2.3. Photometry of Companion Stars

consistent with a Salpeter IMF, within the uncertainty.

Due to the small number of cluster members identified in both the F814W and F555W exposures, it is not useful to derive IMFs for the three minimal O star groups individually. Instead, we created a composite CMD of all members from the three groups. Because of field star contamination, only a subset of the stars comprising these density enhancements are physically associated; the background field star density implies a contamination of $1 - 2$ stars per target frame. In deriving the IMF of these minimal O star groups, we exclude red giants, since they are certainly field stars unassociated with recent star formation. Some main sequence stars may also be field star contaminants, but they are indistinguishable from true cluster members. Table 2.3 provides photometry of the main sequence companion stars present in both V and I images, above the completeness limit of $V = 21$ and $I = 22$ magnitudes. Columns 1 and 2 list the right ascension and declination, while Columns 3 and 4 list the V and I magnitudes.

Figure 2.6*a* shows the CMD for all companions found using the density enhancement analysis. The CMD for companions found using the friends-of-friends algorithm is identical to that in Figure 2.6*a* above our completeness limit of $2M_{\odot}$. We plot the composite IMF of these minimal O star groups in Figure 2.6*b*, excluding all mass bins below our completeness limit. We find one companion star in each of the mass bins, $2M_{\odot} \leq m < 2.5M_{\odot}$, $2.5M_{\odot} \leq m < 3M_{\odot}$, and $3M_{\odot} \leq m < 4M_{\odot}$. Upon generating IMFs of the companions found in the friends-of-friends analysis with clustering lengths $l \pm 1\sigma$, we find that changing the exact prescription for determining

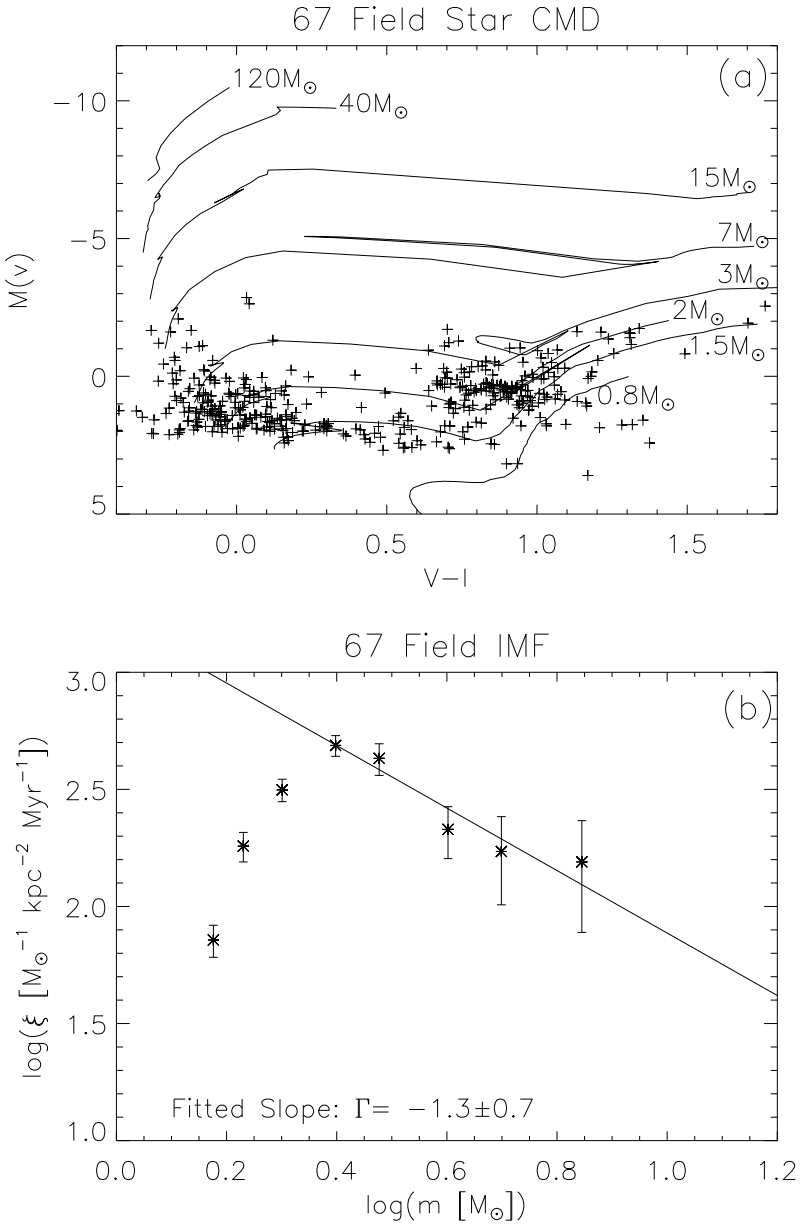

Figure 2.5. (*a*) Color-magnitude diagram and (*b*) field IMF for a representative field, AzV 67. Each of our observed fields is consistent with the Salpeter IMF within the uncertainty. The error bars represent the Poisson uncertainties. Mass bins below our completeness limit of $2M_{\odot}$ are excluded from the fitted line.

companionship has little effect on the measured IMF for this population of minimal O star groups.

The IMF slope for the composite population in the minimal O star groups varies between $\Gamma = 0.1 \pm 1.0$ to -0.2 ± 0.9 in the preceding analysis, which is not far from a Salpeter slope of $\Gamma = -1.35$ within the uncertainties. However, the true slope may be even larger, since we do not correct for contamination by main sequence field stars. Due to the presence of very massive stars and a small number of low-mass companions, the IMF is essentially predetermined to be unusually shallow, but we note that it does not necessarily represent a significant variation from the Salpeter value, statistically, given the small numbers of stars.

2.3 Monte Carlo Simulations

This regime of sparse star formation is strongly dominated by stochastic effects and, as described in §1, it offers an important discriminant between star formation theories. A fundamental question is whether the stellar IMF in clusters is largely independent of parent cloud mass, and determined by only the most local physics (e.g. Maschberger & Clarke 2008; Krumholz et al. 2010). If so, the IMF in the lowest-mass clusters remains identical to that seen in higher-mass clusters, and should be described by the simple random drawing of discrete stars from an IMF represented as an ordinary probability density function. On the other hand, a scenario that is at least as plausible is that the IMF is driven by, and limited by, the mass of the parent molecular cloud (e.g. Bonnell et al. 2004; Weidner & Kroupa 2004). If so, then the stochastic effects seen in the lowest-mass clusters will be linked to the parent cloud masses. The objects in our study offer a unique opportunity to explore this extreme parameter space.

2.3.1 Analytic Probability

We can quantify the likelihood that these minimal O star groups conform to a standard but under-sampled stellar IMF. For a cluster of N_* stars, the probability that

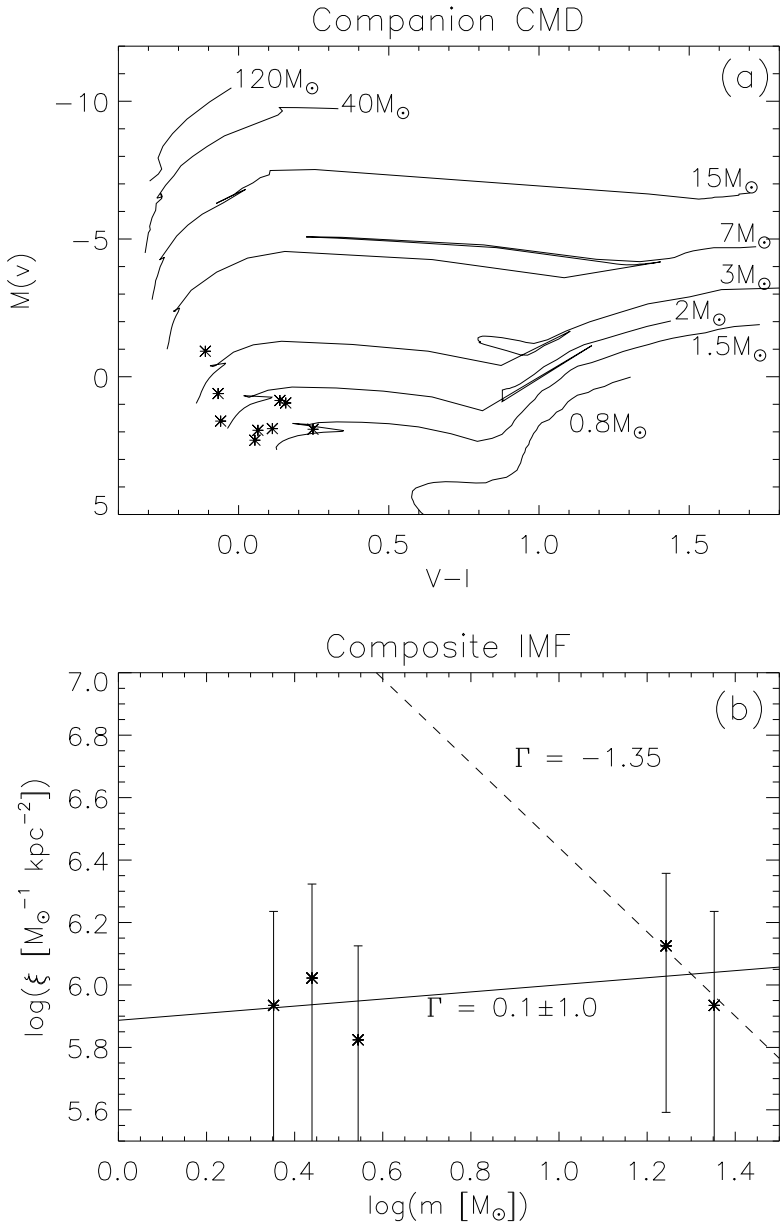

Figure 2.6. Shown in panel (a) is the CMD of the minimal O star groups with membership determined by the stellar density analysis. Panel (b) shows the IMF of the minimal O star groups including companions down to our completeness limit of $2M_{\odot}$ for the F555W band. We plot a solid line, fit to the data, with $\Gamma = 0.1 \pm 1.0$. For reference, a dashed line with $\Gamma = -1.35$, representing a Salpeter slope, is shown.

all stars are below mass $m_{\rm max}$ is given by:

$$P(m_{\rm max}, N_*) = \left[\int_{m_{\rm min}}^{m_{\rm max}} \phi(m)\, dm \right]^{N_*} \quad , \tag{2.5}$$

where $\phi(m)$ is the IMF and $m_{\rm min}$ is its lower mass limit, which we assume to be constant. We adopt a Kroupa IMF (Kroupa 2001), whose form is:

$$\phi(m)dm \propto \begin{cases} m^{-1.3}dm \ , \ 0.08M_\odot \leq m < 0.5M_\odot \\ m^{-2.35}dm \ , \ 0.5M_\odot \leq m < 150M_\odot \end{cases} \tag{2.6}$$

For the minimal O star groups, we estimated N_* as follows. We count the candidate member stars, identified as described in §§2.1 – 2.2, and correct for the expected number of field stars contaminating the cluster line of sight. The contamination is determined by the stellar density of the background field as calculated in §2.2.1 and the angular size of the cluster (Table 2.2). We further correct the observed numbers to account for stars below our completeness limit of $1.5M_\odot$ in the F814W images to get a final N_* estimate over the full mass range of the IMF. Table 2.4 lists star counts for each field as follows. Column 1 shows the star ID; columns 2 and 3 show the total number of stars observed within the cluster raduis and the subset of those estimated to be field stars, respectively; column 4 lists the resulting number of cluster members above the detection threshold; and column 5 lists the inferred N_*, integrating over the full stellar mass range from $m_{\rm lo} = 0.08M_\odot$. We follow a similar process to estimate cluster mass by summing the masses of all stars in the cluster and again integrating below our completeness limit down to $m_{\rm lo} = 0.08M_\odot$. The cluster mass estimates are listed in column 6 and will be utilized for analysis in § 2.5.

We then use these N_* values and the $m_{\rm max}$ values from Table 2.1 to calculate $P(m_{\rm max}, N_*)$ (equation 2.5). These values are given in column 7 of Table 2.4. For the minimal O star groups, we find that the likelihoods of these clusters containing stars as massive as those observed range from 11 to 20%. In the case of those isolated O stars with no observed companions, and assuming that all cluster members are below our detection threshold, the likelihoods that the observed stars formed with

Star	Observed Stars	Field Stars	Detected Members	Estimated N_*	Estimated $M_{\rm cl}(M_\odot)$	$P(m_{\rm max}, N_*)$
AzV 58	1	0	1	$\leq$19	$\leq$43	$\leq$0.03
AzV 67	24	15	9	171	103	0.11
AzV 106	17	9	8	152	72	0.20
AzV 186	1	0	1	$\leq$19	$\leq$72	$\leq$0.01
AzV 226	1	0	1	$\leq$19	$\leq$77	$\leq$0.01
AzV 302	13	3	10	190	81	0.19

Table 2.4. Observed and Estimated Cluster Membership

no companions above $1.5M_\odot$ ranges from upper limits of $\leq$1% to $\leq$3% (Table 2.4). These likelihoods, while low, are not exceedingly so, suggesting that the occurrence of these minimal O star groups, even those with no stars above the detection threshold, is not especially unlikely given the assumed parameters. Our target selection was based on apparent isolation in ground-based imaging, and so we expect our objects to fall in this low-probability regime. As a reminder, we note that these probabilities are based on maximized numbers of stars below the detection limit, in all cases.

2.3.2 Numerical Simulations

We now devise Monte Carlo simulations that generate clusters and cluster members to explore the frequency of the observed minimal O star groups in the context of a stellar clustering law or cluster mass function.

We simulate the scenario for which the IMF is completely independent of cluster mass. We generate clusters using a stellar clustering law having a default $\beta = -2$ power law slope (hereafter the "N_* simulations"):

$$n(N_*)\ dN_* \propto N_*^{\beta}\ dN_* \quad , \tag{2.7}$$

where $n(N_*)\ dN_*$ is the number of clusters in the range N_* to $N_* + dN_*$. We set single stars, $N_* = 1$, as our minimum "cluster" and set an upper limit for clusters at $N_* = 10^6$. Our use of the –2 power law index is motivated by observations of a wide variety of stellar populations including young, massive clusters (e.g., Hunter et al. 2003; Zhang & Fall 1999; Fall et al. 2009), super star clusters (Meurer et al. 1995), globular clusters (e.g., Harris & Pudritz 1994), and HII regions (Oey & Clarke 1998).

Oey et al. (2004) found that this power law applies smoothly down to individual field OB stars, and we assume that the same clustering law holds true for all stellar masses, down to our lower mass limit of $0.08 M_{\odot}$.

Once clusters are generated following the N_* clustering law (equation 2.7), each cluster is randomly populated with stars using the IMF given by equation 2.6. The IMF, including its stellar mass limits, is constant for all clusters, thereby allowing true, isolated O stars to be generated in $N_* = 1$ "clusters". For each N_* simulation, up to 10^7 clusters are generated to ensure that we create enough clusters to fully populate the cluster parameter space.

We also carry out simulations that generate clusters by total cluster mass $M_{\rm cl}$, according to essentially the same power-law distribution (hereafter the "$M_{\rm cl}$ simulations"):

$$n(M_{\rm cl})\ dM_{\rm cl} \propto M_{\rm cl}^{\beta}\ dM_{\rm cl} \quad , \tag{2.8}$$

where $n(M_{\rm cl})$ is the number of clusters in the range $M_{\rm cl}$ to $M_{\rm cl} + dM_{\rm cl}$. We adopt an upper limit to the cluster mass function of $10^5 M_{\odot}$.

Most simulations of clusters heavily favor this method of populating clusters by mass (e.g. WK06; Parker & Goodwin 2007; Haas & Anders 2010). However, the exact prescription for populating stars up to the target $M_{\rm cl}$ varies. For our simulations, we follow Parker & Goodwin (2007) by populating the cluster with stars, randomly sampled from the IMF, until the cluster contains at least 98% of its target mass in stars. At this point, if the last star generated pushes the cluster mass past 105% of the target cluster mass, the entire cluster is discarded. The process of populating the cluster with stars is repeated until the total stellar mass falls within 98% to 105% of the target cluster mass. If these conditions are not imposed, the high-mass stars are too often generated as the last star in the cluster, and the cluster mass function is not well preserved in the final sample of clusters. An investigation of the effects on cluster population using different algorithms can be found in WK06 and Haas & Anders (2010).

We also perform variations of our simulations using $\beta = -1.8$ and –2.3 power law

slopes. These are values typically observed as empirical variation for real systems. For example, observations of giant molecular clouds (GMCs) and self-gravitating clumps within GMCs show power-law mass distributions with slopes $\beta \sim -1.7$ (see Bertoldi & McKee 1992; Rosolowsky 2005). Observations of star clusters in the Large Magellanic Cloud show measured values of $\beta \sim -2.0$ to –2.3 (Hunter et al. 2003) and $\beta \sim -1.8$ (Chandar et al. 2010). Allowing β to vary in our simulations allows us to explore its effect on our results.

2.3.3 The Cluster Lower-Mass Limit

Our cluster simulations are designed to probe the limiting case of sparse O star formation. A critical parameter in this regime is the lower limit placed upon cluster mass or membership number.

With respect to quantized star counts, observational evidence for a –2 power law relation extending to $N_* = 1$ clusters are limited to samples of O and OB stars, probing stellar masses $\geq 20 M_\odot$ and $\geq 10 M_\odot$ (Oey et al. 2004). The form of the stellar clustering law for a complete sample of stars below these masses is unknown. Our simulations extrapolate this –2 power law relation to stellar masses two orders of magnitude lower than those observed. However, it is possible that the clustering law has a turnover or cutoff in the low number regime, or the –2 power law relation may break down at a stellar mass higher than our lower mass limit of $0.08 M_\odot$.

This low N_* regime exists in an intermediate stage between clustered formation and isolated formation, which Adams & Myers (2001) term "group formation". They estimate that the majority of star formation occurs in this group formation regime, with $N_* = 10$–100. They also estimate a lower bound of $N_* = 36$ for a group to evolve as a cluster, defined as having a relaxation time longer than the crossing time of the group. However, N-body simulations show that clusters in this "group formation" regime are likely to lose a significant portion of their stellar members on timescales of a few Myr (Bonnell & Clarke 1999). Interactions that cause the stellar losses preferentially affect low-mass stars, thus making the initial N_* a difficult parameter to estimate from observations for clusters in this regime. This effect may be present in

the embedded cluster catalog from Lada & Lada (2003), which restricts membership to clusters with $N_* \geq 35$ and shows a turnover in the cluster mass function below $50M_\odot$. Since the typical stellar mass is $\sim 0.5M_\odot$, the turnover that they observe in the cluster mass function at $50M_\odot$ corresponds to $N_* \sim 100$, right at the regime where the N-body simulations predicted stellar membership loss. Therefore, while the exact nature of the lower limit of the clustering law is still unknown, a truncation at a lower value of $N_{*,\rm lo}$ in the range from $\sim$35 to 100 stars or $M_{\rm cl}$ from $\sim$17.5 to $50M_\odot$ is reasonable. This lower limit is similar to that employed in previous cluster simulations, which typically range from $5M_\odot$ (Weidner & Kroupa, 2004) to $50M_\odot$ (Parker & Goodwin, 2007).

With respect to the cluster mass function, extragalactic studies of complete samples of clusters have probed to $M_{\rm cl} \sim 10^3 M_\odot$ (Chandar et al. 2010), limiting our knowledge of the form of the mass function for complete samples below this mass. Lada & Lada (2003) probe clusters below $10^3 M_\odot$ by compiling a catalog of embedded clusters in the solar neighborhood. Their results are consistent with a $M_{\rm cl}^{-2}$ cluster mass function for clusters from $50M_\odot$ to $10^3 M_\odot$. Below $50M_\odot$, they find a statistically significant turnover in the cluster mass function. This may indicate that the lower limit of our $M_{\rm cl}$ simulations should be truncated or the power law should turn over around a value $50M_\odot$.

In the next sections, we compare different simulations with observed statistics for SMC massive star clustering and isolated Galactic O stars. In this comparison, we include three separate lower N_* limits for the clustering law at $N_{*,\rm lo} = 1$, 40, and 100 stars, and two separate lower $M_{\rm cl}$ limits of the cluster mass function at $M_{\rm cl,lo} = 20M_\odot$ and $50M_\odot$. Since the typical stellar mass is $\sim 0.5M_\odot$, $N_{*,\rm lo} = 40$ is the appropriate equivalent lower limit for $M_{\rm cl,lo} = 20M_\odot$ and that for $M_{\rm cl,lo} = 50M_\odot$ is $N_{*,\rm lo} = 100$. While these values are empirically motivated, they do also allow the formation of stars $> 20M_\odot$, as required for our purposes. In what follows, it is important to bear in mind that the cluster parameterizations are extrapolated beyond observed mass ranges.

$M_{\rm cl,lo}$ or $N_{*,\rm lo}$	β	1 O star	2 O stars	>2 O stars	1 OB star	2 OB stars	>2 OB stars
				N_* Simulations[a]			
1	-1.8	0.75	0.10	0.151	0.73	0.11	0.16
40	-1.8	0.61	0.15	0.24	0.53	0.18	0.29
100	-1.8	0.53	0.18	0.29	0.40	0.20	0.40
1	-2.0	0.87	0.07	0.07	0.85	0.08	0.08
40	-2.0	0.70	0.15	0.15	0.61	0.18	0.21
100	-2.0	0.61	0.18	0.21	0.46	0.22	0.32
1	-2.3	0.96	0.03	0.02	0.95	0.04	0.02
40	-2.3	0.79	0.12	0.08	0.70	0.17	0.13
100	-2.3	0.69	0.18	0.14	0.53	0.23	0.24
				$M_{\rm cl}$ Simulations[a]			
$20M_\odot$	-1.8	0.56	0.15	0.29	0.53	0.16	0.31
$50M_\odot$	-1.8	0.54	0.16	0.30	0.44	0.19	0.37
$20M_\odot$	-2.0	0.67	0.14	0.19	0.63	0.16	0.21
$50M_\odot$	-2.0	0.64	0.16	0.21	0.52	0.20	0.28
$20M_\odot$	-2.3	0.78	0.12	0.10	0.74	0.14	0.12
$50M_\odot$	-2.3	0.75	0.14	0.12	0.61	0.20	0.19
				SMC Observed[b]			
...	...	0.61±0.08	0.19±0.04	0.19±0.04	0.65±0.04	0.15±0.02	0.19±0.02

a Errors for simulated values are ≤ 0.01
b From Oey et al. (2004).

Table 2.5. Fraction of O (OB) star clusters having a given number of O(OB) stars

Comparison with SMC Clustering Statistics

We compare the distribution of massive stars in the simulated clusters with the actual, observed distribution of stars among SMC clusters. Oey et al. (2004) broke down the clustering of observed, photometrically-identified massive star candidates with a friends-of-friends algorithm. They identified two samples, the "O-star sample" and the "OB-star sample," corresponding to masses $m \gtrsim 20M_\odot$ and $m \gtrsim 10M_\odot$, respectively. In our simulations, we consider only clusters containing one or more O or OB stars, defined by the same respective mass ranges. Table 2.5 summarizes our findings on massive star clustering. The rows are divided into three sections which denote results from the N_* simulations, the $M_{\rm cl}$ simulations, and the Oey et al. (2004) observations. For the simulations, $N_{*,\rm lo}$ or $M_{\rm cl,lo}$ is listed in column 1 and the power law slope is listed in column 2. Columns 3, 4, and 5 list the frequencies of having one, two, or more than two O stars, respectively, in the clusters; while columns 6, 7, and 8 list these frequencies for OB stars in the clusters.

Table 2.5 reveals three trends: (1) steepening the power law slope of the simulation

results in an increasing fraction of O or OB star clusters containing a single O or OB star, (2) the fraction of OB star clusters with a single OB star is lower than the fraction of O star clusters with a single O star and (3) the N_* simulations are more sensitive to the lower limit truncation than the $M_{\rm cl}$ simulations. The final trend is due to our cluster population method. In the case where $M_{\rm cl} < m_{\rm up}$, stars with mass greater than $M_{\rm cl}$ will not be allowed to form in such a cluster in the $M_{\rm cl}$ simulations. However, in the N_* simulations, each cluster can form stars up to $m_{\rm up}$.

In the observations by Oey et al. (2004), 61–65% of clusters having at least one massive star contain only a single massive star. We find best agreement with this fraction in our simulations following a –2 power law slope and a truncation of $N_* = 40$ or $20 M_\odot$. Table 2.5 also shows good agreement with $\beta = -1.8$ for the N_* simulation having a truncation of $N_* = 20$. For $\beta = -2.3$, the steepness of the slope causes the OB cluster sample and O star cluster sample to behave differently enough from each other that they cannot both be in agreement with the observations, regardless of the lower limit. Similarly, at a truncation of $N_* = 100$ or $M_{\rm cl} = 50 M_\odot$, the OB cluster sample and O star cluster sample never come into agreement simultaneously at the same power law slope.

Comparison with Galactic Isolated O Star Fraction

We also compare our simulations to the de Wit et al. (2005) result that 4±2% of all Galactic O stars are found in isolation. The simulations by Parker & Goodwin (2007) are in agreement with this result. Since we modeled our $M_{\rm cl}$ simulations after their work, our results should match theirs quite closely, although the exact parameters of the simulations differ slightly. Parker & Goodwin (2007) set the lower mass limit of the stellar IMF to $0.1 M_\odot$, while our simulations use a value of $0.08 M_\odot$. Also, Parker & Goodwin use a lower limit of $M_{\rm cl} = 50 M_\odot$, while we vary the limit as discussed above. For comparison with this study, we adopt the de Wit et al. (2005) definition of O stars as having mass $\geq 17.5 M_\odot$. This comparison provides a good check for our results and also quantifies the effect of the lower limit, $M_{\rm cl,lo}$ or $N_{*,\rm lo}$, on the isolated O star fraction.

Parker & Goodwin's definition of an isolated O star is twofold: first, the cluster contains no B stars with mass $\geq 10M_{\odot}$ and second, the total cluster mass $M_{\rm cl} < 100M_{\odot}$. These constraints were set according to the detection limits of the de Wit et al. (2005) result and are intended to mimic the sensitivity of those observations. For the following analysis, we follow Parker & Goodwin's definition of O star isolation. The results of this analysis are shown in Table 2.6, which has rows divided between the N_* simulations, the $M_{\rm cl}$ simulations, and the de Wit et al. (2005) observations. $N_{*,\rm lo}$ or $M_{\rm cl,lo}$ for the simulations is listed in column 1, the power law slope for the simulations is listed in column 2, and the fraction of isolated O stars as a fraction of all O stars is listed in column 3. This table reveals trends similar to those seen in Table 2.5, that steepening the power law slope increases the fraction of isolated O stars, and that the N_* simulations are more sensitive to the lower limit truncation than the $M_{\rm cl}$ simulations. Table 2.6 also shows that the fraction of isolated O stars matches very well between the N_* and $M_{\rm cl}$ simulations having lower limits of $N_{*,\rm lo} = 40$ and $M_{\rm cl,lo} = 20M_{\odot}$, respectively.

For their simulation adopting a –2 power law slope, Parker & Goodwin find that 4.6% of O stars are isolated, in good agreement with the 4±2% result from de Wit et al. (2005). We find that many of our simulations match the de Wit et al. (2005) result, spanning the full range of lower limits and power law slopes tested, with the exception of $N_{*,\rm lo} = 1$. Table 2.6 shows that the –2 power law simulations that best agree with the isolated O star fraction have the higher values of $M_{\rm cl,lo} = 50M_{\odot}$ or $N_{*,\rm lo} = 100$, whereas the simulations that best agree with the SMC O and OB star clustering have the lower values of $M_{\rm cl,lo} = 20M_{\odot}$ or $N_{*,\rm lo} = 40$ (Table 2.5). Simulations following a –2.3 power law slope are least reconcilable with both sets of observations.

Default Clustering Models

In §§2.3.3 and 2.3.3, we find that a number of our simulations in both N_* and $M_{\rm cl}$ agree with observed statistics of SMC massive star clustering and Galactic isolated O stars. The N_* simulations are more sensitive to both the power law slope and $N_{*,\rm lo}$,

$M_{\rm cl,lo}$ or $N_{*,\rm lo}$	β	Iso. Fraction[b]
N_* Simulations		
1	-1.8	0.099
40	-1.8	0.029
100	-1.8	0.008
1	-2.0	0.330
40	-2.0	0.083
100	-2.0	0.022
1	-2.3	0.728
40	-2.3	0.212
100	-2.3	0.057
$M_{\rm cl}$ Simulations		
$20M_\odot$	-1.8	0.027
$50M_\odot$	-1.8	0.019
$20M_\odot$	-2.0	0.072
$50M_\odot$	-2.0	0.048
$20M_\odot$	-2.3	0.190
$50M_\odot$	-2.3	0.123
Galactic Observed[c]		
...	...	0.04±0.02

a Here, the definition of isolated O stars is from Parker & Goodwin (2007).
b Errors for simulated values are ≤ 0.01.
c From de Wit et al. (2005).

Table 2.6. Fraction of isolated O stars

and many models agree with these two sets of observations (Tables 2.5 and 2.6). But for the $M_{\rm cl}$ simulations, we find that only the $\beta = -2.0$ models match with both sets of observations, albeit for different $M_{\rm cl,lo}$ lower limits. For the –1.8 and –2.3 power law slopes, none of the simulations can appropriately match both the SMC O and OB clustering simultaneously for a given $N_{*,\rm lo}$ or $M_{\rm cl,lo}$, making a strong case for $\beta = -2.0$ models as the best choice for the power law slope.

We therefore take the –2.0 power law as the base model for comparison between the $M_{\rm cl}$ and N_* simulations. From Table 2.5 we find that models with $N_{*,\rm lo} = 40$ and $20 M_\odot$ best match the SMC massive star clustering observations, while Table 2.6 shows that models with lower limits at $N_{*,\rm lo} = 100$ and $M_{\rm cl,lo} = 50 M_\odot$ best match the isolated Galactic O star observations. Looking further, in Table 2.5 we see that the models with truncations at $N_* = 100$ and $M_{\rm cl} = 50 M_\odot$ also match well with SMC O star clustering, but do not agree with SMC OB star clustering, with the fraction of single OB star clusters being off by $\sim 10\%$. This difference is large compared to the fraction of isolated O stars for the models with $N_{*,\rm lo} = 40$ and $M_{\rm cl,lo} = 20 M_\odot$, which agree with the observations within $\sim 1 - 2\%$. Thus, we conclude that the simulations that best match both the SMC massive star clustering statistics and the fraction of isolated Galactic O stars are the N_* simulation with $N_{*,\rm lo} = 40$ and the $M_{\rm cl}$ simulation with $M_{\rm cl,lo} = 20 M_\odot$. We cannot rule out either N_* or $M_{\rm cl}$ in favor of the other and do not find evidence that either one is a more fundamental parameter.

In the following sections, we compare these two simulations with our observations of minimal O star groups. For this comparison we use the $M_{\rm cl}^{-2}$ and N_*^{-2} simulations with $M_{\rm cl,lo} = 20 M_\odot$ and $N_{*,\rm lo} = 40$, respectively, as our default models.

2.4 Stellar mass ratio $m_{\rm max,2}/m_{\rm max}$

A simple and important parameter we can compare between our observations and simulations is $m_{\rm max,2}/m_{\rm max}$, the mass ratio of the second-most massive and most massive stars in the cluster. This ratio is a directly observable quantity that we can measure for the minimal O star groups, and as such, provides a powerful parameter to use as a comparison between our observations and simulations.

There are two populations in the simulation that are of interest: (1) clusters that contain one or more O stars and (2) clusters that contain just one O star. We explore the full simulation parameter space of the mass ratio $m_{\rm max,2}/m_{\rm max}$ as a function of $m_{\rm max}$ in Figures 2.7 and 2.8. For Figures 2.7 and 2.8, panel (a) includes simulated clusters with at least one O star in the cluster, while panel (b) includes only simulated clusters with exactly one O star. For these plots and all subsequent simulations, we adjust our definition of O stars to be $m \geq 18M_{\odot}$ instead of our earlier $20M_{\odot}$ definition, allowing our lowest-mass target stars to be included in the parameter space when calculating percentile frequencies below. Since the uncertainty in our stellar mass estimates is $1M_{\odot}$ to $3M_{\odot}$, our adjusted definition is on the order of the uncertainty. The simulated clusters plotted in these figures are the O star clusters taken from a random sample of 573 simulated OB clusters, the same number of OB clusters as observed in the SMC, having at least one OB star ($m \geq 10M_{\odot}$; Oey et al. 2004). In these and all subsequent figures, we exclude clusters without O stars from the plots. The color coding in Figures 2.7 and 2.8 indicates the number of stars per cluster, with black indicating $0 \leq \log N_* < 1$, red indicating $1 \leq \log N_* < 2$, orange indicating $2 \leq \log N_* < 3$, green indicating $3 \leq \log N_* < 4$, and blue indicating $4 \leq \log N_* < 5$. Observations from this paper are plotted as black squares. For our apparently isolated O stars, we note that undetected companions may exist, having individual masses up to $1.5M_{\odot}$, and so we plot their $m_{\rm max,2}/m_{\rm max}$ as upper limits.

Our observations lie in an interesting region of the parameter space in both the $M_{\rm cl}$ and N_* simulations. There is a strong drop-off in the population of simulated clusters having $m_{\rm max,2}/m_{\rm max} < 0.02$. This drop-off coincides with some of our observed isolated targets. Thus, the upper limits in $m_{\rm max,2}/m_{\rm max}$ for the isolated stars approach the extreme lower limit of the parameter space. All of our observations lie within the parameter space covered by simulated clusters.

To examine this quantitatively, we identify the subset of simulated clusters that correspond to the selection criteria of our observed stars and clusters. For each target star, we identify all simulated clusters having $m_{\rm max}$ within the uncertainty of the star's empirically-derived mass (Table 2.1). We also eliminate all simulated clusters

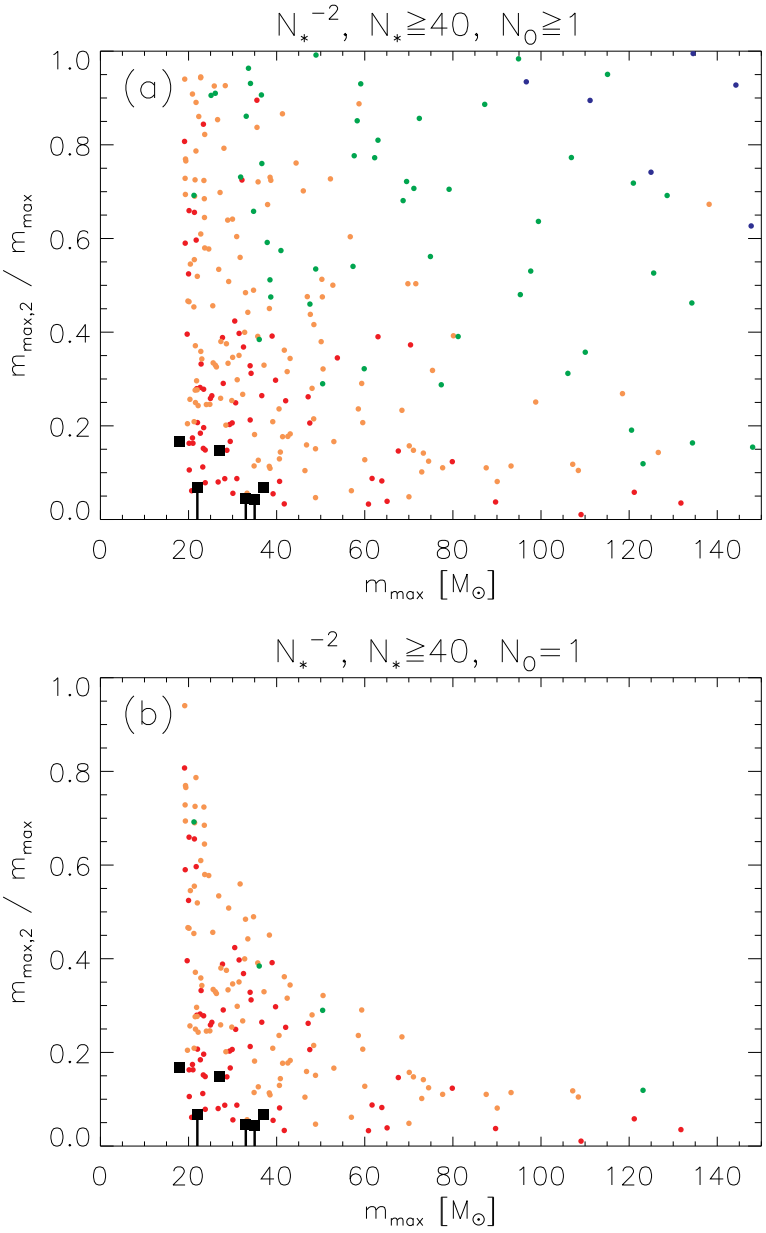

Figure 2.7. $m_{\rm max,2}/m_{\rm max}$ vs $m_{\rm max}$ from the N_*^{-2} simulation with $N_{*,\rm lo} = 40$ for (a) all clusters having at least one O star, and (b) all clusters having only a single O star. Data are color coded in logarithmic bins of N_*, with black $= 0 \leq \log N_* < 1$, red $= 1 \leq \log N_* < 2$, orange $= 2 \leq \log N_* < 3$, green $= 3 \leq \log N_* < 4$, and blue $= 4 \leq \log N_* < 5$. Our observations are plotted as black squares.

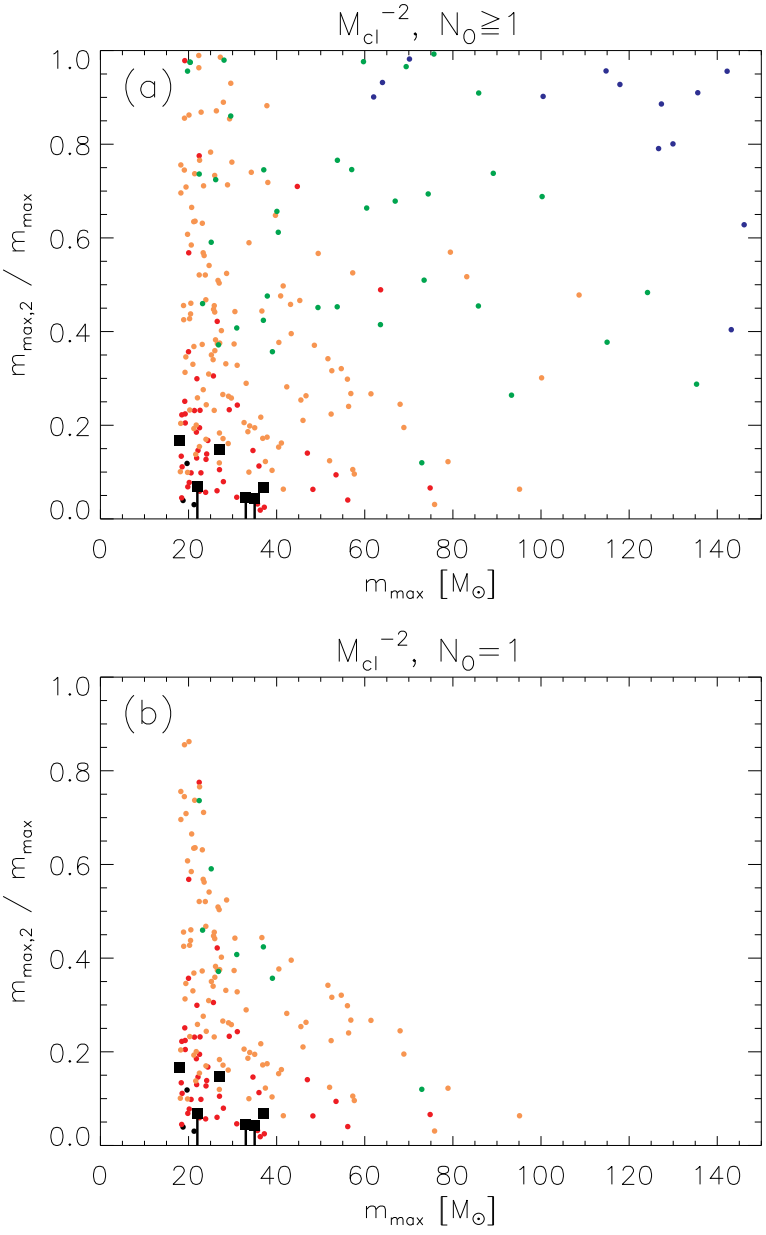

Figure 2.8. Same as Figure 2.7, but for the $M_{\rm cl}^{-2}$ simulation with $M_{\rm cl,lo} = 20 M_\odot$.

Star	$m_{\rm max}$ ($M_\odot$)	$(\frac{m_{\rm max,2}}{m_{\rm max}})_{obs}$	$N_*^{-1.8}$	N_*^{-2}	$N_*^{-2.3}$	$M_{\rm cl}^{-1.8}$	$M_{\rm cl}^{-2}$	$M_{\rm cl}^{-2.3}$	N_*^{-2}, $N_O \geq 1$	$M_{\rm cl}^{-2}$, $N_O \geq 1$
AzV 58	22	0.07	0.01	0.02	0.03	0.04	0.06	0.09	0.02	0.05
AzV 67	37	0.07	0.07	0.10	0.11	0.08	0.10	0.11	0.07	0.06
AzV 106	18	0.17	0.11	0.14	0.18	0.16	0.21	0.27	0.14	0.20
AzV 186	33	0.05	0.01	0.02	0.02	0.03	0.04	0.05	0.01	0.03
AzV 226	35	0.04	0.01	0.02	0.02	0.03	0.04	0.05	0.01	0.03
AzV 302	27	0.15	0.20	0.24	0.29	0.19	0.24	0.30	0.19	0.19

Table 2.7. Fraction of clusters with $[m_{\rm max,2}/m_{\rm max}]_{\rm sim} \leq [m_{\rm max,2}/m_{\rm max}]_{\rm obs}$

containing more than one O star, to obtain our final sub-sample of simulated clusters. For $m_{\rm max,2}$, we use the mass of the most massive observed, companion main-sequence star. In the case of our apparently isolated massive stars, we set $m_{\rm max,2}$ to an upper-limit value of $1.5M_\odot$, our F814W completeness limit. In the following analysis, we denote the observed $m_{\rm max,2}/m_{\rm max}$ as $[m_{\rm max,2}/m_{\rm max}]_{\rm obs}$ and that from simulated clusters as $[m_{\rm max,2}/m_{\rm max}]_{\rm sim}$. Table 2.7 lists the fraction of clusters with $[m_{\rm max,2}/m_{\rm max}]_{\rm sim} \leq [m_{\rm max,2}/m_{\rm max}]_{\rm obs}$ for each star. Column 1 lists the star ID; column 2 lists the mass of the OB star from Table 2.1; column 3 lists $[m_{\rm max,2}/m_{\rm max}]_{\rm obs}$; columns 4, 5, and 6 list the fraction of clusters with $[m_{\rm max,2}/m_{\rm max}]_{\rm sim} \leq [m_{\rm max,2}/m_{\rm max}]_{\rm obs}$ for the N_* simulations with $N_{*,\rm lo} = 40$, having slopes of –1.8, –2, and –2.3, respectively; and columns 7, 8, and 9 list these fractions for the $M_{\rm cl}$ simulations with $M_{\rm cl,lo} = 20M_\odot$, as shown. Columns 5 and 8 correspond to the simulated population in Figures 2.7*b* and 2.8*b*, respectively. Columns 10 and 11 are the same as Columns 5 and 8, respectively, except that they correspond to the simulated population in Figures 2.7*a* and 2.8*a*, showing all clusters with ≥ 1 O star.

Two trends emerge from these data: (1) steepening the power law slope increases the fraction of simulated clusters with $[m_{\rm max,2}/m_{\rm max}]_{\rm sim} \leq [m_{\rm max,2}/m_{\rm max}]_{\rm obs}$ and (2) the N_* simulations typically have a slightly lower fraction of simulated clusters having $[m_{\rm max,2}/m_{\rm max}]_{\rm sim} \leq [m_{\rm max,2}/m_{\rm max}]_{\rm obs}$ than the $M_{\rm cl}$ simulations. The first effect is caused by steeper slopes creating a greater fraction of small clusters, where stochastic effects can result in massive stars forming with only a few low mass companions. The second effect is caused by the fact that some of the clusters fall into the low $m_{\rm max,2}/m_{\rm max}$ regime in the $M_{\rm cl}$ simulation where $N_* < 40$, which is not allowed in the N_* simulation, due to our lower limit of $N_{*,\rm lo} = 40$. Looking specifically at the

$\beta = -2$ simulations, Table 2.7 shows that the frequency of single O star simulated clusters having $[m_{\rm max,2}/m_{\rm max}]_{\rm sim} \leq [m_{\rm max,2}/m_{\rm max}]_{\rm obs}$ for all observed groups is below the 25th percentile in both simulations, confirming the impression from Figures 2.7*b* and 2.8*b*. For all O star clusters from Figures 2.7*a* and 2.8*a*, our observed groups are all below the 20th percentile. Some of our isolated star observations are found in the lowest 5th percentile in both simulations, but still within the parameter space covered by the simulations.

That our observations are not well-distributed among the cluster population in Figures 2.7*b* and 2.8*b* is primarily due to our sample selection. Our selection process included a visual inspection of our targets using ground-based imaging to ensure they appeared isolated, thereby ensuring that our objects have extremely low values of $m_{\rm max,2}/m_{\rm max}$. These targets were drawn to qualify for both the field O star and field OB star samples from Oey et al. (2004), defined to have no other stars having $m \geq 20M_{\odot}$ and $m \geq 10M_{\odot}$ within a clustering length, respectively. Thus by definition, $m_{\rm max,2} < 10M_{\odot}$ for our sample. On the other hand, 27 of the 91 stars (30%) in the field O star sample of Oey et al. are not members of the field OB sample, implying that for these stars $m_{\rm max,2} \geq 10M_{\odot}$. The remaining 70% of isolated O stars having companions with masses below $10M_{\odot}$ can be compared to a simulated fraction of 57% in our $M_{\rm cl}^{-2}$ simulation and 64% in our N_{*}^{-2} simulation. However, the SMC field O star sample is contaminated by runaway stars which will inflate the observed fraction of O stars with $m_{\rm max,2} \leq 10M_{\odot}$.

However, we also note that the distribution of $m_{\rm max,2}/m_{\rm max}$ in the simulations does depends somewhat on the cluster population parameters and populating algorithm. For example, if we do not discard and repopulate clusters when the total cluster mass exceeds 105% of the target mass (see §2.3.2), then our test simulations show that the increased production of massive stars can affect the percentiles by up to a factor of two, so that our objects fall in the lowest 50th percentile, for the default $M_{\rm cl}$ simulation. Thus in this case, our observed clusters are nearer to the median and more well-distributed overall.

2.5 The relation between $m_{\rm max}$ and $M_{\rm cl}$

2.5.1 Observations and Simulations

In Figures 2.9 and 2.10, we compare the relationship between the cluster mass $M_{\rm cl}$ and maximum stellar mass $m_{\rm max}$. As in Figure 2.7, panel (a) includes simulated clusters with ≥ 1 O star, while panel (b) includes only simulated clusters with exactly one O star. The color coding scheme is also the same as in Figure 2.7. The solid lines show contours for the 10th, 25th, 50th, 75th, and 90th percentiles of $M_{\rm cl}$ as a function of $m_{\rm max}$ in the simulation, while the dashed line represents the mean. These percentiles are computed from a much larger set of 10^6 ($M_{\rm cl}$ simulations) or 10^7 (N_* simulations) modeled clusters, to reduce stochastic scatter. For our observations (black squares), we calculate $M_{\rm cl}$ as described in §2.3.1 (Table 2.4). The diamonds show observed Galactic clusters whose $M_{\rm cl}$ and $m_{\rm max}$ are tabulated by Weidner et al. (2010a).

Figures 2.9*a* and 2.10*a* show that the majority of the Galactic cluster sample lies above the 90th percentile in $M_{\rm cl}$ for a given $m_{\rm max}$ in both the N_* and $M_{\rm cl}$ simulations. In contrast, our observed objects all occur below the 50th percentile in both simulations and are more representative of the single O star cluster sample in Figures 2.9*b* and 2.10*b*. Indeed, Figures 2.9*b* and 2.10*b* show that the majority of the Galactic cluster sample lies outside the single O star cluster parameter space. This indicates that the Galactic cluster sample is comprised of clusters with a well-populated IMF, probably due to selection effects, since more fully populated clusters preferentially tend to be observed (Maschberger & Clarke 2008).

In Figure 2.11, we plot the mean $m_{\rm max}$ value as a function of $M_{\rm cl}$ (dashed line) for our $M_{\rm cl}^{-2}$ simulation. The solid lines now show contours for the 10th, 25th, 50th, 75th, and 90th percentiles of $m_{\rm max}$ as a function of $M_{\rm cl}$ in the simulation, again calculated from the larger sets of simulated clusters. The dashed line represents the mean. We note that in Figure 2.11*a*, the percentiles are calculated from all clusters having a given $M_{\rm cl}$, while the simulated clusters plotted here are only those which contain at least one O star. In Figure 2.11*b*, the percentiles exclude all clusters with multiple O stars, and the plotted clusters are those with a single O star.

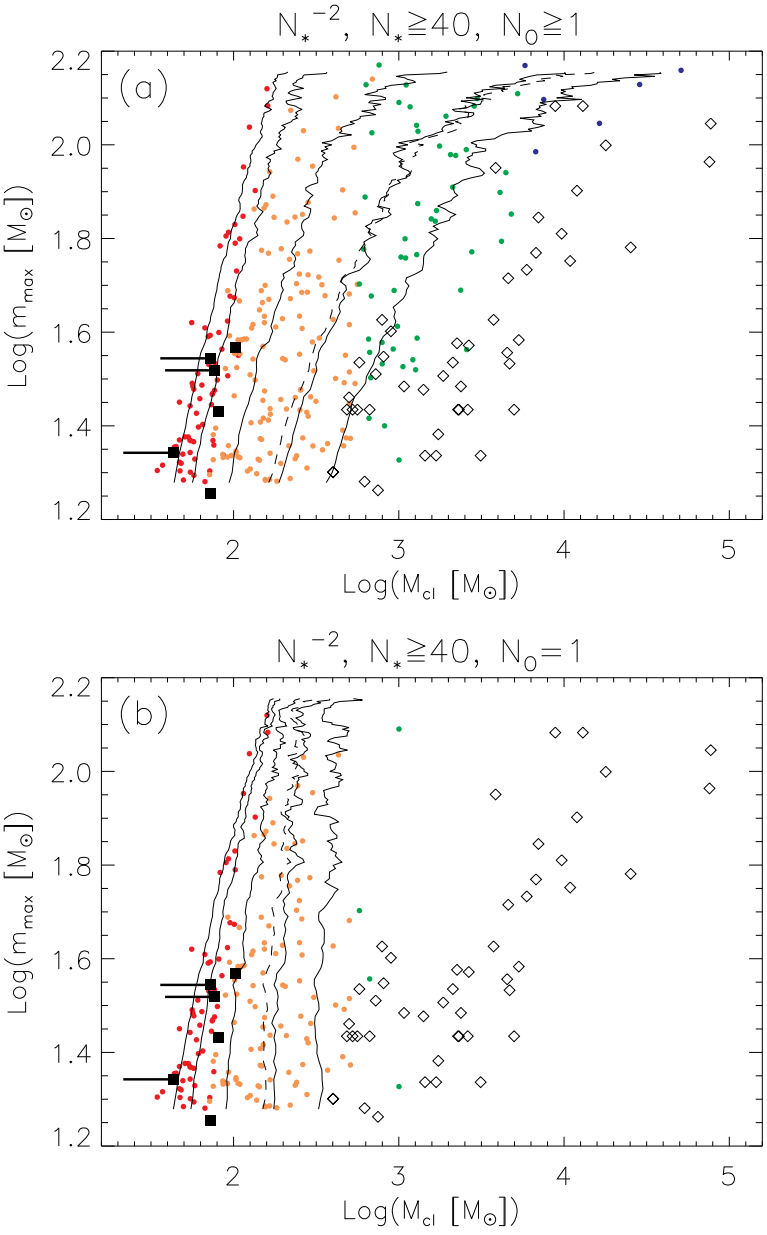

Figure 2.9. $\log(m_{\rm max})$ vs. $\log(M_{\rm cl})$ from the N_* simulations for (*a*) all clusters having at least one O star, and (*b*) all clusters having only a single O star. Colors are as in Figure 2.7, with diamonds representing Galactic clusters tabulated by Weidner et al. (2010a). The solid lines represent the 10th, 25th, 50th, 75th, and 90th percentile of $M_{\rm cl}$ as a function of $m_{\rm max}$ from the simulations. The dashed line represents the average value from the simulations.

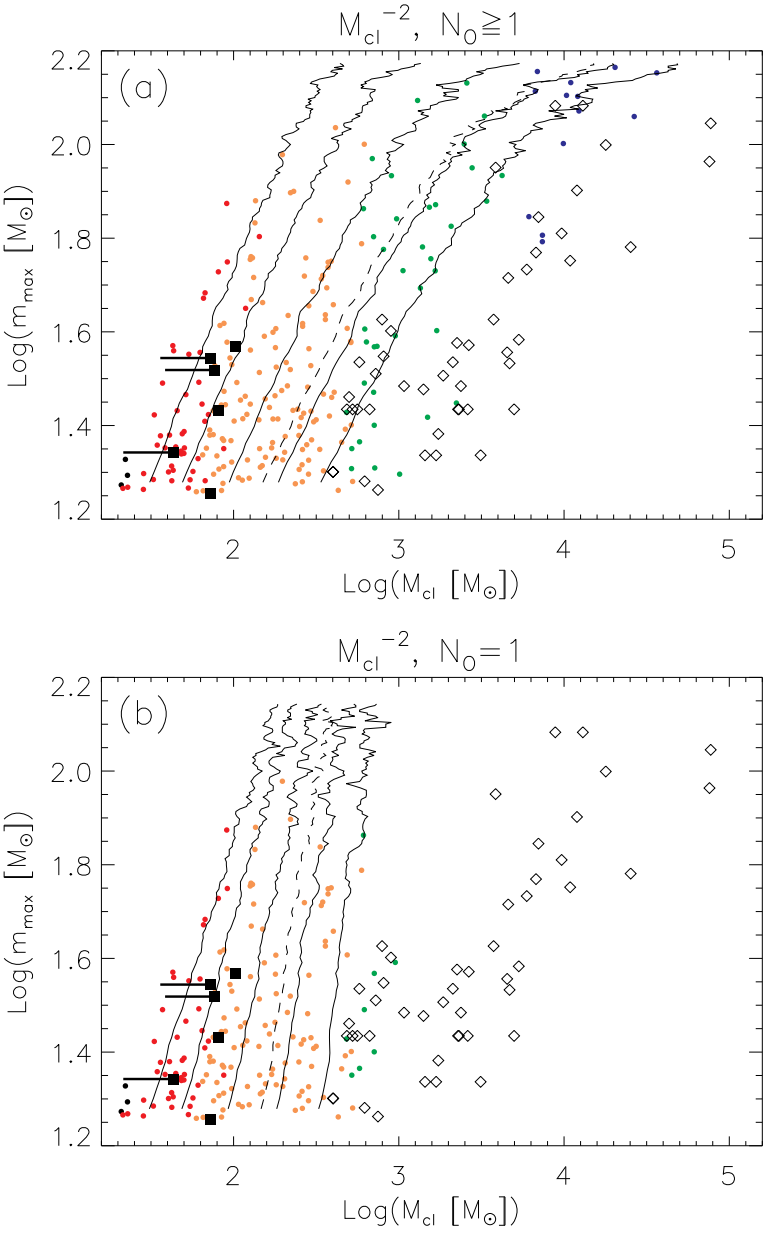

Figure 2.10. Same as Figure 2.9 but for the $M_{\rm cl}$ simulations.

Here, we see that nearly all of our observed clusters are above the 90th percentile of $m_{\rm max}$ as a function of $M_{\rm cl}$. In Figure 2.11*a*, all the Galactic clusters are below the 50th percentile, with the majority below the 10th percentile. Figure 2.11*b* again demonstrates that the Galactic O star cluster sample largely falls outside the parameter space of the single O star clusters. Comparing the percentiles plotted in Figure 2.11*b* with those in Figure 2.11*a* shows little difference for our observed $M_{\rm cl}$ values; however, as $M_{\rm cl}$ increases, the transition from single O star clusters to clusters with > 1 O star is revealed in the turnover of the percentiles in Figure 2.11*b*. This confirms that the Galactic cluster sample is comprised mainly of clusters with multiple O stars.

2.5.2 Does $M_{\rm cl}$ determine $m_{\rm max}$?

We now compare our observations with numerical simulations that are limited by a relation between the maximum stellar mass within a cluster and total cluster mass ($m_{\rm max}$-$M_{\rm cl}$). As mentioned in §2.1, various forms of this relation have been proposed, based on both theory (Bonnell et al. 2004) and observations (WK06), that invoke a physical relation between $m_{\rm max}$ and $M_{\rm cl}$. This is different from the purely statistical relation between the average $m_{\rm max}$ and $M_{\rm cl}$ (Oey & Clarke 2005). In the latter case it is simply improbable to form a massive star in a small cluster, whereas in the integrated galaxial initial mass function (IGIMF) proposed by Weidner & Kroupa (2005), the $m_{\rm max}$-$M_{\rm cl}$ relation is modeled deterministically, such that $m_{\rm max}$ never exceeds the value derived from this $m_{\rm max}$-$M_{\rm cl}$ relation. For reference, see Figure 1 of Weidner & Kroupa (2005), which plots various $m_{\rm max}$-$M_{\rm cl}$ relations from the literature.

If we adopt the mean in Figure 2.11*a* as a simple $m_{\rm max}$-$M_{\rm cl}$ relation, then all simulated clusters above the dashed line are in violation of such a relation. We note that the mean corresponds to somewhat lower-mass clusters for a given $m_{\rm max}$ than the WK06 $m_{\rm max}$-$M_{\rm cl}$ relation. Even so, our observed minimal O star groups do not fit within the framework of a steepened IGIMF as presented by Weidner & Kroupa (2005), although we note that statistical variation of the $m_{\rm max}$-$M_{\rm cl}$ relation is not included in their work.

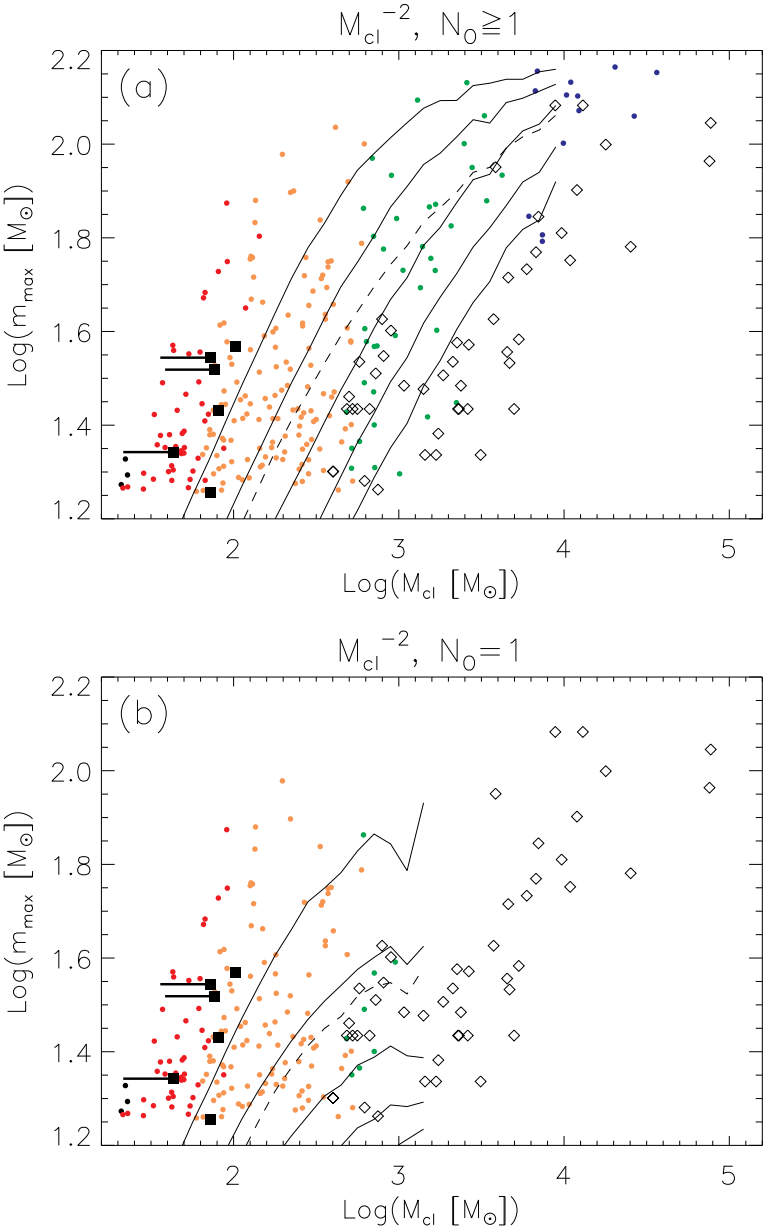

Figure 2.11. Same as Figure 2.10, except with percentile and mean lines showing $m_{\max}$ as a function of $M_{\rm cl}$.

Figure 2.12 shows $m_{\rm max,2}/m_{\rm max}$ as a function of $m_{\rm max}$ for clusters that correspond to our imposed $m_{\rm max}$-$M_{\rm cl}$ relation, which are those below the mean $m_{\rm max}$ plotted in Figure 2.11*a*. The color coding and panel samples are the same as in Figure 2.8. Figure 2.12*a* illustrates that all simulated O star clusters now exhibit $m_{\rm max,2}/m_{\rm max} \geq 0.2$. With this imposed $m_{\rm max}$-$M_{\rm cl}$ relation, our observations appear to fall completely outside the parameter space of the simulations in both Figure 2.12*a* and 2.12*b*, given the number of clusters corresponding to the SMC cluster population. This form of the deterministic $m_{\rm max}$-$M_{\rm cl}$ relation is therefore poorly supported by our observations of minimal O star groups.

One possible interpretation of these results is that our observed objects are remnants of clusters affected by "infant weight loss" (e.g., Bastian & Goodwin, 2006). However, even if the objects have been reduced by a factor of a few in $M_{\rm cl}$ or N_*, they would still be discrepant from the Galactic cluster sample of Weidner et al. (2010a). Recent simulations have shown that cluster mass segregation can occur on timescales of $\sim$1 Myr for the most massive cluster stars (Allison et al. 2009). Massive stars segregated to the cluster core are unlikely to be evaporated by "infant weight loss", and so clusters are likely to retain the two most massive stars. Therefore, the observed $m_{\rm max,2}/m_{\rm max}$ values are unlikely to be affected by dynamical evaporation. Moreover, "infant weight loss" is associated with the rapid removal of gas, which, however, is still present in the majority of our objects (§2.2.3). Furthermore, N-body simulations of sparse, young clusters by Weidner et al. (2010b) show that $< 15\%$ of the cluster's mass is removed within 5 Myr, suggesting that significant mass loss is relatively unimportant in such objects.

Our results are similar to those found by Maschberger & Clarke (2008), who examined a sample of clusters from the literature using studies that focused on low N_* clustering around high-mass stars. The observations of isolated Herbig Ae/Be stars by Testi et al. (1997, 1999), as well as our observations of isolated OB stars, show that massive stars may form in even the most sparse environments. As we showed above, these observations are not consistent with a strictly-defined, deterministic $m_{\rm max}$-$M_{\rm cl}$ relation. At the very least, the minimal OB groups, along with clusters compiled

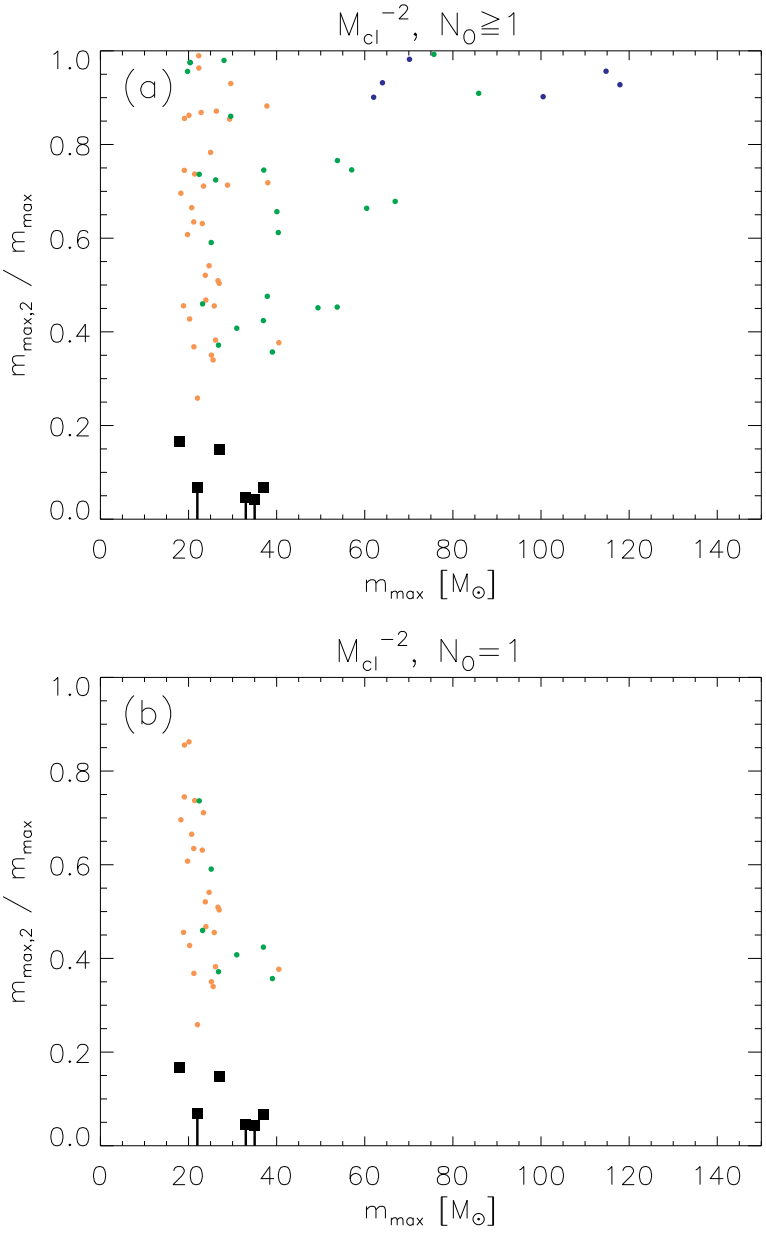

Figure 2.12. Same as Figure 2.8, but applying a fixed $m_{\rm max}$ - $M_{\rm cl}$ relation.

by Weidner et al. (2010a), imply huge deviation from a direct $m_{\rm max}$-$M_{\rm cl}$ relation (Figure 2.11). While a steepened IGIMF will occur even without a $m_{\rm max}$-$M_{\rm cl}$ relation, this result has problematic implications for the magnitude of proposed steepening for the IGIMF in aggregate galactic stellar populations (Weidner & Kroupa 2005). In addition, the competitive accretion theory of star formation is also linked to an $m_{\rm max}$-$M_{\rm cl}$ relation (Bonnell et al. 2004), although we note that Maschberger et al. (2010) find that competitive accretion simulations are nevertheless able to produce massive field stars of at least $9M_{\odot}$. On the other hand, simulations of star formation based on core accretion (e.g., Krumholz et al. 2010) show that under specific cloud conditions, radiative heating can prevent fragmentation, perhaps more directly forming minimal O star groups similar to those observed in this paper.

2.6 Conclusions

We carried out a SNAP program with *HST's* Advanced Camera for Surveys that yielded high resolution observations of eight field OB stars in the SMC. These stars range in spectral type from O7 to B0.5, and in mass from $18M_{\odot}$ to $37M_{\odot}$. Radial velocities for two stars (AzV 223 and smc16) show them to be runaways, and we may expect one or two more to be transverse runaways. There is no evidence of clustering down to a $1.5M_{\odot}$ detection limit in three of the six non-runaway cases. The non-runaway, isolated stars (AzV 58, AzV 186, and AzV 226) remain candidates for isolated OB star formation. Two of these isolated OB stars reside within HII regions, indicating that these stars may still be located in the region of their formation, and strengthening the possibility that these O stars have formed alone. For the other three non-runaway OB stars (AzV 67, AzV 106, and AzV 302), we detect an associated population of stars using a stellar density analysis and a separate friends-of-friends algorithm. After accounting for field contamination, we find eight to ten stars associated with each OB star, ranging in mass from our lower detection limit of $1M_{\odot}$ to $4M_{\odot}$.

The three observations that do show evidence of clustering exhibit a flat IMF with slope of $\Gamma = 0.1 \pm 1.0$ to -0.2 ± 0.9 when combining their populations, although due

to the small sample size, the IMF may be consistent with a Salpeter IMF, which has Γ = -1.35. The flat IMF is due to a lack of low-mass companions that ordinarily are expected to form along with these O stars.

Assuming that each of our non-runaway stars is still in the location where it formed, we infer cluster membership of $N_* = 19 - 171$ based upon the companion population $\geq 1.5 M_\odot$, integrated over the full stellar mass range for our Kroupa IMF of $0.08 M_\odot - 150 M_\odot$. Given their inferred N_*, we calculate that a small fraction, only 0.01–0.2, of clusters will form a star with mass $m \geq m_{\rm max}$ observed.

We have conducted Monte Carlo simulations to explore where our observations fall within the cluster parameter space of typical star formation, assuming a Kroupa IMF and either a clustering law based on N_* or cluster mass function based on $M_{\rm cl}$. The power law slopes and lower limits of $M_{\rm cl}$ and N_* for these simulations were constrained using observations of massive star clustering in the SMC by Oey et al. (2004) and the fraction of isolated Galactic O stars by de Wit et al. (2005). Together, these observational constraints resulted in a –2 power law slope with lower limits of $N_{*,\rm lo} = 40$ or $M_{\rm cl,lo} = 20 M_\odot$ as the best fit models, which we adopted as the default simulations for this study. These default N_* and $M_{\rm cl}$ models match equally well with the observations, thus neither one is established as a more suitable metric for modeling cluster distribution.

We find that observed mass ratios of the two highest-mass stars are below the 25th percentile of single O star clusters generated by the default simulations. This result is due to choosing targets which appeared isolated in ground-based imaging. Our observations also lie below the 50th percentile when comparing total cluster mass (either $M_{\rm cl}$ or N_*) as a function of $m_{\rm max}$, whereas a sample of Galactic clusters from Weidner et al. (2010a) are nearly all above the 90th percentile. These numbers suggest that our observations are more typical examples of O star clusters than the Galactic cluster sample, which contains clusters with well-populated IMFs.

We show evidence that our observed minimal O star groups are inconsistent with a deterministic $m_{\rm max}$-$M_{\rm cl}$ relation. By extension, our observations are also inconsistent with the $m_{\rm max}$-$M_{\rm cl}$ relation proposed for the IGIMF effect (Weidner & Kroupa 2005)

and the relation that $M_{\rm cl} \propto m_{\rm max}^{1.5}$ (Bonnell et al. 2004), predicted by the competitive accretion model of massive star formation. We argue that in most cases, an observed $m_{\rm max}$-$M_{\rm cl}$ relation is simply a product of the stochastic, probabilistic nature of a universal IMF, rather than an IMF with a variable upper limit corresponding to cluster mass. We conclude that our observations of minimal O star groups are consistent with a universal stellar mass function, including a constant stellar upper-mass limit, without the need to invoke a $m_{\rm max}$-$M_{\rm cl}$ relation.

CHAPTER 3

The Initial Mass Function of Field OB Stars in the Small Magellanic Cloud

3.1 Introduction

In many ways, the mass of a star is its most important attribute. A star's mass constrains not just its observable properties and future evolution, but also provides an observational link to the local conditions under which it formed. Similarly, the initial mass function (IMF) is a fundamental parameter of a stellar population and provides a direct probe of the star formation process.

The form of the high mass tail of the stellar initial mass function (IMF) was first discovered by Salpeter (1955), who found it could be well-described by a simple power law of the form $n(m)\ dm \propto m^{-\gamma} dm$ where n is the number of stars, m is stellar mass, and $\gamma = 2.35$. This original measurement has proven to be robust for stars $\gtrsim 1 M_{\odot}$, with stellar populations from small OB associations to young, massive clusters all exhibiting this canonical Salpeter IMF (Kroupa 2001 and references therein). These widespread similarities in the top end of the IMF from such disparate populations may imply that the IMF is a universal property of star formation, regardless of environment (e.g., Elmegreen 2000). However, the universality of the IMF is still an important open question (see Bastian et al. 2010).

Alongside the power law slope of the IMF, the stellar upper mass limit, $m_{\rm up}$, is also a critical component of a stellar population. Studies of well-populated clusters indicate $m_{\rm up} \sim 150 M_{\odot}$ (e.g., Oey & Clarke 2005), although masses up to twice as large are reported (e.g., Crowther et al. 2010). However, $m_{\rm up}$ for small-scale, isolated star formation is poorly constrained.

The field star population is an ideal target for an investigation into the consistency of the Salpeter IMF slope and $m_{\rm up}$ for distributed, sparse star formation. Furthermore, the ability of massive stars to form in isolation is a distinguishing test between two popular theories of massive star formation, monolithic collapse (e.g., Shu et al. 1987) and competitive accretion (e.g., Zinnecker 1982). In the monolithic collapse model, molecular clouds fragment unevenly into clumps that will each form a single star, which will accrete material solely from its own fragment of the cloud. In this model, the mass of the fragment determines the available mass to form the star, so massive stars will form from massive fragments. In contrast, the competitive accretion model predicts that molecular cloud fragments are not limited to their own gas mass, but rather accrete from a shared reservoir of gas in the molecular cloud. In this scenario, high mass stars preferentially form in the dense centers of molecular clouds, where more gas available for accretion exists. From these two models, only the former is compatible with field massive star formation, although the specific mechanism that would allow a small molecular cloud to avoid fragmentation altogether is unclear. 3-D hydrodynamic simulations by Krumholz et al. (2009) reveal a scenario where a high-mass star can form in isolation or alongside a few low mass stars. In contrast, simulations of competitive accretion indicate a specific correlation between cluster mass ($M_{\rm cl}$) and the most massive star a cluster will form ($m_{\rm max}$), given by $M_{\rm cl} \propto m_{\rm max}^{1.5}$ (Bonnell et al. 2004). Thus, according to the competitive accretion scenario, massive stars are incapable of forming in isolation.

The concept of a $m_{\rm max}$-$M_{\rm cl}$ relation is also advocated by Weidner & Kroupa (2006), who use analytical models and an aggregation of Galactic cluster data to support a deterministic $m_{\rm max}$-$M_{\rm cl}$ relationship, similar to that of competitive accretion. Using an expanded Galactic cluster dataset, Weidner et al. (2010) argue that it is statistically improbable these clusters were randomly populated from the same universal stellar IMF and that a clear relationship between $m_{\rm max}$ and $M_{\rm cl}$ exists. One of the primary consequences of a deterministic $m_{\rm max}$-$M_{\rm cl}$ relationship is that the integrated galaxial initial mass function (IGIMF) would necessarily be steeper than the canonical Salpeter IMF (Weidner & Kroupa 2005), since the most massive stars are restricted

to forming only in the most massive of clusters. Similarly, the formation of massive stars in isolation appears contradictory to this model.

In situ formation is not the only explanation for isolated massive stars. There are a number of methods by which stars formed in clusters may appear in isolation. Runaway stars, in particular, are a well-established component of the field massive star population. These runaways are stars formed in the dense cores of clusters, which are ejected from their birth cluster either dynamically (Poveda et al. 1967) or by receiving a kick from a supernova explosion (Blaauw 1961). Estimates vary greatly on their fractional contribution to the field population, with observed values between 10% (Blaauw, 1961) and 50% (de Wit et al. 2005). While these works identify runaways using their high peculiar space velocities (> 30 km/s), the existence of slow runaways (Banerjee et al. 2012) or two-step ejections that reduce space velocities (Pflamm-Altenburg & Kroupa 2010) may result in such runaway fractions being underestimated. Gvaramadze et al. (2012) suggests that the runaway fraction may be as high as 100%, considering the observational difficulties of identifying low velocity runaways. Another potential origin of field massive stars are clusters that quickly expel their gas, which may cause rapid dissociation of the cluster, "infant mortality" (e.g., de Grijs & Goodwin 2008) or a large fraction of it, "infant weight loss" (e.g., Bastian & Goodwin, 2006). Finally, in some cases, sparse clusters may simply exist undetected around field massive stars (e.g., Lamb et al. 2010). As a whole, the field population may be a combination of some or all of these separate stellar populations.

The heterogeneous nature of the field population significantly complicates its mass function. Each component of the field may have a different impact on the stellar mass function. The frequency of runaways, for example, correlates with spectral type (e.g., Blaauw 1961). Stone (1991) found runaway fractions of 30-40% and 5-10% for O and early B stars, respectively. Thus, the runaway population would tend to flatten the IMF of the field. In contrast, competitive accretion theory and the $m_{\rm max}$-$M_{\rm cl}$ relation suggest that sparse massive star formation or in situ field formation may not sample the top end of the IMF, which would result in steepening the field IMF in a manner

similar to the proposed steepening of the IGIMF. However, the mass function of field stars formed in situ is an unknown quantity and may be a product of a different mode of star formation, distinct from clustered star formation.

Studies of field massive star populations have yet to converge on a value for its stellar mass function. An analysis by van den Bergh (2004) directly compares the spectral types of clustered stars versus field stars from a survey of Galactic O stars (Maíz-Apellániz et al. 2004). He finds that field OB stars are skewed towards later spectral types than their clustered counterparts, which suggests that the field population is either less massive or older than the cluster population. Massey et al. (1995) and Massey (2002) use a combination of spectroscopy and photometry to measure the high mass stellar IMF of clusters, associations and a few sample field regions in the Small and Large Magellanic Clouds. While the clusters and associations exhibit the canonical Salpeter IMF slope, $\Gamma = \gamma - 1 = 1.35$, the field IMF is significantly steeper, with a slope of $\Gamma \sim 4$ above their completeness limit of $25 M_{\odot}$. However, Selman et al. (2011) show that the field population around the 30 Dor region of the Large Magellanic Cloud is consistent with a Salpeter IMF. Ubeda et al. (2007) derive an IMF slope of $\Gamma = 1.8$ for NGC 4214 using *HST* WFPC2 and STIS photometry. Resolving these discrepancies requires a robust determination of the field massive star IMF using a reliable estimator for mass, such as spectroscopy.

The field studies discussed above fall into two general categories: a small-scale survey using reliable, spectroscopic mass estimates, or a large-scale photometric survey that yields less reliable masses. Spectroscopic studies in particular have significant completeness issues and are limited to the nearby Galactic field or sub-samples of nearby galaxies. These limitations lead to an incomplete picture of the field massive star population. In this work, we present the first spatially complete, spectroscopic survey of an entire galaxy's field massive star population. We target the Small Magellanic Cloud (SMC) in our Runaways and Isolated O Type Star Spectroscopic Survey of the SMC (RIOTS4). With RIOTS4 spectra, we obtain accurate masses for the entire population of field massive stars across the full spatial extent of the SMC. This unprecedented data set will yield a definitive mass function for field massive stars in

the SMC, including the slope and upper mass limit. We discuss the importance of these results in the context of massive star formation models and highlight differences between the field and clustered populations of massive stars.

3.2 RIOTS4

Here, we present an abbreviated description of the RIOTS4 survey. A complete description can be found in Lamb et al. (in prep). RIOTS4 targets the complete sample of 374 SMC field OB stars, as identified in Oey et al. (2004). Selection of these targets is a two step process. First, Oey et al. (2004) identify massive stars in the SMC using two photometric selection criteria, $B \leq 15.21$ and $Q_{UBR} \leq -0.84$, where Q_{UBR} is the reddening free parameter given by

$$Q_{UBR} = (m_U - m_R) - \frac{A_U - A_R}{A_B - A_R}(m_B - m_R) = (m_U - m_R) - 1.396(m_B - m_R) \ . \quad (3.1)$$

Photometry from Massey (2002) is used for this selection. Second, the field stars are selected by running a friend-of-friends algorithm (Battinelli 1991) on the massive star sample. This algorithm identifies stellar clustering by setting a physical clustering length such that the number of clusters is maximized. Thus, our RIOTS4 targets are those OB stars that are at least one clustering length (28 pc) removed from any other OB stars.

The primary instrument for RIOTS4 is the Inamori-Magellan Areal Camera and Spectrograph (IMACS) on the Magellan Baade telescope at the Las Campanas Observatory. One of the primary benefits of IMACS is the capability of multi-object observations using slitmasks. We observe a total of 328 objects in 49 slitmasks in the f/4 observing mode. The multi-object observing setup is designed to maximize spectral resolution with a 1200 lines/mm grating and either a 0.7" or 1" slit width, resulting in spectral resolutions of R $\sim$ 3700 and R $\sim$ 2600, respectively. Wavelength coverage varies between spectra, but every spectrum includes coverage from 4000-4700 $\AA$. The exposure time for each multi-object observation is one hour, split into three 20 minute exposures. We conducted all multi-object observations between

September 2006 and December 2010.

We were unable to fit all stars onto multi-slit masks, due to the density of targets being too high to fit all the objects onto the mask or too low to warrant the use of multi-object slitmasks. In these cases, we instead observe targets using IMACS long slit observations, or with the Magellan Inamori Kyocera Echelle (MIKE) single object spectrograph on the Magellan Clay telescope. With IMACS, we observe 27 stars with a 300 l/mm grism in f/2 mode with 0.5" - 0.7" slit widths, which yield spectral resolutions of R $\sim$ 1000 - 1300. As before, these observations are three 20 minute exposures. With MIKE, we observe 48 stars with a 1" slit width, which yields R $\sim$ 28000. For these observations, exposure times range from 15 - 30 minutes depending on the brightness of the target and are designed to achieve a S/N $>$ 30. We performed these observations between November 2010 and October 2011.

To reduce the multi-object spectra, we use the Carnegie Observatories System for MultiObject Spectroscopy (COSMOS) data reduction package[1]. COSMOS is specifically designed to reduce and extract IMACS spectra spread across eight CCD chips. We follow the standard COSMOS cookbook to perform bias-subtraction, flat-fielding, wavelength calibration and extraction of 2-D spectra. With the 2-D spectra output from COSMOS, we use the apextract package in IRAF[2] to find, trace, and extract stellar apertures, which yields 1-D spectra. We reduce MIKE and IMACS long slit spectra with standard IRAF procedures and use the apextract package to generate 1-D spectra. With 1-D spectra in hand, we rectify them using the continuum procedure and eliminate remaining cosmic rays or bad pixel values with the lineclean procedure, which are both part of the onedspec package in IRAF.

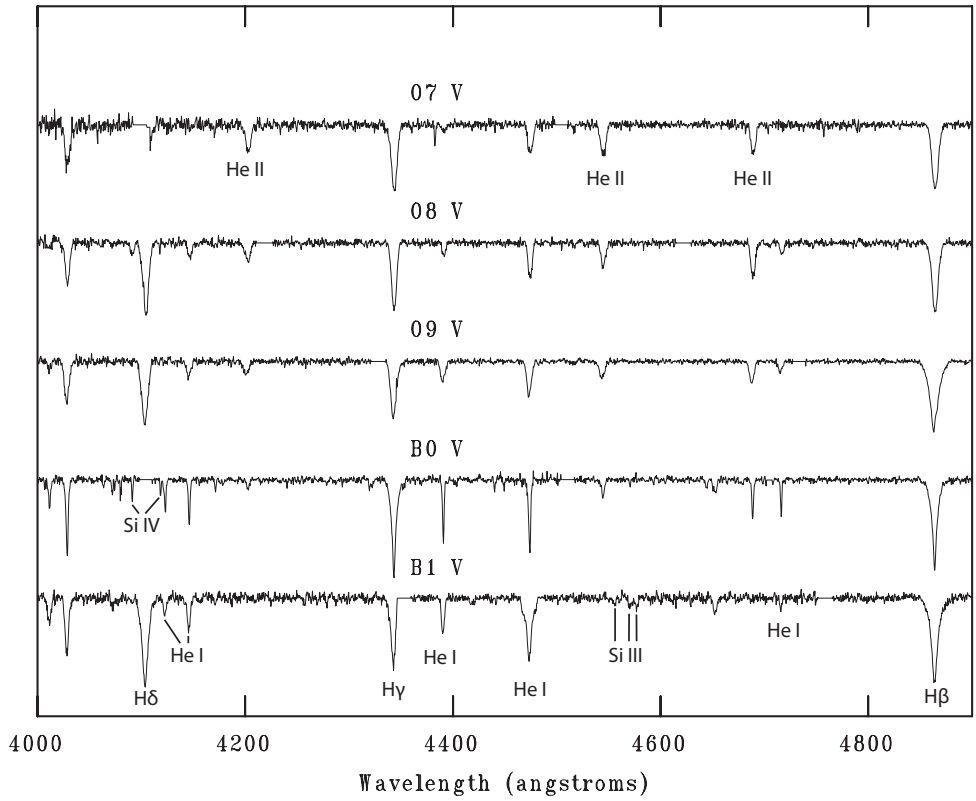

Figure 3.1. A sequence of spectral types from 07 V to B1 V from the RIOTS4 survey. We label the major spectral features in the range from $4000 - 4900\mathring{A}$. The ratio of He II λ4542 to He I λ4471 is a primary spectral type diagnostic for O stars. Notice how this ratio decreases towards later spectral types, until the disappearance of He II at B1 V.

3.3 Spectral Catalog

The key observational result of the RIOTS4 survey is the distribution of stellar spectral types. For field massive stars, the number of stars and completeness of the sample are both unprecedented in spectroscopic studies. We obtain spectral types for stars in the RIOTS4 survey using a qualitative comparison with the spectral atlas of Walborn & Fitzpatrick (1990), with additional reference to Lennon (1997), Walborn et al. (2000), Walborn et al. (1995) and Walborn (2009). J. B. L., M. S. O., and A. S. G. individually assign spectral types for each star. We re-examine any discrepancies until a consensus is reached. We polish our catalog further by plotting spectra sequentially according to spectral type in an iterative process to more clearly define the boundaries between spectral types. We consider the majority of our spectral types accurate to within half a type; thus, a star cataloged as O9 may range from O8.5 - O9.5. For stars with more uncertainty, we list a range of spectral types in our catalog. In Figure 3.1, we plot a sequence of RIOTS4 spectra, which cover spectral types from O7 V to B1 V. The primary diagnostic lines used for spectral typing are the ratio of He II λ4542 to He I λ4471 for O stars (see Figure 3.1) and the ratio of Si IV λ4088 to Si III λ4555 for B stars. Luminosity classes are determined using an iterative approach, where spectral diagnostics are the primary criterion and photometric magnitudes are a secondary criterion. Primary spectral diagnostics for luminosity class include emission of N II $\lambda\lambda$4634-4640-4042 and absorption/emission of He II λ4686 for stars earlier than O8, the ratio of Si IV λ4088 to He I λ4026 for late O stars, and the ratio of Si III λ4555 to He I λ4471 for B stars. Due to the lower metallicity of the SMC, many stars in our sample exhibit weak metal lines in comparison to the Walborn & Fitzpatrick (1990) catalog. Thus, for evolved stars, we also rely heavily on the classification criterion established by Lennon (1997) for SMC supergiants. Finally, photometric magnitudes (Massey 2002) do provide an additional

[1]COSMOS was written by A. Oemler, K. Clardy, D. Kelson, G. Walth, and E. Villanueva. See http://code.obs.carnegiescience.edu/cosmos.

[2]IRAF is distributed by the National Optical Astronomy Observatory, which is operated by the Association of Universities for Research in Astronomy (AURA), Inc., under cooperative agreement with the National Science Foundation (NSF).

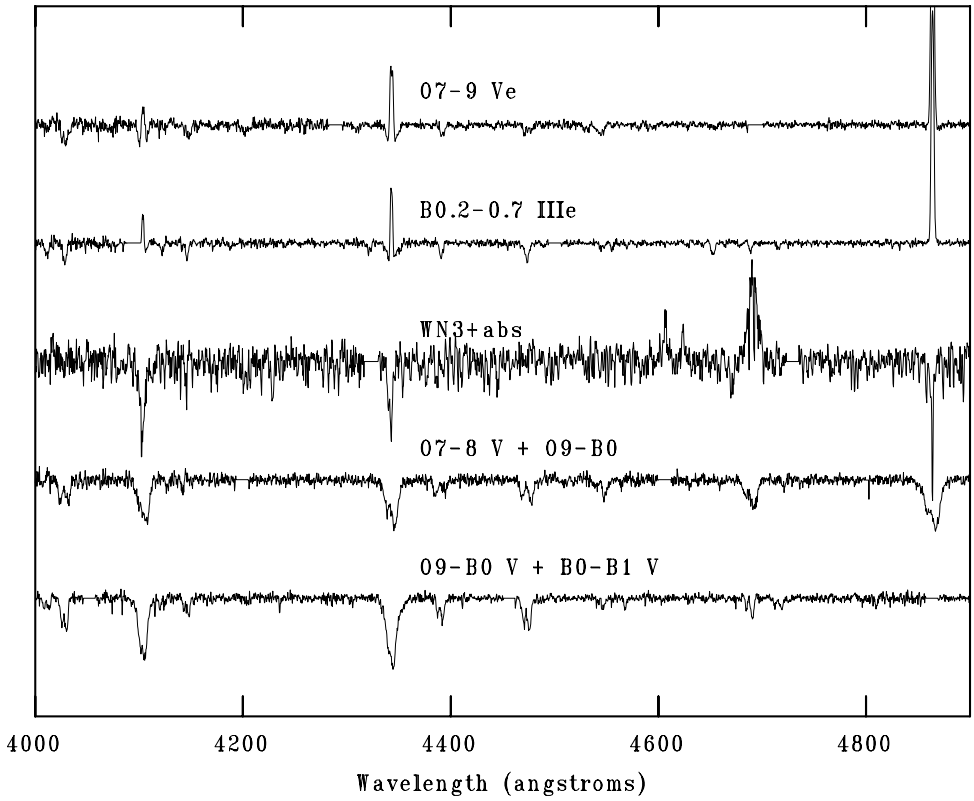

Figure 3.2. A collection of binary and emission line stars from the RIOTS4 survey. From top to bottom, these are examples of an Oe star, a Be star, a Wolf-Rayet star, an O+O binary system, and an O+B binary system. The spectral type ranges for the Oe and Be star include a direct measurement based on line ratios and an estimate of the equivalent photospheric spectral type the star would have if infilling of He I did not occur.

check on the luminosity class. However, multiplicity cannot be ruled out and should be expected at a significant level. As part of the RIOTS4 survey, we investigate the binary fraction of SMC field massive stars by taking $\sim$10 epochs of observations for 30 stars our sample. Preliminary results from these observations indicate a binary fraction $\gtrsim 50\%$ (Lamb et al. in prep), which is similar to that found in open clusters (e.g Sana et al. 2008, 2009, 2011)

Two populations add considerable difficulties to the RIOTS4 spectral catalog: binaries and emission line stars (see Figure 3.2). We identify binaries either through double-peaked absorption lines, or the presence of two strong spectral lines that cannot originate from a single star, such as He II λ4542 and Si III λ4555. To obtain

spectral types for the binary population, we create a sequence of model binary star spectra, ordered by spectral type of the primary and secondary objects. To avoid issues with metallicity, we create these model binaries directly from the RIOTS4 data. First, we median combine RIOTS4 spectra with identical spectral types to obtain a template spectrum for that type. Then, we combine two template spectra, appropriately accounting for luminosity, to generate a model binary star. In this manner, we find that we can identify the primary object to within one spectral type in most cases. However, the secondary star is rarely well constrained, especially in the case of single-lined binaries. The spectral types of B star companions to a primary O stars, which represent the majority of our binary systems, are particularly difficult to determine. These difficulties are due in large part to the relatively weak metal lines that distinguish B star spectral types, and the luminosity difference between O and B stars. We also investigate the consequences of a large population of undetected binaries in §3.6.1.

The second troublesome population are emission line (Wolf-Rayet and Oe/Be) stars. Our survey includes a pair of well studied Wolf-Rayet (WR) stars, for which we adopt their physical parameters from Massey et al. (2002). However, for Oe/Be stars, their emission lines arise from hot circumstellar material around the star. In the case of classical Oe/Be stars, this material exists in a 'decretion disk' caused by the rapid rotation of the star (e.g., Porter & Rivinius 2003). This population is expected, since classical Oe/Be stars are more common in the SMC than in the Galaxy or the LMC (e.g., Bonanos, 2010). Classical Oe/Be stars represent a significant fraction of the RIOTS4 sample, with $< 50\%$ of B stars and $< 20\%$ of O stars exhibiting emission in one or more Balmer lines. However, these fractions are artificially high due to the selection criteria for RIOTS4. Classical Oe/Be stars exhibit strong H-α emission, which brightens the R magnitudes of these stars. In turn, this effect lowers the value of Q_{UBR} in these objects, which causes them to be preferentially included in the RIOTS4 survey due to our $Q_{UBR} \leq -0.84$ selection criterion. Thus, the completeness of Be stars extends to slightly later spectral types than for normal B stars in the RIOTS4 survey. For measuring stellar masses, the primary issue with

Oe/Be star spectra is the presence of weak or filled-in absorption lines. Spectral types are significantly impacted when the important diagnostic lines listed above appear filled-in or non-existent. In the particular case of Oe stars, infilling does not affect the He II lines but may impact He I lines, which may bias these stars to earlier spectral types (Negueruela et al. 2004). To deal with this issue, we adopt a large spectral type range for Oe stars that show evidence of infilling in He I lines. The earliest type in this range is obtained from the ratio of He II to He I line strengths, as in non-emission line stars. The later type in this range is estimated by the relative strengths of the different He II lines and indicates the spectral type the star would have without infilling. This equivalent photospheric spectral type allows us to obtain a better estimate of $T_{\rm eff}$. Oe/Be stars with smaller ranges indicate objects where the important diagnostic lines appear with smooth, Gaussian profiles. Ultimately, we adopt the median spectral type from these ranges in our derivation of their stellar parameters, but adopting either the early or later types in these ranges does not significantly impact our results (see §3.5.1).

There is some overlap of our survey with other spectroscopic studies of the SMC; however, our typical S/N $\sim$ 75 and resolution R $\sim$ 3000 compare favorably to these studies. A number of our targets were observed by Massey et al. (1995) with similar S/N $\sim$ 75 but lower resolution (R $\sim$ 1500). We find good agreement with our spectral types. When discrepancies do arise, they are always within half a spectral type or two luminosity classes. Another study that significant overlaps with RIOTS4 is the 2dF survey of the SMC (Evans et al. 2004; Evans & Howarth 2008). Their spectroscopic data is slightly lower quality than RIOTS4, with average S/N $\sim$ 45 and R $\sim$ 1600. Our agreement with 2dF is not as good as with Massey et al. (1995), with the majority of discrepancies arising with luminosity class. In general, we agree with 2dF spectra to within one spectral type and two luminosity classes. Evans et al. (2004) classify a large fraction of the overlapping sample of stars as giants, many of which we classify as dwarfs. However, due to the poor quality of their spectra, they rely on a combination of the equivalent width of H-γ and stellar magnitude for their luminosity classifications. Thus, their ad hoc methodology may explain this apparent

discrepancy in luminosity classifications.

3.4 HR Diagram and Stellar Masses

We use our spectral types and photometry from Massey (2002) to derive the physical properties of 284 individual stars in RIOTS4. In Table 3.1, we list the spectral types and physical properties for all stars in the RIOTS4 survey that contribute to our measurement of the IMF ($> 20M_{\odot}$). We list the ID number, B magnitude, and V magnitude from Massey (2002) in columns 1, 2, and 3, respectively. Photometric errors are typically ~ 0.03 mag in B and ~ 0.02 mag in V (Massey 2002). Column 4 lists Q_{UBR} calculated from the Massey (2002) photometry. We list bolometric magnitude, $M_{\rm Bol}$, in column 5, which is calculated using the extinction, A_V, and stellar effective temperature, $T_{\rm eff}$ (Section 3.4, given in columns 6 and 7, respectively). Finally, we list the estimated mass and observed spectral type from RIOTS4 in columns 8 and 9, respectively. Stars with uncertain spectral types are given a range, with their adopted $T_{\rm eff}$ coming from the median spectral type within that range. To obtain stellar effective temperature, $T_{\rm eff}$, we use two different calibrations, one for O stars and one for B stars. Due to the lower metallicity in the SMC (e.g., Hunter et al. 2007), the $T_{\rm eff}$ of O stars is systematically higher than in the Galaxy for stars of the same spectral type (Massey et al. 2005). For O stars, we therefore convert spectral types to $T_{\rm eff}$ using the calibration in Massey et al. (2005) for the SMC. For B stars, we use conversions to $T_{\rm eff}$ from Crowther et al. (1997). These calibrations overlap smoothly at a spectral type of B0. Although Crowther et al. (1997) use a sample of Galactic stars for their calibration, Massey et al. (2005) demonstrate that $T_{\rm eff}$ for SMC and Galactic stars is equal for stars B0 and later. We calculate bolometric magnitudes using $M_{\rm Bol} = V$ - DM - A_V + BC, where DM is the distance modulus, A_V is the extinction, and BC is the bolometric correction. We adopt $DM = 18.9$ (Harries et al. 2003) and $BC = 27.99 - 6.9 \log T_{\rm eff}$ (Massey et al. 2005). A_V is found using the SMC extinction maps from the Magellanic Clouds Photometric Survey (MCPS; Zaritsky et al. 2002).

With $T_{\rm eff}$ and $M_{\rm Bol}$ computed, we construct a Hertzprung-Russell diagram of the

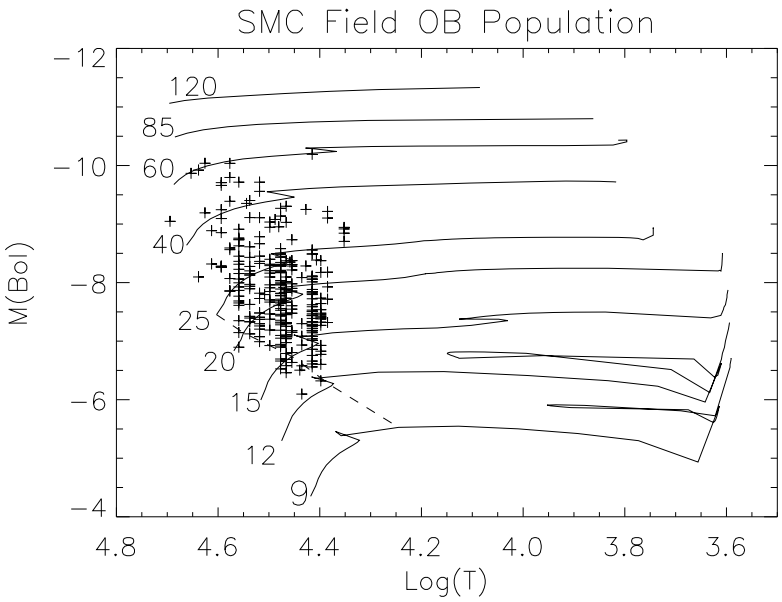

Figure 3.3. An H-R diagram of our field stars with physical parameters $T_{\rm eff}$ and $M_{\rm Bol}$ derived from spectral types and Massey (2002) photometry. The evolutionary tracks plotted here are from Charbonnel et al. (1993) at SMC metallicity and are labelled corresponding to the stellar mass of the evolutionary track in $M_{\odot}$. The dashed line indicates the completeness limit of RIOTS4.

SMC field massive star population (Figure 3.3). Stars from the RIOTS4 survey are plotted as plus signs, while the lines represent Geneva stellar evolutionary tracks at a metallicity of Z=0.004, consistent with the SMC (Charbonnel et al. 1993). These tracks are labelled by stellar mass in $M_{\odot}$. We plot the completeness limit of RIOTS4 as a dashed line. Thus, RIOTS4 is complete to 20 $M_{\odot}$ along most of the main sequence and 25 $M_{\odot}$ along the ZAMS. Although relatively few stars are observed below the completeness limit, this is due to the RIOTS4 selection criteria, rather than an indication of the completeness of Massey (2002) photometry. Due to these completeness issues, we will limit our measurement of the field IMF in Section 3.5.1 to stars > 20 $M_{\odot}$. One striking feature of this HR diagram is the shift of the observed main sequence from the main sequence of the Geneva models. There is a distinct lack of stars observed along the modeled ZAMS and likewise, a significant population of objects extending past the main sequence turn-off of the models. A similar distribution is seen in a sample of SMC field stars from Massey (2002) (his Figure 10) and in the SMC cluster NGC 346 from Massey et al. (1995) (their figure

8). Thus, it is unclear if this offset is a real property of the SMC, or due to some systematic issue with either the Geneva models or the calibration and calculation of $T_{\rm eff}$ and $M_{\rm Bol}$. One possible explanation is that the Geneva models plotted here are non-rotating models. Models with rotation at SMC metallicity shift the main sequence to cooler $T_{\rm eff}$, but the magnitude of the effect is only ~ 0.04 dex for stars rotating at 300 km s^{-1} (Maeder & Meynet 2001). Thus, rotation alone cannot explain the discrepancy shown in Figure 3.3. Therefore, it appears that SMC field massive stars are systematically cooler or more evolved than expected from the Geneva stellar evolutionary models.

Despite the above issues with the Geneva models, the nearly horizontal evolution of stars off the main sequence in $M_{\rm Bol}$ vs. $T_{\rm eff}$ helps to mitigate their impact on stellar mass estimates. Thus, with these Geneva models and the derived stellar parameters of $T_{\rm eff}$ and $M_{\rm Bol}$, we proceed to estimate the stellar mass of each individual star. To accomplish this, we linearly interpolate between the Geneva model isochrones (Charbonnel et al. 1993) to match the stellar parameters. The primary source of error in our mass estimates is due to uncertainty in our spectral types. Our typical uncertainty of half a type corresponds to $\sim$1500 K or 1-5 $M_{\odot}$, depending on mass of the star. Stars with higher masses will typically have larger errors due to the spacing of tracks in the $M_{\rm Bol}$ vs. $T_{\rm eff}$ parameter space. Another potential source of error is the discrepancy between the models and observations discussed above. However, since this appears to be a systematic effect, its impact on the shape of the IMF should be small.

3.5 The Field Massive Star IMF

3.5.1 The Field IMF above $20M_{\odot}$

We proceed with a derivation of the stellar mass function of the field following the method of Koen (2006). Since the field population is not coeval, we are actually measuring its present day mass function (PDMF), rather than its IMF. Just as with

the IMF, the PDMF can be described by a power law of the form

$$f(m) = \alpha m^{-(\Gamma_{\rm PDMF}+1)} \ , \tag{3.2}$$

where α is the normalization constant and $\Gamma_{\rm PDMF}$ is the logarithmic slope of the PDMF. This PDMF can be described by a cumulative distribution function (cdf) of the form

$$F(m) = \int_{m_{\rm lo}}^{m} f(m')\,{\rm d}m' = \frac{\alpha}{\Gamma_{\rm PDMF}}(m_{\rm lo}^{-\Gamma_{\rm PDMF}} - m^{-\Gamma_{\rm PDMF}}) \ , \tag{3.3}$$

where $m_{\rm lo}$ is the lower mass limit and $F(m)$ is the probability that a star's mass is between $m_{\rm lo}$ and m. Normalization requires that the upper mass limit, $m_{\rm up}$, follows $F(m_{\rm up}) = 1$, which yields

$$\alpha = \frac{\Gamma_{\rm PDMF}}{m_{\rm lo}^{-\Gamma_{\rm PDMF}} - m_{\rm up}^{-\Gamma_{\rm PDMF}}} \ . \tag{3.4}$$

From equations (3.3) and (3.4),

$$F(m) = \frac{1 - (m/m_{\rm lo})^{-\Gamma_{\rm PDMF}}}{1 - (m_{\rm up}/m_{\rm lo})^{-\Gamma_{\rm PDMF}}} \ , \tag{3.5}$$

which can be written as

$$\log[1 - \kappa F(m)] = -\Gamma_{\rm PDMF} \log m + \Gamma_{\rm PDMF} \log m_{\rm lo} \ , \tag{3.6}$$

where $\kappa = [1 - (m_{\rm up}/m_{\rm lo})^{-\Gamma_{\rm PDMF}}]$. In the case where $m_{\rm up} \to \infty$ then $\kappa \to 1$ or if $m_{\rm up} \gg m_{\rm lo}$ then $\kappa \simeq 1$. Following Koen (2006), the cdf $F(m)$ can be replaced by an empirical cdf given by

$$F[m(j)] = \frac{j}{(N+1)} \ , \tag{3.7}$$

where N is the number of stars in the sample, j is the rank of the star when the sample is ordered by increasing stellar mass. Thus, j goes from 1 to N, where 1 is the lowest mass star and N is the highest mass star. Using this empirical cdf, we generate a plot of $\log[1 - F(m)]$ vs. $\log m$ for the RIOTS4 sample (Figure 3.4). For

this analysis, we adopt $m_{\rm lo} = 20 M_{\odot}$, which corresponds to the selection criteria for the RIOTS4 survey (see Figure 3.3). This limit yields a sample of 130 stars from which we will derive the PDMF. It is clear from equation (3.6) that when $\kappa \rightarrow 1$, $\Gamma_{\rm PDMF}$ is simply the slope of $\log[1 - F(m)]$ vs. $\log m$ from Figure 3.4. Thus, we use a linear least squares fit to obtain $\Gamma_{\rm PDMF}$=3.5 from Figure 3.4.

We also consider the case where $\kappa < 1$. In this case, the form of the IMF assumes that of a truncated pareto distribution given by

$$\log[1 - F(m)] = \log\left[1 - \frac{1 - (m/m_{\rm lo})^{-a}}{k}\right], \tag{3.8}$$

We perform two fits to the dataset assuming this form of the IMF, a nonlinear least squares and a maximum likelihood method, given by equations (8) and (10), respectively in Koen (2006). From these fits, we find $\Gamma_{\rm PDMF}$= 2.8 using the non-linear least squares fitting and $\Gamma_{\rm PDMF}$= 3.1 using the maximum likelihood method.

Of the 130 stars contributing to this IMF measurement, Oe/Be stars account for 25% (33) of these objects. Since the spectral type and thus $T_{\rm eff}$ and mass of these stars is more uncertain, we test the impact these objects have on the PDMF slope. As we discussed in §3.3, these stars have a larger possible range in their equivalent photospheric spectral type, which we assign individually for each star. We find that adopting the earliest or latest extremes for these ranges changes the slope of the derived PDMF by 0.1 at most. Adopting the earliest spectral types changes only the non-linear fit to $\Gamma_{\rm PDMF}$= 2.9, reducing the scatter in our PDMF measurements. In contrast, adopting the latest spectral types increases the scatter, where $\Gamma_{\rm PDMF}$ = 3.6, 2.7, and 3.2 for linear and nonlinear least squares fits and maximum likelihood method, respectively. Finally, if we exclude the Oe/Be stars entirely, the remaining 97 'normal' stars exhibit a slightly steeper slope of $\Gamma_{\rm PDMF}$= 3.7, 3.2, and 3.6 for linear and nonlinear least squares fits and maximum likelihood method, respectively (see Figure 3.5). Thus, we find that the impact of Oe/Be stars on our derived mass function is small.

With an estimate of the PDMF slope, we now investigate the IMF of the SMC

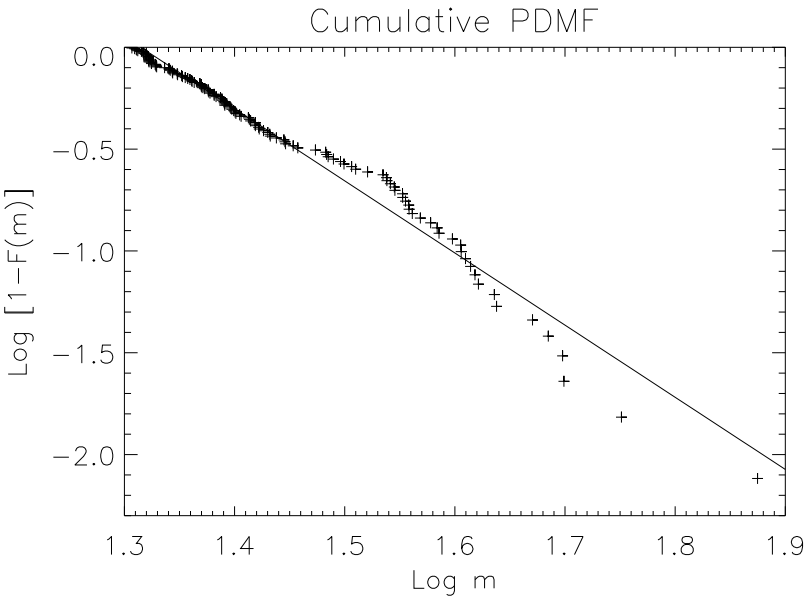

Figure 3.4. The PDMF of the SMC field star population, plotted as $\log[1 - F(m)]$ versus $\log m$, where $F(m)$ is the empirical CDF. The plotted line shows the linear least squares fit to the data, with a slope of $\Gamma_{\rm PDMF}$=3.5.

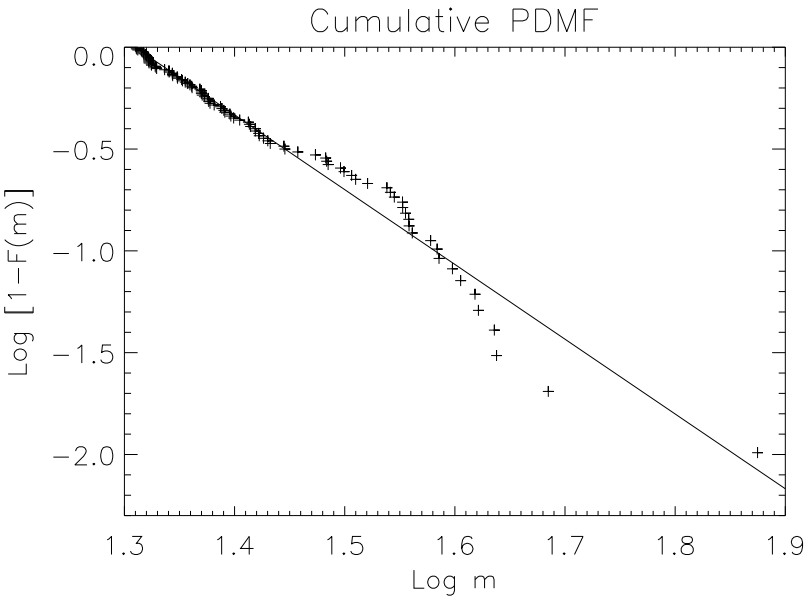

Figure 3.5. The PDMF of the SMC field star population with Oe/Be stars omitted, plotted as $\log[1 - F(m)]$ versus $\log m$, where $F(m)$ is the empirical CDF. The plotted line shows the linear least squares fit to the data, with a slope of $\Gamma_{\rm PDMF}$=3.7.

field. To find the intrinsic field IMF, we employ a simple Monte Carlo simulation to create a theoretical stellar field population assuming a continuous, fixed star formation rate. In our Monte Carlo models, we generate an artificial field population with an IMF given by $n(m)\ dm \propto m^{-(\Gamma_{\rm IMF}+1)}dm$, where we vary $\Gamma_{\rm IMF}$ between 1.0 to 4.0 in steps of 0.1. We set $m_{\rm lo} = 20M_{\odot}$ and $m_{\rm up} = 150M_{\odot}$ as fixed parameters for each simulation and assign each star a random age from 0 to $\sim 10^7$ yrs (the lifetime of a $20\mathrm{M}_{\odot}$ star) to simulate continuous star formation. Stars with ages greater than their expected lifetime are excluded for obvious reasons. For each value of $\Gamma_{\rm IMF}$, we generate 10^4 artificial field populations. For each artificial population, we include only the first 130 stars, to provide an accurate comparison with the RIOTS4 sample. With the 10^4 artificial populations, we compare the resultant distribution of PDMF slopes from each model to the observed PDMF slope from the RIOTS4 sample. We find that an input IMF of $\Gamma_{\rm IMF} = 2.3$ generates a PDMF distribution that most closely matches the the observed PDMF values from the nonlinear least squares fit and the maximum likelihood method. Figure 3.6 shows this distribution of PDMF slopes for $\Gamma_{\rm IMF} = 2.3$ in both least squares fitting and maximum likelihood methods. We can use the distribution in Figure 3.6 to estimate the error in our IMF slope using this method. Assuming a Gaussian distribution, the 1-σ error corresponds to a difference of ± 0.4 in the slope. Thus, we arrive at our final estimate of $\Gamma_{\rm IMF} = 2.3 \pm 0.4$. This slope is much steeper than the canonical Salpeter slope of $\Gamma_{\rm IMF} = 1.35$.

3.5.2 Field IMF from $7 - 20M_{\odot}$

To probe the stellar IMF of the SMC field below the detection limits of RIOTS4, we utilize BV photometry of the SMC bar from Phase II of the Optical Gravitational Lensing Experiment (OGLE; Udalski et al. 1998). Depending on the stellar density, OGLE photometry is $\sim 75 - 90\%$ complete to $B \sim 20$ and $V \sim 20.5$ (Udalski et al. 1998). Assuming a distance modulus of 18.9 for the SMC (Harries et al. 2003), these magnitudes correspond to a $3M_{\odot}$ star along the ZAMS. Therefore, we adopt $3M_{\odot}$ as the lower mass cutoff for our field star target selection from OGLE photometry. The target selection process is similar to that of the RIOTS4 survey; however, in this

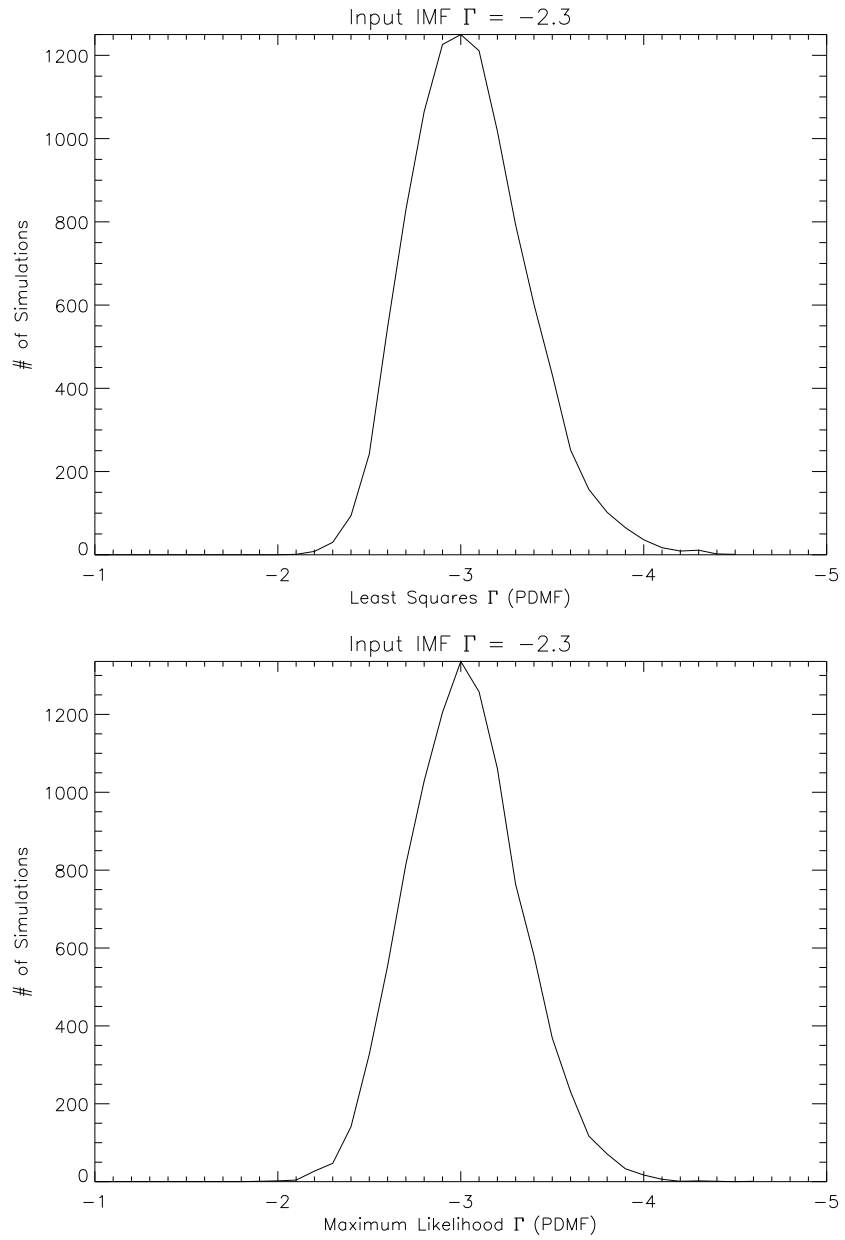

Figure 3.6. The distribution of PDMF slopes for an input IMF slope of $\Gamma_{\rm IMF} = 2.3$. Notice that these distributions peak in the range of Γ=2.8 to 3.1.

case our initial selection criteria include all stars above the $3M_{\odot}$ Geneva evolutionary track in absolute magnitude, M_V, vs. $B-V$ color (Girardi et al. 2002). In addition, we include stars that fall blueward of the main sequence evolutionary tracks with $M_V \leq 1$, which are likely main sequence stars $\geq 3M_{\odot}$. Prior to these selections, all stars are extinction-corrected using the SMC extinction maps from Zaritsky et al. (2002). With this sample, we run a new iteration of the friends-of-friends code, just as in the target selection for the RIOTS4 survey. Here, the relatively high density of the SMC bar and inclusion of lower mass stars results in a higher stellar surface density than in the RIOTS4 sample. Thus, when we maximize the total number of clusters to find the clustering length (18 pc), it is lower than in the RIOTS4 iteration of this code. Therefore, in the OGLE sample, field stars are defined as stars located at least 18 pc away from their nearest neighbor.

Figure 3.7 shows a color-magnitude contour plot of all stars included in the friends-of-friends algorithm. Stars shown in Figure 3.7 are from a single 14.2" x 52" OGLE field and represent $\sim$ 10% of the full OGLE sample. Stellar density contours of 10^0, 10^1, 10^2, and 10^3 stars per bin begin at the colors red, green, blue, and black, respectively. We also plot evolutionary tracks between $3M_{\odot}$ and $40M_{\odot}$ from Girardi et al. (2002), which are calculated from Charbonnel et al. (1993). The horizontal and vertical lines at $B-V=0.9$ depict the mean errors in $B-V$ and M_V, respectively, as they change with magnitude. The line in the upper left indicates the mean error in the extinction measurement. We also plot the distribution of $B-V$ errors vs. M_V in Figure 3.8. From Figure 3.7, the distribution of stars blueward of the ZAMS is consistent with a population of main sequence stars that are displaced due to photometric errors.

To examine the effects of photometric errors on the OGLE CMD, we generate an artificial stellar population following the Girardi et al. (2002) evolutionary tracks and then simulate their distribution in M_V vs. $B-V$ based on the uncertainties in OGLE photometry and SMC extinction values. We create this artificial stellar population from a standard Salpeter IMF, given by $n(m)\,dm \propto m^{-(\Gamma_{\rm IMF}+1)}dm$, where $\Gamma_{\rm IMF}$= 1.35, $m_{\rm lo} = 2M_{\odot}$, and $m_{\rm up} = 120M_{\odot}$. We again operate under the condition

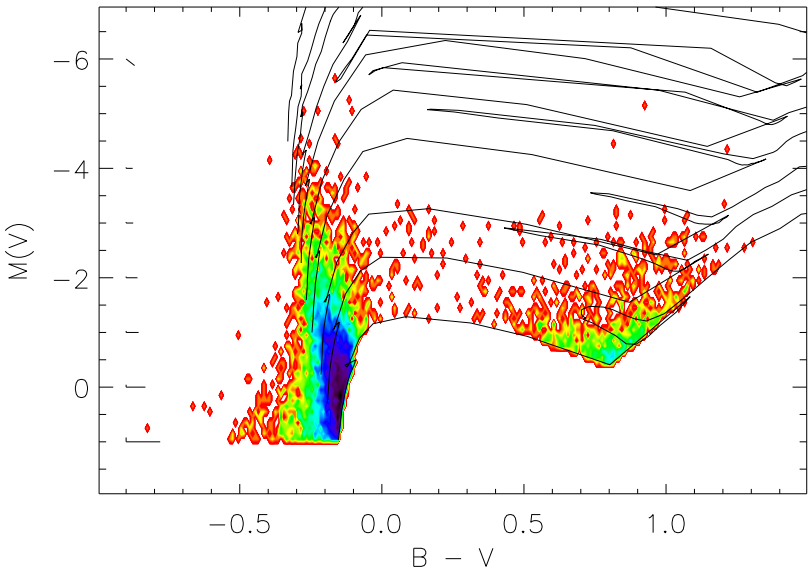

Figure 3.7. Contour plot depicting a color magnitude diagram of all stars in the SMC included in our initial selection criteria from OGLE BV photometry. The contours for 10^0, 10^1, 10^2, and 10^3 stars per bin begin at red, green, blue, and black, respectively. The Geneva evolutionary tracks (Girardi et al. 2002) range from $3 - 40 M_{\odot}$.

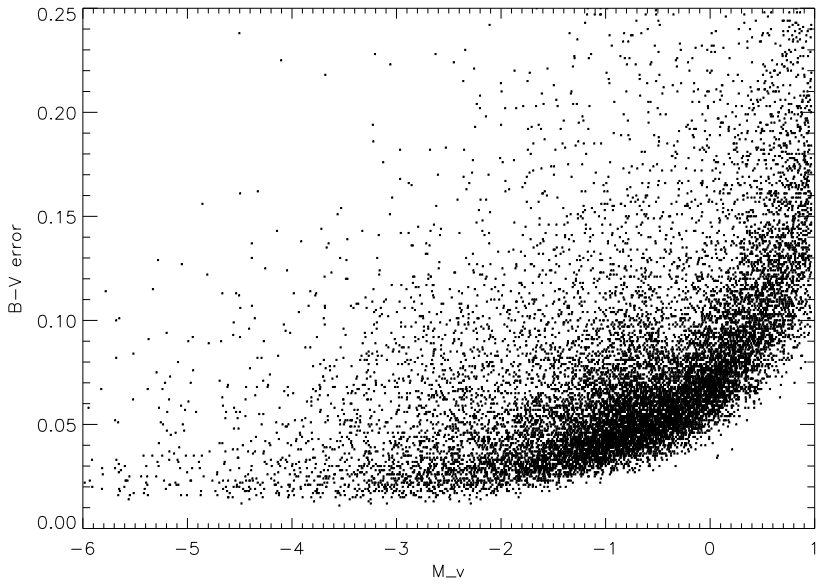

Figure 3.8. The distribution of errors in $B - V$ vs. M_V.

of continuous star formation, thus assign each star a random age from 0 to $\sim 10^9$ yrs (the lifetime of a $2M_\odot$ star). With given mass and age, we estimate M_V and $B-V$ for each star by performing a linear interpolation between the Geneva model isochrones (Girardi et al. 2002). The top panel of Figure 3.9 depicts this artificial population above $3M_\odot$ on a color-magnitude contour plot. Using this simulated photometry, we model an observation of this hypothetical population. To do this, we assign the B, V, and extinction *errors* of a real OGLE star to each of our hypothetical stars. We ensure that the difference in both B and V magnitudes between our hypothetical star and its real OGLE match is < 0.1. We degrade the hypothetical photometry based on these errors by selecting a random value from a Gaussian distribution with 1-σ given by the observed uncertainty for each error term individually. We stress that we are not modeling the photometry of these stars, but simply applying the observed OGLE errors to our model population.

The bottom panel of Figure 3.9 is a color-magnitude contour plot of our artificial population after applying the OGLE observational errors. This shows how the OGLE observational errors affect a hypothetical stellar population with a Salpeter IMF. This plot can be directly compared to the actual OGLE observations in Figure 3.7. We note the generally good agreement between our artificial population and the OGLE observations as a whole. Since we took no effort to model the actual OGLE stellar population, and only modeled the observed OGLE errors, this comparison confirms that the population blueward of the ZAMS is due to the observational errors and therefore, contains important information about the stellar IMF. However, there are three noticeable discrepancies between these plots; the redward extension of the main sequence in the OGLE data, the difference in shape of the giant populations, and the quantity of stars between the main sequence and giant populations. These discrepancies are not due to the errors, but rather represent a real difference between our model population and the OGLE observations. The main sequence offset is similar to that observed in the RIOTS4 spectroscopic data (Figure 3.3), which points to this issue arising from the stellar evolutionary models, rather than our artificial star models. The issues between the main sequence and the giant population can be

partially explained due to Galactic contamination. We investigate this contamination using the Bescanon model to estimate the different Galactic stellar populations in the direction of the SMC (Robin et al. 2003). We find that nearly all Galactic stars have $B - V > 0.4$, with the highest density of contamination from $B - V \sim 0.5 - 0.7$. This range of $B - V$ values represents the largest deviation of the giant population between the artificial model and the OGLE data. The number of stars observed in OGLE between $B - V \sim 0.4 - 0.7$ is within a factor of two of the expected Galactic contribution.

We now apply our OGLE error models not to an artificial population, but to the observed SMC field population. Using the sample of field stars identified by our friends-of-friends code, we measure the IMF of the field with a statistical approach rather than doing a basic star count per mass bin. This unique method is advantageous for two reasons: (1) we want to incorporate stars blueward of the ZAMS into our measurement of the IMF, and (2) the size of the color-magnitude parameter space coupled with the observational errors leads to very inaccurate mass estimates (e.g., Massey 2011). Thus, our method should be more accurate and include more stars than the star count per mass bin method. For each OGLE star, we generate 10^4 unique realizations of its B, V, and extinction values by selecting a random value on a Gaussian distribution centered on the observed values, where the 1-σ value of the distribution is given by the observational error for each measurement. With these 10^4 realizations, we count how many lie within each mass bin of the Geneva evolutionary tracks. From this count, we assign a fractional probability for the star's existence in each mass bin, which is calculated by the the number of realizations in that mass bin divided by the total realizations found within all mass bins. Any realizations that fall outside the Geneva evolutionary tracks are ignored as unphysical realizations and do not count towards this analysis. This ensures that each star is weighted equally for the IMF, by having a total probability over all mass bins equal to one. If we did not exclude unphysical realizations, then a star directly on the ZAMS would only have a total probably of ~ 0.5, since about half its realizations would exist blueward of the main sequence, while a star near the turnoff of the main sequence would have

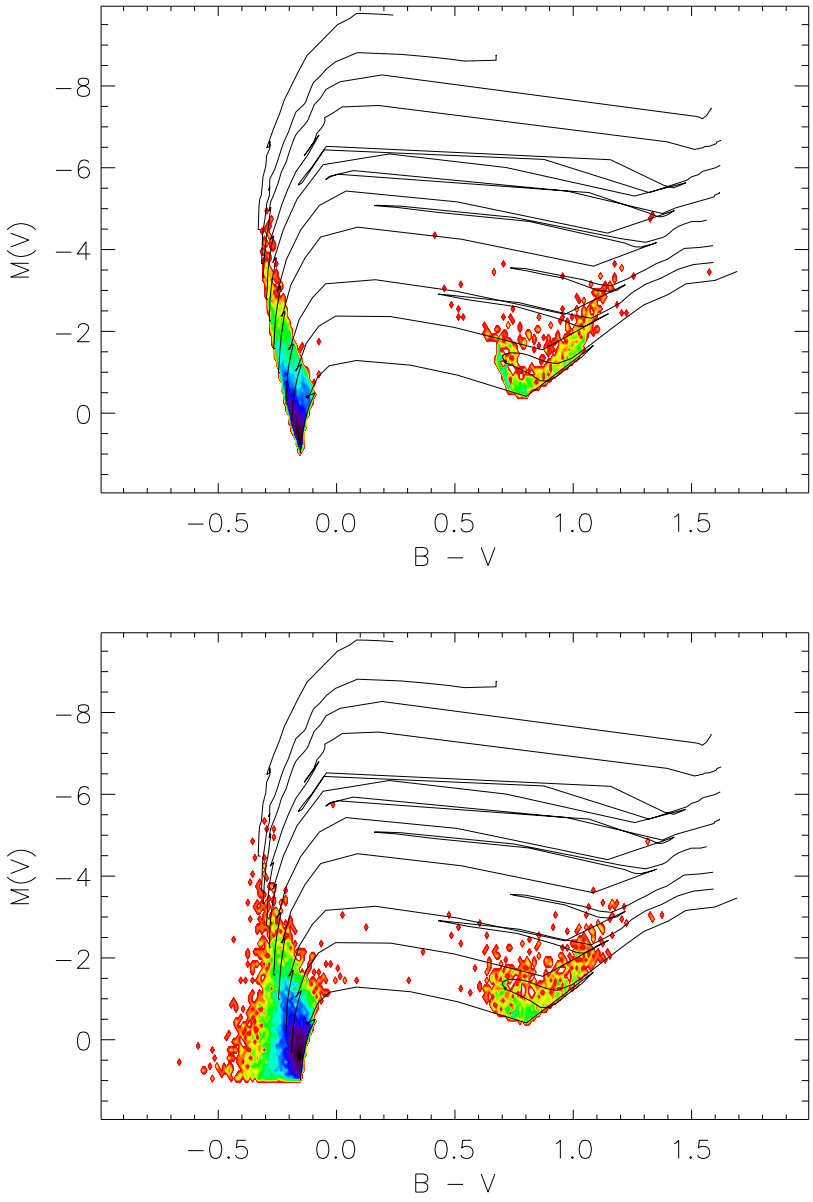

Figure 3.9. Axes, contours, and evolutionary tracks as in Figure 3.7. The top panel depicts an artificial stellar population generated from the evolutionary tracks. The bottom panel depicts the same population, with B, V, and extinction errors from the OGLE survey.

nearly all its realizations counted. Thus, we ensure that stars blueward of the main sequence are counted equally to stars near on the main sequence.

Before completing the IMF measurement, we first re-evaluate the issue of completeness for the IMF sample. We have demonstrated that stars scattering between mass bins is important, and therefore, we want our data to be complete below the mass bins we consider in our IMF measurement. In addition, some OGLE fields are only 75% complete for a ZAMS star of $3M_{\odot}$, assuming no extinction is present. Thus, to minimize completeness problems, we adopt the lower mass limit for this IMF measurement to be $7M_{\odot}$. Even for OGLE fields with the highest stellar density, completeness for $7M_{\odot}$ stars on the ZAMS is $> 95\%$ with A_V=0 or $> 90\%$ with A_V=1.

With our new lower mass limit of $7M_{\odot}$, we plot the IMF from our statistical analysis in Figure 3.10. Here, we follow the formalism of Scalo (1986), where $\log \xi$ represents the mass function in units of stars born per unit mass($M_{\odot}$) per unit area (kpc^2) per unit time (Myr). In Figure 3.10, OGLE data are plotted as asterisks, with error bars given by the poisson uncertainties. The dashed line is a linear fit to these points, which is weighted by the Poisson errors. This fit yields $\Gamma_{\rm IMF} = 2.3 \pm 0.6$. The dotted line shows a Salpeter slope of $\Gamma_{\rm IMF} = 1.35$. The most striking feature of Figure 3.10 is that the field IMF from $7 - 25M_{\odot}$ appears to gradually transition from a steep high mass slope to a Salpeter-like slope at lowest two mass bins. This turnover in the mass function may be an indication that different processes are driving the low and high mass IMF slopes of the field.

3.5.3 Combined Field IMF

With the combination of OGLE photometry and RIOTS4 spectroscopy, we are now able to fully characterize the IMF of the SMC field population above $7M_{\odot}$. In Figure 3.10, we also include a binned mass function from the RIOTS4 data, plotted as diamonds. With the superior accuracy of masses derived by spectral types, we simply tally the number of stars in each mass bin to construct the IMF above $20M_{\odot}$ for the RIOTS4 data. Due to the different methods used to identify the OGLE and RIOTS4 field samples, they must be normalized to one another. Therefore, we use the $20M_{\odot}$

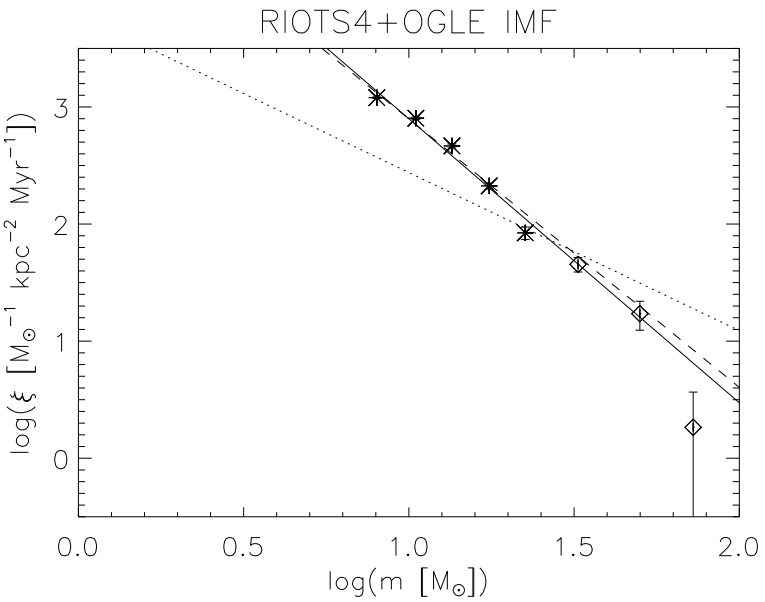

Figure 3.10. The IMF of the SMC field star population as derived from the OGLE BV photometry (dashed line) and combined OGLE plus RIOTS4 data (solid line). The slope of the dashed line is $\Gamma_{\rm IMF} = 2.3$ and solid line is $\Gamma_{\rm IMF} = 2.4$.

to $25M_{\odot}$ mass bin, which is common to both these two data sets, to normalize the RIOTS4 star count to the OGLE star count. We apply this normalization to each mass bin in the RIOTS4 data to construct the full IMF shown in Figure 3.10. Here, we see that nearly the entire mass range can be well described by a single power law with slope of $\Gamma_{\rm IMF} = 2.4 \pm 0.4$ (solid line), in full agreement with our slope derived from the cumulative distribution function of the RIOTS4 masses ($\Gamma_{\rm IMF} = 2.3 \pm 0.4$). Only at the lowest bins does a turnover in the power law begin to appear. We emphasize that this turnover is not an effect of incompleteness, since the OGLE data is $> 90\%$ complete for a $7M_{\odot}$ ZAMS star with $A_V = 1$, whereas the typical extinction towards the SMC is ~ 0.5 mag (Zaritsky et al. 2002).

3.6 Discussion

3.6.1 Effects of Binary Star Systems

Recent studies indicate that the massive star binary fraction is quite high, with observations of open clusters (e.g. Sana et al. 2008, 2009, 2011) and massive clusters

(Kiminki & Kobulnicky 2012) indicating lower limits of 60% and 70%, respectively. Our own analysis of the field binary fraction using ~ 10 epochs of observations for 30 RIOTS4 stars reveals a binary fraction $> 50\%$ (Lamb et al. in prep). However, the fraction of RIOTS4 spectra that exhibit clear indications of binarity is small. Thus, a large fraction of undetected binaries is a concern for our IMF measurements. If a binary system is treated as a single star, the excess flux will result in an overestimate of the mass of the primary. Additionally, if the secondary star is $> 20M_{\odot}$, then its absence from the IMF will further bias the star count in favor of the higher mass bins. To quantify the magnitude of this effect, we design a simple Monte Carlo code to examine the ramifications of undetected binaries on our observed PDMF in RIOTS4.

In this analysis, we assume that each object in the RIOTS4 survey is in an undetected binary system. The primary stars in these binary systems are assumed to have the OGLE4 derived spectral types, with a possible mass range from $20M_{\odot}$ to $75M_{\odot}$. We randomly assign each binary system a mass ratio, $q = m_2/m_1$, which is uniformly distributed from 0.01 to 1. This uniform distribution in q is motivated by recent observational studies of the binary mass ratios in open and massive clusters (see e.g. Sana & Evans 2011; Kiminki & Kobulnicky 2012). In comparison with a Salpeter distribution of secondary masses, this uniform distribution in q will have a higher fraction of massive secondaries and more strongly affect the IMF results. With these mass ratios, we use a simple power law mass-luminosity relationship to split the observed light into two separate binary components. We recalculate the magnitude of the primary star using

$$m_{\rm bol,1} = m_{\rm bol} - 2.5 \log \left[\frac{1}{1+q^{\delta}} \right] , \tag{3.9}$$

where $m_{\rm bol}$ is the derived bolometric magnitude of the binary system, $m_{\rm bol,1}$ is the bolometric magnitude of the primary star, q is the mass ratio of the binary system, and δ is the power law of the mass-luminosity relationship, given by $L \propto m^{\delta}$. With $m_{\rm bol,1}$ and $T_{\rm eff}$, we derive the mass of the primary as in §3.4 under the assumption that the observed stellar spectrum, and thus our adopted $T_{\rm eff}$, accurately reflect the physical

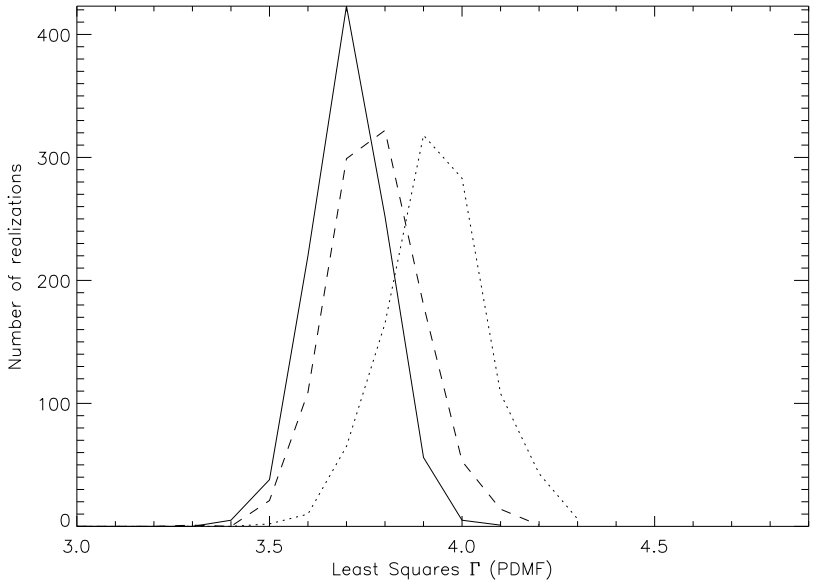

Figure 3.11. The distribution of PDMF slopes for RIOTS4 if all stars are in undetected binary systems. The solid, dashed, and dotted lines represents simulations with $\delta = 3$, 2, and 1, respectively. We display slopes from the linear least squares fit for this analysis, for which our derived RIOTS4 PDMF slope is $\Gamma_{\rm PDMF} = 3.5$.

properties of the primary star. With these derived primary masses and secondary masses given directly by q, we recreate the RIOTS4 PDMF with a 100% undetected binary fraction and measure its slope accordingly. We perform this analysis 10^3 times for each of three different mass-luminosity relationships, given by $\delta = 1$, $\delta = 2$, and $\delta = 3$. For simplicity, we opt to include only single power law models, rather than a broken power law for the mass-luminosity relationship. These different values of δ encompass the range of values expected at both high stellar masses $\delta \sim 1$ and lower stellar masses $\delta = 3$ and represent the cases of maximal and minimal impact on the IMF, respectively.

The distribution of linear least squares PDMF slopes for these Monte Carlo simulations can be found in Figure 3.11. Simulations with $\delta = 1$, 2, and 3 are plotted with dotted, dashed, and solid lines, respectively. These distributions can be directly compared with our measured RIOTS4 linear least squares PDMF slope of $\Gamma_{\rm PDMF} = 3.5$. Figure 3.11 shows that undetected binaries will only cause a steepening of the RIOTS4 PDMF slope. The degree of steepening ranges from 0.2 to 0.4 and depends weakly

on the power law slope of the mass-luminosity relationship. Finally, we perform one additional simulation of the extreme case where all RIOTS4 stars are in undetected equal mass binaries, which results in $\Gamma_{\rm PDMF} = 4.5$. Thus, we clearly demonstrate that undetected binary systems will only serve to steepen the PDMF and therefore, IMF of the field. Thus, undetected binaries cannot be the source of the steep high mass field IMF.

3.6.2 Star Formation History

One critical assumption made heretofore in this work is that the star formation rate in the SMC has remained constant for the last $\sim$ 10 Myr. Here, we investigate the possibility that a recent burst of star formation could be responsible for the steep field IMF. To perform this analysis, we proceed as in Section 3.5.1 by generating a theoretical population and measuring its PDMF for the purposes of comparing it with the observed RIOTS4 PDMF. For each model, in addition to a continuous star formation rate, we add a burst of star formation. However, here, we always use the canonical Salpeter IMF to generate both the continuous and bursting stellar populations. With these models, we investigate how the time since the burst, duration of the burst, and the star formation rate of the burst affect the output PDMF of the model. We restrict our models to bursts beginning within the last 10 Myr, which is approximately the lifetime of a $20 M_{\odot}$ star. For each set of model parameters, we generate 10^4 theoretical populations and as before, we plot the distribution of PDMF slopes for each model. Covering each variable in turn, we find that the higher the star formation rate of the burst, the more it steepens the PDMF. The duration of the burst, however, exhibits more subtle behavior. A burst too long in duration tends to mimic the PDMF of continuous star formation. Likewise, a burst that is too short also does not significantly alter the PDMF. In most cases, the maximum effect on the PDMF occurs for a burst duration of $\sim$ 5 Myr. Finally, we find that bursts ending $<$ 3 Myr ago generate too many high mass stars, making these models incompatible with our observed slope and highest mass star.

In addition to tracking the distribution of PDMF slopes, we also investigate how

the star formation history affects the shape of the PDMF and IMF. Since the shape of individual models can differ significantly from one population to the next, we generate a ranked order of masses for each iteration of the model and take the average value at each rank to create the model PDMF. For example, we take the most massive star from each iteration for a given model and average these values to get the most massive star of the model PDMF. This process continues for each of the N stars in the burst models, where N is the number of stars $> 20M_{\odot}$ from the RIOTS4 survey. Since there is no guarantee that we will form a given number stars in a given model, we always take the first 130 stars $> 20M_{\odot}$ to ensure a direct comparison to our RIOTS4 sample. We also extend this ranked average of stars down to $7M_{\odot}$ so we can make a direct comparison of the averaged IMF of these models with the combined RIOTS4 and OGLE IMF.

The model that most closely matches the observed PDMF is a burst of star formation that begins 8 Myr ago, lasts for 5 Myr, and does not include any continuous star formation component along with the burst. Figure 3.12 shows the distribution of PDMF slopes for this best burst model, which are in agreement with the $\Gamma = 2.8-3.1$ observed for RIOTS4. Figure 3.13 depicts the averaged cumulative PDMF for the best burst model, which can be directly compared with the observed PDMF from RIOTS4 (Figure 3.4). Similarly, Figure 3.14 shows the averaged IMF of the best burst model and can be compared with the RIOTS4 and OGLE combined IMF. To compare the averaged PDMF distribution with the observed RIOTS4 PDMF distribution, we use a KS test and find a 90% likelihood that these populations were drawn from the same parent population. However, this agreement does not extend below $20M_{\odot}$. As seen in Figure 3.14, the averaged IMF of the best burst model turns over much more rapidly below $20M_{\odot}$ than the combined RIOTS4 and OGLE IMF. A KS test comparing these two populations still finds a 68% likelihood they were drawn from the same parent population, but with the small number of data points, this percentage may be an overestimate.

Therefore, we find some evidence that for a narrow range of burst parameters, it is possible that the observed PDMF of the SMC field can be reconciled with the

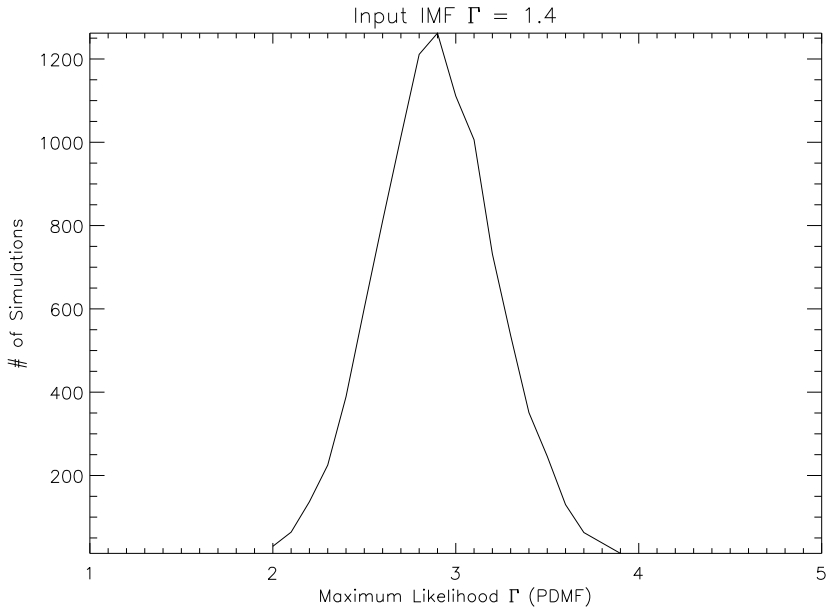

Figure 3.12. The distribution of PDMF slopes for the best burst model. As in Figure 3.6 these distributions agree with the observed RIOTS4 PDMF slope of $\Gamma = 2.8 - 3.1$.

canonical Salpeter IMF from our RIOTS4. However, with inclusion of the OGLE data, the shape of the mass function does not represent a smooth power law as seen in the combined RIOTS4 and OGLE IMF. Thus, it is unlikely that the observed PDMF is due solely to a recent burst of star formation.

3.7 Conclusions

We conduct an extensive survey targeting a spatially complete sample of field massive stars in the Small Magellanic Cloud (SMC). This Runaways and Isolated O Type Star Spectroscopic Survey of the SMC (RIOTS4) uses the IMACS multi-object spectrograph on the Magellan Baade telescope and the MIKE echelle spectrograph on the Magellan Clay telescope. Targets for RIOTS4 come from Oey et al. (2004), who identify a sample of 374 candidate field massive stars using photometry to select massive stars and a friends-of-friends algorithm to ensure isolation. A total of 284 objects yield spectra of sufficient quality to derive their effective temperatures to within ~ 1500 K and calculate their bolometric luminosities with photometry from Massey (2002). These physical properties yield stellar mass estimates typically accurate to

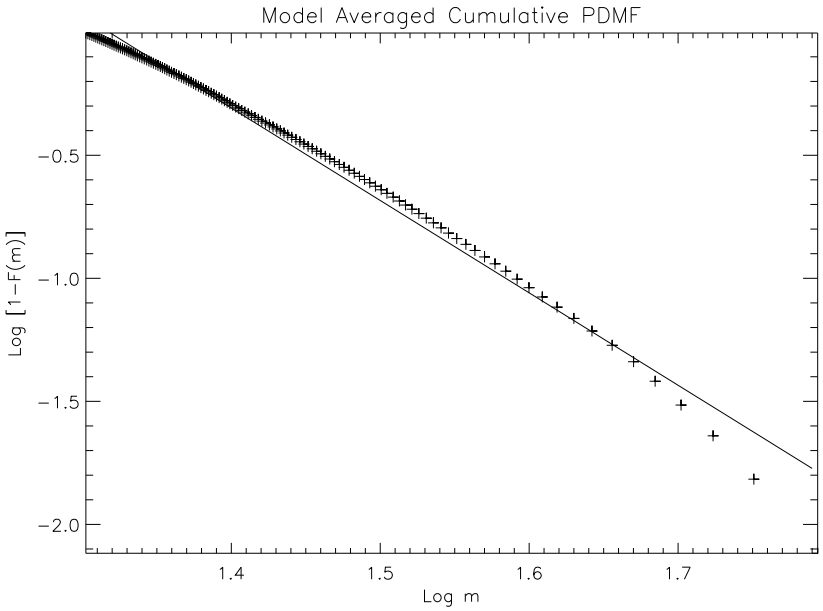

Figure 3.13. The averaged PDMF of the best burst model, plotted as in Figure 3.4.

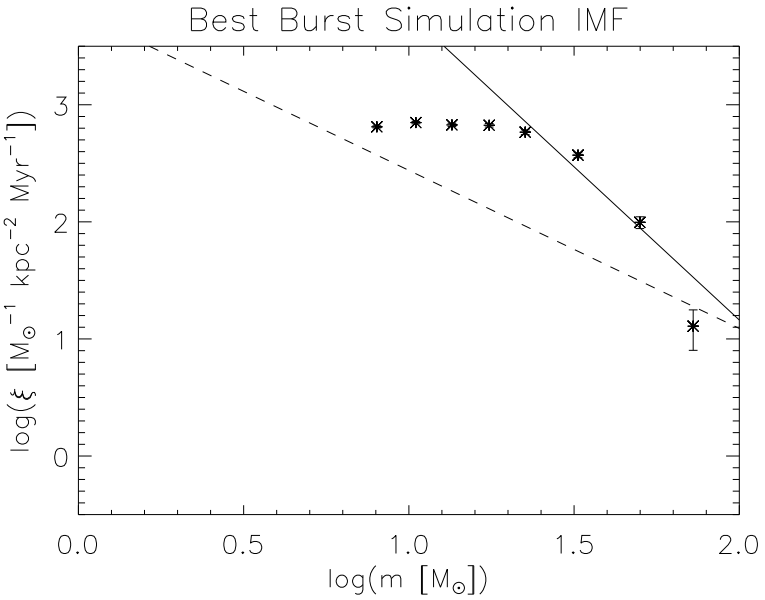

Figure 3.14. The averaged IMF of the best burst model, plotted as in Figure 3.10. Notice the steep turnover in comparison with Figure 3.10.

$\sim 2M_{\odot}$. The majority of stars without derived physical properties are Oe/Be stars with weak or filled-in diagnostic lines, which prevents accurate spectral classification.

RIOTS4 is complete to $\sim 20M_{\odot}$ along the main sequence. We therefore include the 130 stars with mass $\geq 20M_{\odot}$ in our analysis of the stellar IMF of the field. Following the methodology of Koen (2006), we obtain a slope of $\Gamma_{\rm PDMF} = 2.8$ to 3.5 for the present day mass function (PDMF) of the field population. To obtain the field IMF, we use a simple Monte Carlo model to generate 10^4 artificial field populations for a variety of input IMF slopes ranging from $\Gamma_{\rm IMF}$=1.0 to 4.0. Assuming continuous star formation, we measure the distribution of the PDMF slopes of these different models. The model PDMF distribution that best matched our observed PDMF slope was for an input $\Gamma_{\rm IMF}$=2.3$\pm$0.4. Thus, we find that the field IMF is much steeper than the canonical Salpeter slope of $\Gamma_{\rm IMF}$=1.35.

To extend our field IMF to lower masses, we use BV photometry from OGLE. Using selection techniques similar to those for RIOTS4 targets, we identify a sample of field stars $\geq 7M_{\odot}$ from the OGLE survey. We employ a statistical methodology to measure the field IMF from the OGLE data. We randomly select values from a Gaussian distribution of the individual B, V and extinction errors, which we use to generate 10^4 realizations of the photometry for each OGLE field star. We treat these realizations as a probability distribution in M_V vs. $B-V$, and divide each star fractionally into different mass bins by counting the proportional contribution of realizations to each bin. In this way, we account for stars that were displaced outside of the evolutionary models due to photometric errors. From the OGLE data, we derive an IMF slope of $\Gamma_{\rm IMF}$=2.3$\pm$0.6 for the mass range $7M_{\odot} - 20M_{\odot}$. This IMF exhibits a steep slope at higher mass and gradually turns over into a slope approaching Salpeter, $\Gamma_{\rm IMF}$=1.35, at the lowest two mass bins. We combine this OGLE IMF measurement with an IMF derived from counting the number of stars per mass bin of the RIOTS4 data to get a field IMF above $7M_{\odot}$. The slope for this combined IMF is $\Gamma_{\rm IMF}$=2.4$\pm$0.4, which again is well above the canonical Salpeter slope (Figure 3.10).

One of the major potential sources of error in our IMF is the presence of a signif-

icant, undetected binary population. To account for this possible scenario, we model the RIOTS4 population as if every star is a member of a binary system. We select the binary mass ratio $q = m_2/m_1$ randomly from a uniform distribution from 0.01 to 1 and split the light according to a mass-luminosity relationship, $L \propto m^{\delta}$, where $\delta = 1$, 2, or 3. We find that this 100% binary fraction has a steepening effect on the observed RIOTS4 PDMF slope, in the range of 0.2-0.4, depending on the value of δ, with a steeper power law having a smaller effect on the IMF.

Finally, we investigate the possibility that a unique star formation history of the SMC combining with a Salpeter IMF could result in the observed steep PDMF. We model a range of bursting star formation histories, by varying the burst duration, burst strength, and time elapsed since the burst occurred. We find one 'best burst' model that closely matches the $\Gamma = 2.8 - 3.1$ slope of the PDMF from RIOTS4. This is a burst that begins 8 Myrs ago, lasts for 4.5 Myrs, and has no other star formation occurring during the previous 10 Myrs (100% burst). However, the 'best burst' model IMF flattens dramatically below $20M_{\odot}$, which is a feature not seen in the OGLE IMF. Thus, a burst of star formation can not fully explain the steep SMC field star IMF.

In summary, we employ a number of methods to measure the IMF of the SMC field using spectroscopy from the RIOTS4 survey combined with photometry from Massey (2002) and photometry from the OGLE survey. In these analyses, we find an IMF slope of $\Gamma_{\rm IMF} = 2.3$ - 2.4 for the high mass SMC field population, which is significantly steeper than the canonical Salpeter IMF with $\Gamma_{\rm IMF} = 1.35$. Although not as steep, our results confirm those of previous studies of the SMC, which found a steep field IMF slope of $\Gamma \sim 3 - 4$ for stars $> 25M_{\odot}$ (Massey et al. 1995; Massey 2002). If the field population originates largely from sparse and in situ star formation, then our results would suggest the existence of a deterministic $M_{\rm cl} - m_{\rm max}$ relationship. If such a $M_{\rm cl} - m_{\rm max}$ relationship exists, then the IGIMF effect (Weidner & Kroupa 2005) necessitates that the field IMF must be steeper than the canonical Salpeter IMF (Weidner & Kroupa 2005). Thus, the steep field IMF may be an indication that field massive stars form through a different mechanism than those in clusters. Given

the steep IMF, it seems unlikely that runaways make up a significant portion of the field, since they are more common at higher masses (e.g., Stone 1991). However, if a significant runaway fraction exists, then it would indicate that the field components formed in sparse environments or in situ have an even steeper IMF than we observe.

Table 3.1: RIOTS4 Spectral Catalog

ID	**B**	**V**	**Q**	$\mathbf{M_{bol}}$	$\mathbf{A_V}$	$\mathbf{T_{eff}}$ **(K)**	**Mass** ($M_\odot$)	**Sp Type**
1600	14.42	14.60	-11.15	-0.87	0.32	33000	$23.6\ ^{+1.7}_{-1.5}$	O9 V
3459	13.32	13.46	-12.30	-0.93	0.48	33000	$35.9\ ^{+3.3}_{-5.0}$	O9 III
4919	13.66	13.85	-11.34	-0.95	0.33	29250	$26.2\ ^{+4.1}_{-4.7}$	B0.2 III
5313	14.89	15.11	-10.78	-0.87	0.23	34500	$20.9\ ^{+1.8}_{-1.5}$	O8.5 V
7437	12.93	13.12	-14.32	-0.94	0.33	42250	$75.0\ ^{+5.4}_{-4.7}$	O6 III((f))
7782	14.30	14.46	-12.30	-0.91	0.40	37750	$33.2\ ^{+2.4}_{-2.2}$	O7.5 V
9732	14.63	14.81	-11.63	-0.88	0.31	39250	$27.1\ ^{+2.7}_{-2.2}$	O7 Vz
11045	14.80	15.01	-11.37	-0.87	0.21	34500	$24.9\ ^{+2.6}_{-1.8}$	O8.5 V
11623	14.12	14.13	-11.79	-0.86	0.83	33000	$28.4\ ^{+3.4}_{-1.2}$	O9 V
11677	14.47	14.46	-10.82	-1.01	1.04	33000	$21.0\ ^{+1.6}_{-1.4}$	O9 V
11777	13.76	13.88	-11.03	-0.92	0.53	28500	$24.4\ ^{+1.6}_{-3.4}$	B0.5 III
11802	14.62	14.59	-10.64	-0.86	0.96	29250	$21.3\ ^{+1.6}_{-2.6}$	B0.2 V
13075	12.93	13.05	-12.25	-0.89	0.52	30000	$38.5\ ^{+3.6}_{-3.8}$	B0 III
13831	13.91	14.06	-10.71	-0.87	0.39	26750	$22.5\ ^{+3.9}_{-3.5}$	B0.5 III
13896	13.56	13.76	-12.83	-0.98	0.30	37750	$40.3\ ^{+3.2}_{-2.6}$	O7.5 III((f))
14324	14.17	14.11	-13.53	-0.97	1.12	43500	$50.0\ ^{+3.7}_{-9.5}$	Oe5.5 V((f))
14878	14.11	14.25	-11.03	-0.89	0.46	33000	$22.3\ ^{+1.9}_{-1.5}$	O9 V
15060	14.11	14.29	-10.45	-0.88	0.30	26750	$20.7\ ^{+3.7}_{-3.5}$	B0.5 III
15271	13.36	13.54	-13.85	-0.94	0.39	45000	$56.4\ ^{+3.9}_{-13.5}$	Oe5 V(f)
15742	13.51	13.64	-12.07	-0.92	0.53	33000	$32.4\ ^{+3.0}_{-1.7}$	O9 V
16147	14.03	14.15	-10.74	-0.91	0.53	28500	$21.9\ ^{+2.1}_{-2.7}$	B0.5 III
16230	13.01	13.20	-12.44	-0.90	0.29	33000	$38.4\ ^{+2.8}_{-2.5}$	O9 III
16481	14.16	14.26	-11.36	-0.94	0.62	31500	$26.0\ ^{+1.4}_{-1.9}$	O9.5 V
16518	13.77	13.90	-11.22	-0.96	0.53	30000	$24.6\ ^{+2.6}_{-1.5}$	B0 V
16587	13.99	13.91	-11.22	-1.00	1.24	30000	$24.6\ ^{+2.6}_{-1.6}$	B0 V
17240	14.37	14.47	-12.17	-0.85	0.55	37000	$32.1\ ^{+3.6}_{-4.0}$	O7.5-8 V

Table 3.1 – *Continued from previous page*

ID	B	V	Q	M_{bol}	A_V	T_{eff} (K)	Mass ($M_\odot$)	Sp Type
18329	14.64	14.65	-11.51	-0.98	0.91	36250	$25.2\ ^{+2.6}_{-1.7}$	O8 III(f)
19382	14.27	14.31	-10.80	-0.96	0.81	29250	$21.9\ ^{+2.3}_{-3.2}$	B0.2 V
19728	12.49	12.59	-10.14	-0.89	0.59	20500	$23.4\ ^{+3.0}_{-2.4}$	B1.5 Ib
21844	14.09	14.18	-12.45	-0.86	0.57	37750	$35.1\ ^{+2.1}_{-2.4}$	O7.5 III((ff))
21877	14.96	15.10	-11.58	-0.95	0.46	39250	$26.9\ ^{+2.7}_{-2.3}$	O7 Vz
22321	13.70	13.69	-12.78	-0.98	1.00	37750	$40.7\ ^{+6.7}_{-5.7}$	Oe8 V
22451	13.98	14.14	-11.48	-0.93	0.41	33000	$25.9\ ^{+2.2}_{-2.0}$	O9 III
24213	14.17	14.34	-10.61	-0.88	0.31	28500	$20.7\ ^{+1.2}_{-2.3}$	B0.5 III
25282	14.73	14.74	-10.56	-0.90	0.90	30000	$20.3\ ^{+1.5}_{-3.1}$	Be0 V
27736	14.54	14.54	-10.67	-0.99	0.95	30000	$21.0\ ^{+1.6}_{-1.5}$	Be0 V
30744	14.24	14.30	-11.42	-0.88	0.66	33000	$25.4\ ^{+2.0}_{-1.8}$	O9 V
33823	14.45	14.62	-10.66	-0.89	0.35	30000	$20.9\ ^{+1.6}_{-1.4}$	B0 III
34005	14.80	15.01	-10.87	-1.02	0.29	33000	$21.3\ ^{+1.7}_{-1.5}$	O9 V
34457	13.74	13.93	-11.18	-0.91	0.30	30250	$24.6\ ^{+1.9}_{-3.0}$	O9.7 I
35491	14.66	14.71	-12.06	-0.90	0.77	37750	$30.4\ ^{+2.2}_{-2.0}$	O7.5 V
35598	14.88	15.15	-10.99	-0.94	0.05	36250	$22.3\ ^{+1.8}_{-1.9}$	O8 V
36175	12.64	12.68	-10.60	-0.85	0.73	22500	$23.4\ ^{+6.9}_{-2.4}$	B1 I
36213	13.21	13.38	-11.91	-0.90	0.38	31500	$31.3\ ^{+2.9}_{-3.2}$	O9.5 III+B
36325	15.02	14.88	-10.99	-0.88	1.33	32750	$22.1\ ^{+2.2}_{-2.7}$	O9-9.5 V
36514	15.01	15.15	-10.73	-0.87	0.47	33000	$20.5\ ^{+1.6}_{-1.3}$	O9 V
37502	14.65	14.62	-11.08	-1.03	1.10	30000	$24.2\ ^{+2.0}_{-2.1}$	Be0 V
38024	14.32	14.53	-13.38	-0.94	0.27	47750	$48.4\ ^{+1.6}_{-3.6}$	O4 Vz
38036	14.28	14.33	-12.45	-0.98	0.82	39250	$34.5\ ^{+2.5}_{-2.0}$	Oe7 III
38921	14.07	14.12	-11.59	-0.96	0.80	30000	$27.9\ ^{+3.7}_{-1.6}$	B0 III
40380	14.22	14.33	-12.14	-0.92	0.58	39250	$31.6\ ^{+2.8}_{-2.5}$	O7 V
42260	14.43	14.54	-11.12	-0.85	0.50	31500	$23.5\ ^{+1.7}_{-1.7}$	O9.5 V
43724	14.05	14.25	-12.53	-0.96	0.32	39250	$35.7\ ^{+2.6}_{-2.6}$	O7 Vz((f))
46022	14.74	14.85	-10.75	-0.84	0.52	31500	$20.8\ ^{+1.5}_{-1.4}$	O9.5 V
46035	14.05	14.24	-12.52	-0.95	0.34	39250	$35.7\ ^{+2.2}_{-2.6}$	O7 V
46090	14.58	14.66	-10.55	-0.88	0.64	30000	$20.4\ ^{+1.3}_{-3.2}$	Be0 V
46317	14.53	14.76	-10.99	-0.90	0.17	33000	$22.1\ ^{+1.7}_{-1.5}$	O9 V
46831	15.05	15.15	-11.11	-0.87	0.54	34500	$22.8\ ^{+4.2}_{-3.1}$	O8.5 V

Table 3.1 – *Continued from previous page*

ID	B	V	Q	M_{bol}	A_V	T_{eff} (K)	Mass ($M_\odot$)	Sp Type
47478	14.74	14.96	-11.83	-0.98	0.28	39250	$28.7\ ^{+2.6}_{-2.5}$	O7 V
48037	14.56	14.54	-11.07	-1.00	1.03	30000	$24.1\ ^{+2.0}_{-1.8}$	Be0 V
48170	14.16	14.29	-11.26	-0.96	0.53	32750	$24.5\ ^{+1.7}_{-3.2}$	O9-9.5 V
48601	13.58	13.71	-11.76	-0.92	0.49	29750	$30.5\ ^{+1.2}_{-7.1}$	B0 I
49450	14.07	14.22	-10.89	-0.86	0.37	28500	$22.9\ ^{+1.9}_{-3.1}$	B0.5 V
49580	14.22	14.38	-11.18	-0.88	0.39	31500	$23.8\ ^{+1.9}_{-1.7}$	O9.5 V
50095	14.48	14.51	-12.71	-0.94	0.87	36250	$39.6\ ^{+2.8}_{-3.5}$	O8+B
50609	12.43	12.55	-10.86	-0.90	0.53	22500	$26.4\ ^{+3.9}_{-3.0}$	B1 I
50791	15.04	15.19	-11.07	-0.93	0.47	36250	$22.7\ ^{+1.8}_{-1.9}$	O8 V
50825	14.58	14.84	-11.80	-0.92	0.08	37000	$27.9\ ^{+3.7}_{-2.9}$	O7.5-8 V
51373	13.72	13.79	-12.83	-1.08	0.84	39250	$40.3\ ^{+7.1}_{-5.4}$	Oe7.5 III
51435	14.92	15.12	-10.83	-0.89	0.29	33000	$21.0\ ^{+1.7}_{-1.4}$	O9 V
51500	14.72	14.97	-12.55	-0.93	0.15	43500	$36.1\ ^{+2.7}_{-1.7}$	O5.5 V
52363	14.80	14.98	-11.37	-0.97	0.38	36250	$24.5\ ^{+2.0}_{-1.9}$	Oe8 V((f))
52410	13.69	13.75	-13.36	-1.07	0.85	39250	$49.9\ ^{+4.2}_{-3.2}$	Oe7IV
53042	14.67	14.85	-10.70	-0.86	0.28	31500	$20.4\ ^{+1.6}_{-1.7}$	O9.5 V
53360	15.04	15.09	-11.65	-0.95	0.77	39250	$27.4\ ^{+2.7}_{-2.5}$	Oe7 V
54721	12.69	12.88	-12.22	-0.95	0.35	31500	$36.4\ ^{+3.2}_{-3.5}$	O9.5 III
56503	14.87	14.95	-11.37	-0.92	0.68	33000	$25.0\ ^{+2.1}_{-1.7}$	Oe9 V
58947	13.63	13.63	-10.81	-0.85	0.74	26000	$23.4\ ^{+3.4}_{-2.4}$	B1 III
59319	14.23	14.32	-12.67	-0.99	0.68	42250	$37.0\ ^{+2.6}_{-1.6}$	Oe6 V
59977	14.81	14.81	-10.87	-0.98	0.94	33000	$21.3\ ^{+1.7}_{-1.5}$	O9 IIIe
60460	14.74	14.98	-10.84	-0.88	0.09	33000	$21.1\ ^{+1.7}_{-1.4}$	O9 V
61842	13.38	13.47	-10.34	-0.87	0.59	23500	$21.0\ ^{+5.3}_{-2.0}$	B1-1.5 I
62416	14.59	14.68	-10.78	-0.92	0.61	31500	$21.1\ ^{+1.5}_{-1.6}$	O9.5 V
63284	13.38	13.49	-10.43	-0.85	0.50	24250	$21.0\ ^{+4.3}_{-2.0}$	Be1 II
63413	13.97	13.90	-10.95	-0.89	1.10	30750	$23.0\ ^{+1.0}_{-1.4}$	O9.5 Ia
64773	15.05	15.25	-10.72	-0.87	0.23	33750	$20.5\ ^{+2.6}_{-2.0}$	O8.5-9 V
65346	14.99	15.19	-10.65	-0.99	0.36	36250	$20.9\ ^{+1.6}_{-1.9}$	08 V
65355	14.71	14.91	-11.58	-0.92	0.28	37750	$25.9\ ^{+2.7}_{-1.6}$	O7.5 V
66415	13.08	13.25	-12.03	-0.91	0.38	30500	$34.5\ ^{+2.1}_{-4.3}$	O9.7 Ia
67060	14.43	14.63	-13.04	-0.94	0.28	39250	$43.2\ ^{+3.7}_{-2.8}$	O7 Vz

Table 3.1 – *Continued from previous page*

ID	B	V	Q	M_{bol}	A_V	T_{eff} (K)	Mass ($M_\odot$)	Sp Type
67269	14.56	14.73	-11.75	-0.93	0.40	37000	$27.8\ ^{+3.3}_{-3.3}$	O7.5-8 V
67673	14.80	14.84	-11.56	-1.00	0.83	36250	$25.5\ ^{+2.6}_{-1.5}$	Oe8 V
67893	13.92	13.97	-12.45	-1.05	0.87	37750	$35.1\ ^{+2.6}_{-2.4}$	Oe7.5 V
68427	13.52	13.51	-11.34	-1.06	1.09	29250	$26.2\ ^{+1.0}_{-2.8}$	Be0.2 III
68621	14.41	14.64	-11.00	-0.94	0.20	33000	$22.1\ ^{+1.9}_{-1.5}$	O9 V
68756	14.30	14.48	-11.60	-0.94	0.34	37750	$26.2\ ^{+2.5}_{-1.8}$	O7.5 III((f))
69460	14.82	14.95	-12.99	-0.99	0.53	41000	$41.1\ ^{+2.7}_{-3.1}$	Oe6.5 V(f)
69555	14.35	14.59	-11.99	-0.96	0.17	41000	$30.4\ ^{+2.1}_{-2.5}$	O6.5 Vz
69630	13.79	14.01	-10.38	-0.85	0.16	24250	$21.0\ ^{+2.4}_{-2.0}$	B1 II
70149	14.41	14.61	-11.17	-0.90	0.25	31500	$23.8\ ^{+1.8}_{-2.0}$	O9.5 V
71002	13.75	13.97	-11.29	-0.93	0.23	31500	$24.9\ ^{+1.6}_{-1.9}$	O9.5 V
72204	14.34	14.57	-11.27	-0.92	0.20	36250	$23.8\ ^{+1.6}_{-1.9}$	O8 V+neb
72208	12.41	12.54	-9.71	-0.89	0.48	19000	$21.0\ ^{+2.4}_{-2.0}$	B2 I
72535	13.42	13.45	-13.15	-1.11	1.00	37750	$46.8\ ^{+3.6}_{-3.3}$	O7.5 V
72724	14.25	14.42	-10.63	-0.87	0.34	30000	$20.8\ ^{+1.6}_{-1.4}$	B0 V
73337	12.96	13.12	-12.84	-0.96	0.47	36250	$41.8\ ^{+3.8}_{-3.2}$	O8 III+B
73355	14.26	14.36	-11.16	-0.93	0.59	30000	$24.6\ ^{+2.2}_{-1.8}$	Be0 V
73913	13.57	13.63	-11.69	-0.91	0.72	31500	$26.4\ ^{+5.3}_{-1.0}$	O9.5 III
73952	12.51	12.62	-9.67	-0.88	0.52	19000	$21.0\ ^{+2.4}_{-2.0}$	B2 I
75126	14.65	14.39	-11.23	-1.14	2.02	33000	$24.1\ ^{+1.0}_{-1.6}$	O9 V
75210	14.57	14.67	-10.87	-0.89	0.59	34500	$21.3\ ^{+2.0}_{-1.4}$	O8.5 V
75689	14.31	14.34	-11.66	-1.08	0.94	36250	$27.0\ ^{+2.1}_{-2.3}$	Oe8 V
75919	14.32	14.39	-11.15	-1.01	0.78	34500	$23.1\ ^{+1.9}_{-1.7}$	Oe8.5 V
75980	14.12	14.17	-11.03	-1.02	0.81	30000	$23.9\ ^{+1.9}_{-2.6}$	Be0 V
76371	13.76	13.96	-11.04	-0.91	0.30	31500	$23.0\ ^{+1.7}_{-1.6}$	O9.5 III
77368	13.76	14.00	-13.02	-0.93	0.15	41000	$41.5\ ^{+2.7}_{-3.3}$	O6.5V
77458	13.00	13.15	-11.92	-0.92	0.45	29250	$34.3\ ^{+2.9}_{-4.1}$	Be0.2 III
77609	12.55	12.69	-11.60	-0.91	0.48	25000	$34.8\ ^{+13.2}_{-4.5}$	B0.5 I
78694	14.27	14.35	-11.49	-0.98	0.72	36250	$25.1\ ^{+2.5}_{-1.7}$	Oe8 V
79248	14.40	14.60	-12.50	-0.92	0.29	34500	$37.8\ ^{+3.0}_{-2.5}$	O8.5 V
80998	14.24	14.46	-11.98	-0.96	0.25	37750	$29.7\ ^{+2.5}_{-2.1}$	O7.5 V
81019	14.24	14.43	-10.95	-0.93	0.33	31500	$22.5\ ^{+1.6}_{-1.5}$	O9.5 V

Table 3.1 – *Continued from previous page*

ID	B	V	Q	M_{bol}	A_V	T_{eff} (K)	Mass ($M_\odot$)	Sp Type
81646	14.15	14.36	-11.52	-0.92	0.26	34500	$25.1\ ^{+3.2}_{-1.0}$	O8.5 V
81941	13.82	14.03	-11.45	-0.89	0.24	31500	$26.7\ ^{+1.7}_{-2.2}$	O9.5 V
82322	14.12	14.37	-10.81	-0.88	0.09	30000	$21.7\ ^{+1.7}_{-2.3}$	B0 V
82489	14.17	14.22	-12.09	-1.04	0.86	39250	$30.9\ ^{+2.4}_{-2.5}$	Oe7 V
83171	14.28	14.39	-10.91	-0.94	0.58	30000	$22.0\ ^{+2.0}_{-1.3}$	Be0 V
83678	12.99	13.18	-12.79	-0.95	0.36	34500	$43.4\ ^{+3.9}_{-3.7}$	O8.5 III

CHAPTER 4

Conclusions

The high mass tail of the stellar IMF is an important diagnostic tool for star formation. This is especially true for sparse star formation, where it is difficult to differentiate between stochastic sampling of a universal IMF and a deterministic $m_{\rm max}$-$M_{\rm cl}$ relationship. In this thesis, we presented high-resolution HST imaging of field massive stars in the SMC and optical spectra from our RIOTS4 survey of a spatially complete sample of field OB stars in the SMC. These observations provided critical constraints on theories of massive star formation, the $m_{\rm max}$-$M_{\rm cl}$ relationship, and the integrated galactic initial mass function (IGIMF).

4.1 Summary of Chapter 2

In Chapter 2, we present *HST* ACS observations of eight field OB stars in the SMC. We find no evidence of clustering around five of the eight targets, down to our detection limit of $1.5M_{\odot}$. However, radial velocities reveal two of these five stars to be runaways. The remaining three objects remain candidates for isolated massive star formation. Two of these three stars are associated with HII regions, which strengthens their case as examples of isolated massive star formation. The remaining three stars exist within sparse clusters, which we detect using two separate methods, a stellar density analysis and a friends of friends algorithm. In each case, these clusters contain 8-10 stars from $1-4M_{\odot}$ along with the putative field OB star.

Assuming each of the non-runaway stars is clustered, we extrapolate our observations below their detection limit to derive the properties of these sparse clusters. By integrating the observed population over a standard Kroupa IMF (Kroupa 2001)

from $0.8-150M_{\odot}$, we estimate $M_{\rm cl} = 43-103M_{\odot}$ and $N_* = 19-171$. Assuming the random sampling from the standard Kroupa IMF, we calculate a $0.01-0.2$ probability that these clusters would contain a star as massive as those observed. We further examine the inferred cluster properties by comparing them to clusters generated from simplistic Monte Carlo simulations. These simulated clusters are generated according to a stellar clustering law or cluster mass function and subsequently populated with a standard Kroupa IMF. We adopt a –2 power law slope for the clustering law and cluster mass function with $N_{*,\rm lo} = 40$ and $M_{\rm cl,lo} = 20M_{\odot}$, respectively. Compared with these simulated clusters, our observations all fall below the 50th percentile of either $M_{\rm cl}$ or N_* as a function of $m_{\rm max}$. In contrast, the Galactic cluster sample of Weidner et al. (2010) exists almost entirely above the 90th percentile. These numbers suggest that among clusters with at least one O star, our observations are closer to a typical cluster than those with a well-populated IMF.

We demonstrate that our observations are inconsistent with a deterministic $m_{\rm max}$-$M_{\rm cl}$ relationship, as defined by the Galactic cluster sample and semi-analytical calculations of Weidner et al. (2010) or the competitive accretion models of Bonnell et al. (2004). Thus, our observations are more consistent with monolithic collapse star formation models, rather than competitive accretion models. Similarly, our observations are inconsistent with the IGIMF effect as proposed by Weidner & Kroupa 2005. Rather, our observations are consistent with clusters being randomly populated from a universal IMF, with a uniform upper mass limit.

4.2 Summary of Chapter 3

In Chapter 3, we present a complete census of field massive stars in the SMC using spectroscopic observations from our RIOTS4 survey. RIOTS4 spectra come primarily from the IMACS multi-object spectrograph with R $\sim 2600-3700$. The remaining spectra come from the MIKE echelle spectrograph R $\sim$ 28000 or IMACS long slit spectra R $\sim 1000-1300$. These observations cover all of the 374 stars in the field OB star sample from Oey et al. (2004). Using spectral types from RIOTS4 and photometry from Massey (2002), we derive the physical quantities of effective tem-

perature, $T_{\rm eff}$, and bolometric magnitude, $M_{\rm Bol}$, for the majority of these objects. These are used to derive accurate mass estimates for individual stars with typical errors of $\sim 2M_{\odot}$.

We derive the field IMF using the 178 stars above the RIOTS4 completeness limit of $20M_{\odot}$. Using three fitting techniques, we determine that the slope of the present day mass function (PDMF) for the SMC field is $\Gamma_{\rm PDMF} = 2.8$ to 3.5. We derive the field IMF from the observed PDMF by comparing our observations with artificial field populations generated from a Monte Carlo code. We vary the input IMF of the artificial populations between $\Gamma_{\rm IMF}$=1.0 to 4.0 and measure the distribution of PDMF slopes for 10^4 iterations of each code. By comparing the PDMF distribution with our observations, we infer that the IMF of the field is $\Gamma_{\rm IMF}$=2.3$\pm$0.4.

To extend this IMF measurement to lower masses, we use BV photometry from the Optical Gravitational Lensing Experiment (OGLE). We identify the field population using a friends of friends algorithm and develop a novel technique to measure the IMF for these stars. For each star, we generate 10^4 realizations of its BV photometry by randomly sampling the individual B, V and extinction errors along a Gaussian distribution centered on the observed value, with 1-σ given by the observed error in each quantity. From these realizations, we construct a probability distribution for the mass of each star, which is then split fractionally into different mass bins. With the OGLE data, we derive a field IMF of $\Gamma_{\rm IMF}$=2.3$\pm$0.6 from $7 - 20M_{\odot}$. When combined with a binned mass distribution of the RIOTS4 data, the field IMF $> 7M_{\odot}$ is given by $\Gamma_{\rm IMF}$=2.4$\pm$0.4. Our steep IMF measurements are lower than previous measurements for the SMC field of $\Gamma_{\rm IMF} \sim 4$(Massey et al. 1995; Massey 2002). In all our measurements, the SMC field IMF is significantly steeper than a Salpeter slope of $\Gamma_{\rm IMF}$= 1.35. However, the lowest mass bins of the OGLE IMF may hint at a turnover happening towards a slope more consistent with Salpeter.

We investigate the possibility that the steep observed PDMF could be reconciled with a Salpeter IMF using different models for the SMC star formation history. We find that our observed PDMF slope $> 20M_{\odot}$ agrees with a model where all star formation occurs within a burst beginning 8 Myr ago and lasting for 4.5 Myrs. However,

below $20M_{\odot}$, the IMF of this model exhibits a dramatic flattening not observed in the OGLE IMF. Thus, even with a variable star formation history, we are unable to explain the observed PDMF of the field with a Salpeter IMF. The consequences of a steep field IMF depend largely on the origin of the field population. If the field is composed mainly of stars formed in sparse clusters, then a steep IMF could indicate the existence of a deterministic $m_{\rm max}$-$M_{\rm cl}$ relationship. This, in turn, supports the concept of a steep IGIMF (Weidner & Kroupa 2005). Alternatively, if the field is formed mainly in situ, this steep IMF may indicate that field stars form with a different IMF than clustered stars. Finally, runaway stars add a complicating factor to the steep IMF, since they are most common at higher masses. Thus, a significant contribution from runaways may imply that the IMF of sparse and in situ field star formation is even steeper than our observations would indicate.

4.3 Interpretation

Using HST imaging, we establish the existence of sparse clusters with massive O stars and candidates for in situ field O star formation. With our RIOTS4 survey, we find the SMC field has a steep IMF that is inconsistent with the canonical Salpeter IMF. Placed in the context of star formation, these results appear somewhat contradictory. When viewed as individual clusters, these objects are inconsistent with a deterministic $m_{\rm max}$-$M_{\rm cl}$ relation and instead, support the random sampling of clusters from a universal Kroupa IMF. However, when viewed as a complete stellar population, the steep IMF of the field indicates that sparse star formation does not fully sample the top of the IMF and is consistent with a deterministic $m_{\rm max}$-$M_{\rm cl}$ relation. Even so, there are a few scenarios that might explain this apparent contradiction.

One possibility is that the sparse O star clusters we observed were merely the remnants of richer clusters that have mostly dispersed. In this scenario, the original cluster may have formed in a manner fully consistent with a deterministic $m_{\rm max}$-$M_{\rm cl}$ relation. This scenario implies that field massive stars likely all formed in clusters that either quickly dispersed or ejected the stars as runaways.

A second potential explanation is a difference in the formation mechanism between

clustered and isolated stars. In this scenario, the sparse O star clusters may sample the canonical Salpeter IMF up to $\sim 150 M_{\odot}$, while sparse, in situ field formation is limited to a lower value of $m_{\rm up}$ and/or a steeper IMF slope. In this scenario, a key issue is defining the characteristics of field and clustered formation. Are they distinguished by the properties of their natal gas cloud, or the number of stars formed? Our Monte Carlo simulations from Chapter 2 may provide an answer. We found that limiting the stellar clustering law to $N_* \geq 40$ provided the best match to the observed fraction of isolated O stars in the Galaxy and Magellanic Clouds. In particular, we discovered that extending the clustering law to lower N_* values would result in a significant overproduction of field O stars. Therefore, if this model is accurate, a change from clustered to sparse star formation may occur around $N_* = 40$. However, if this clear dichotomy of cluster and field star formation exists, why hasn't it been observed for local, low mass field stars? An answer to this question is hinted at in the Chapter 3 results of the field IMF using photometry from OGLE for $7 - 20 M_{\odot}$ stars. While this observed field IMF slope is steeper than Salpeter, the lowest mass bins exhibit a gradual turnover towards a Salpeter slope. Thus, it is possible that the steep field IMF exists only above $10 M_{\odot}$.

Finally, the runaway population may add a false $m_{\rm up}$ constraint, depending on the method and timescale of runaway ejections. If most runaways happen via the binary supernova scenario, then the runaway population would be composed of the secondary, lower mass stars from these binary systems, which would effectively limit the runaway population to masses $< m_{\rm up}$. Alternatively, if the timescale for ejection is longer than the lifetime of the highest mass stars, then the runaway population would also fail to extend to $m_{\rm up}$. However, runaways cannot fully explain our observations, since the runaway fraction of O stars is higher than B stars. Thus, the flat IMF of runaways is inconsistent with our observations of a steep field IMF.

While we cannot definitively distinguish between these scenarios, some of our results are still solid. The steep field IMF of the SMC is a robust result, found separately using two different datasets, RIOTS4 spectra and OGLE photometry. The large number of stars in our RIOTS4 survey and the spatially complete sample both

work to overcome the effects of stochasticity. This confirms the earlier steep IMF measurements of the SMC field by Massey et al. (1995) and Massey (2002). Furthermore, the steep observed field IMF is direct evidence that the slope of the high mass tail of the IGIMF must be steeper than Salpeter. However, it is unclear if this results from a deterministic $m_{\rm max}$-$M_{\rm cl}$ relation, or the formation of stars in clusters with $M_{\rm cl} < m_{\rm up}$. Future observations of a large sample of sparse O star clusters may be able to conclusively determine whether such an $m_{\rm max}$-$M_{\rm cl}$ relation exists.

BIBLIOGRAPHY

Adams, F. C., & Myers, P. C. 2001, ApJ, 553, 744

Allison, R. J., Goodwin, S. P., Parker, R. J., et al. 2009, ApJ, 700, L99

Azzopardi, M., Vigneau, J., & Macquet, M. 1975, A&AS, 22, 285

Banerjee, S., Kroupa, P., & Oh, S. 2012, ApJ, 746, 15

Bastian, N., Covey, K. R., & Meyer, M. R. 2010, ARA&A, 48, 339

Bastian, N., & Goodwin, S. P. 2006, MNRAS, 369, L9

Battinelli, P. 1991, A&A, 244, 69

Bertoldi, F., & McKee, C. F. 1992, ApJ, 395, 140

Blaauw, A. 1961, Bull. Astron. Inst. Netherlands, 15, 265

Bonanos, A. Z., Lennon, D. J., Köhlinger, F., et al. 2010, AJ, 140, 416

Bonnell, I. A., Bate, M. R., Clarke, C. J., & Pringle, J. E. 2001, MNRAS, 323, 785

Bonnell, I. A., Bate, M. R., & Vine, S. G. 2003, MNRAS, 343, 413

Bonnell, I. A., & Clarke, C. J. 1999, MNRAS, 309, 461

Bonnell, I. A., Clark, P., & Bate, M. R. 2008, MNRAS, 389, 1556

Bonnell, I. A., Larson, R. B., & Zinnecker, H. 2007, Protostars and Planets V, 149

Bonnell, I. A., Vine, S. G., & Bate, M. R. 2004, MNRAS, 349, 735

Chandar, R., Fall, S. M., & Whitmore, B. C. 2010, ApJ, 711, 1263

Charbonnel, C., Meynet, G., Maeder, A., Schaller, G., & Schaerer, D. 1993, A&AS, 101, 415

Crowther, P. A. 1997, IAU Symposium, 189, 137

Crowther, P. A., Schnurr, O., Hirschi, R., et al. 2010, MNRAS, 408, 731

de Grijs, R., & Goodwin, S. P. 2008, MNRAS, 383, 1000

de Wit, W. J., Testi, L., Palla, F., Vanzi, L., & Zinnecker, H. 2004, A&A, 425, 937

de Wit, W. J., Testi, L., Palla, F., & Zinnecker, H. 2005, A&A, 437, 247

Eddington, A. S. 1924, MNRAS, 84, 308

Elmegreen, B. G. 2000, ApJ, 530, 277

Elmegreen, B. G. 2006, ApJ, 648, 572

Elmegreen, B. G. 2008, ApJ, 672, 1006

Evans, C. J., & Howarth, I. D. 2008, MNRAS, 386, 826

Evans, C. J., Howarth, I. D., Irwin, M. J., Burnley, A. W., & Harries, T. J. 2004, MNRAS, 353, 601

Evans, C. J., Lennon, D. J., Smartt, S. J., & Trundle, C. 2006, A&A, 456, 623

Fall, S. M., Chandar, R., & Whitmore, B. C. 2009, ApJ, 704, 453

Gies, D. R. 1987, ApJS, 64, 545

Girardi, L., Bertelli, G., Bressan, A., et al. 2002, A&A, 391, 195

Gvaramadze, V. V., Weidner, C., Kroupa, P., & Pflamm-Altenburg, J. 2012, MNRAS, 3336

Haas, M. R., & Anders, P. 2010, A&A, 512, A79

Harries, T. J., Hilditch, R. W., & Howarth, I. D. 2003, MNRAS, 339, 157

Harris, W. E., & Pudritz, R. E. 1994, ApJ, 429, 177

Hoogerwerf, R., de Bruijne, J. H. J., & de Zeeuw, P. T. 2001, A&A, 365, 49

Hoversten, E. A., & Glazebrook, K. 2008, ApJ, 675, 163

Hoyle, F. 1953, ApJ, 118, 513

Hunter, I., Dufton, P. L., Smartt, S. J., et al. 2007, A&A, 466, 277

Hunter, D. A., Elmegreen, B. G., Dupuy, T. J., & Mortonson, M. 2003, AJ, 126, 1836

Jeans, J. H. 1902, Royal Society of London Philosophical Transactions Series A, 199, 1

Kiminki, D. C., & Kobulnicky, H. A. 2012, ApJ, 751, 4

Koen, C. 2006, MNRAS, 365, 590

Köppen, J., Weidner, C., & Kroupa, P. 2007, MNRAS, 375, 673

Kroupa, P. 2001, MNRAS, 322, 231

Kroupa, P., & Weidner, C. 2003, ApJ, 598, 1076

Krumholz, M. R., Cunningham, A. J., Klein, R. I., & McKee, C. F. 2010, ApJ, 713, 1120

Krumholz, M. R., Klein, R. I., McKee, C. F., Offner, S. S. R., & Cunningham, A. J. 2009, Science, 323, 754

Krumholz, M. R., & McKee, C. F. 2008, Nature, 451, 1082

Jeans, J. H. 1902, Royal Society of London Philosophical Transactions Series A, 199, 1

Lada, C. J., & Lada, E. A. 2003, ARA&A, 41, 57

Lamb, J. B., Oey, M. S., Werk, J. K., & Ingleby, L. D. 2010, ApJ, 725, 1886

Lee, J. C., Gil de Paz, A., Tremonti, C., et al. 2009, ApJ, 706, 599

Lennon, D. J. 1997, A&A, 317, 871

Li, Y., Klessen, R. S., & Mac Low, M.-M. 2003, ApJ, 592, 975

Maeder, A., & Meynet, G. 2001, A&A, 373, 555

Maíz-Apellániz, J., Walborn, N. R., Galué, H. Á., & Wei, L. H. 2004, ApJS, 151, 103

Maschberger, T., & Clarke, C. J. 2008, MNRAS, 391, 711

Maschberger, T., Clarke, C. J., Bonnell, I. A., & Kroupa, P. 2010, MNRAS, 404, 1061

Massey, P. 2002, ApJS, 141, 81

Massey, P. 2011, UP2010: Have Observations Revealed a Variable Upper End of the Initial Mass Function?, 440, 29

Massey, P., Lang, C. C., Degioia-Eastwood, K., & Garmany, C. D. 1995, ApJ, 438, 188

Massey, P., Puls, J., Pauldrach, A. W. A., et al. 2005, ApJ, 627, 477

Massey, P., Zangari, A. M., Morrell, N. I., et al. 2009, ApJ, 692, 618

Meurer, G. R., Heckman, T. M., Leitherer, C., et al. 1995, AJ, 110, 2665

Meurer, G. R., Wong, O. I., Kim, J. H., et al. 2009, ApJ, 695, 765

Negueruela, I., Steele, I. A., & Bernabeu, G. 2004, Astronomische Nachrichten, 325, 749

Oey, M. S. 2011, ApJ, 739, L46

Oey, M. S., & Clarke, C. J. 1998, AJ, 115, 1543

Oey, M. S., & Clarke, C. J. 2005, ApJ, 620, L43

Oey, M. S., King, N. L., & Parker, J. W. 2004, AJ, 127, 1632

Oey, M. S., Parker, J. S., Mikles, V. J., & Zhang, X. 2003, AJ, 126, 2317

Parker, R. J., & Goodwin, S. P. 2007, MNRAS, 380, 1271

Pflamm-Altenburg, J., & Kroupa, P. 2010, MNRAS, 404, 1564

Pflamm-Altenburg, J., Weidner, C., & Kroupa, P. 2009, MNRAS, 395, 394

Porter, J. M., & Rivinius, T. 2003, PASP, 115, 1153

Poveda, A., Ruiz, J., & Allen, C. 1967, Boletin de los Observatorios Tonantzintla y Tacubaya, 4, 86

Robin, A. C., Reylé, C., Derrière, S., & Picaud, S. 2003, A&A, 409, 523

Rosolowsky, E. 2005, PASP, 117, 1403

Salpeter, E. E. 1955, ApJ, 121, 161

Sana, H., Gosset, E., & Evans, C. J. 2009, MNRAS, 400, 1479

Sana, H., Gosset, E., Nazé, Y., Rauw, G., & Linder, N. 2008, MNRAS, 386, 447

Sana, H., James, G., & Gosset, E. 2011, MNRAS, 416, 817

Scalo, J. M. 1986, Fundamentals of Cosmic Physics, 11, 1

Searle, L., & Zinn, R. 1978, ApJ, 225, 357

Selman, F. J., Espinoza, P., & Melnick, J. 2011, UP2010: Have Observations Revealed a Variable Upper End of the Initial Mass Function?, 440, 39

Selman, F. J., & Melnick, J. 2008, ApJ, 689, 816

Shu, F. H., Adams, F. C., & Lizano, S. 1987, ARA&A, 25, 23

Sirianni, M., Jee, M. J., Benítez, N., et al. 2005, PASP, 117, 1049

Smith, C., Leiton, R., & Pizarro, S. 2000, Stars, Gas and Dust in Galaxies: Exploring the Links, 221, 83

Spaans, M., & Silk, J. 2000, ApJ, 538, 115

Stanimirović, S., Staveley-Smith, L., & Jones, P. A. 2004, ApJ, 604, 176

Staveley-Smith, L., Sault, R. J., Hatzidimitriou, D., Kesteven, M. J., & McConnell, D. 1997, MNRAS, 289, 225

Stone, R. C. 1991, AJ, 102, 333

Testi, L., Palla, F., Prusti, T., Natta, A., & Maltagliati, S. 1997, A&A, 320, 159

Testi, L., Palla, F., & Natta, A. 1999, A&A, 342, 515

Thilker, D. A., Bianchi, L., Meurer, G., et al. 2007, ApJS, 173, 538

Úbeda, L., Maíz-Apellániz, J., & MacKenty, J. W. 2007, AJ, 133, 932

Udalski, A., Szymanski, M., Kubiak, M., et al. 1998, Acta Astronomica, 48, 147

van den Bergh, S. 2004, AJ, 128, 1880

Walborn, N. R., 2009, in Stellar Spectral Classification by Richard O. Gray and Christopher J. Corbally. (eds) Princeton University Press, 2009.

Walborn, N. R., & Fitzpatrick, E. L. 1990, PASP, 102, 379

Walborn, N. R., Lennon, D. J., Haser, S. M., Kudritzki, R.-P., & Voels, S. A. 1995, PASP, 107, 104

Walborn, N. R., Lennon, D. J., Heap, S. R., et al. 2000, PASP, 112, 1243

Weidner, C., Bonnell, I. A., & Moeckel, N. 2011, MNRAS, 410, 1861

Weidner, C., & Kroupa, P. 2004, MNRAS, 348, 187

Weidner, C., & Kroupa, P. 2005, ApJ, 625, 754

Weidner, C., & Kroupa, P. 2006, MNRAS, 365, 1333

Weidner, C., Kroupa, P., & Bonnell, I. A. D. 2010, MNRAS, 401, 275

White, S. D. M., & Rees, M. J. 1978, MNRAS, 183, 341

Zaritsky, D., Harris, J., Thompson, I. B., Grebel, E. K., & Massey, P. 2002, AJ, 123, 855

Zhang, Q., & Fall, S. M. 1999, ApJ, 527, L81

Zinnecker, H. 1982, Annals of the New York Academy of Sciences, 395, 226